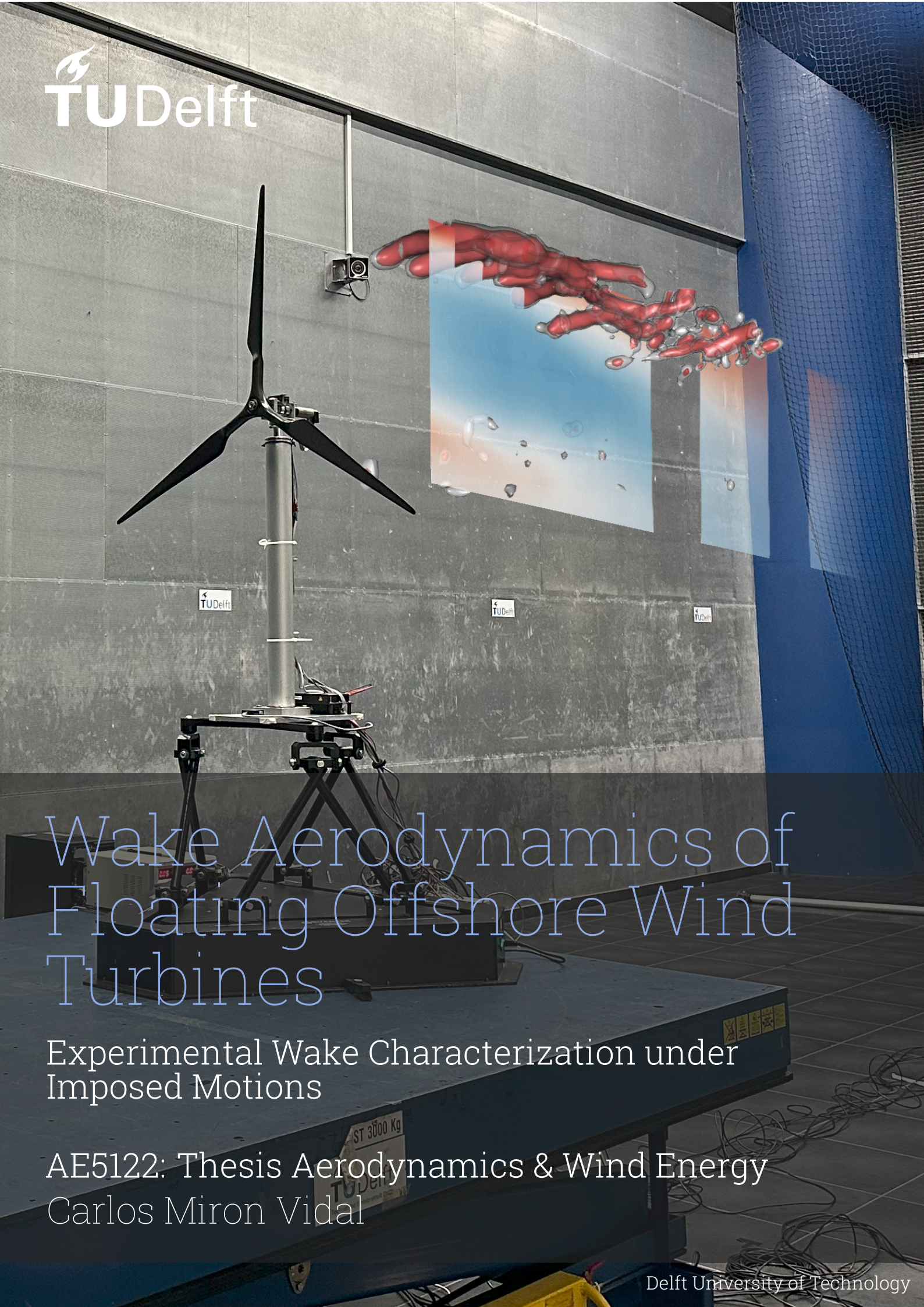

Wake Aerodynamics of Floating Offshore Wind Turbines

Experimental Wake Characterization under Imposed Motions

AE5122: Thesis Aerodynamics & Wind Energy

Carlos Miron Vidal

Delft University of Technology

Wake Aerodynamics of Floating Offshore Wind Turbines

Experimental Wake Characterization under Imposed Motions

by

Carlos Miron Vidal

Supervisor:	F. Taruffi
Defense Chair:	D. Ragni
External Member:	A. Sciacchitano
Project Duration:	Nov, 2024 - July, 2025
Faculty:	Faculty of Aerospace Engineering, Delft

TU Delft

Preface

The work you're about to read marks the final step of my Master of Science in Aerospace Engineering at Delft University of Technology. I'm proud to present it here and truly hope you enjoy the read.

This work is dedicated to my family and friends in Spain, who have continuously supported my choices and stood by me, even from a distance. To my close friends here in Delft and Den Haag, thank you for being part of this journey: for the fun weekends, concerts, and F1 watch sessions that pulled me away from studying when I needed it, and also for studying and tackling tough assignments together.

A special thanks goes to my thesis supervisor, F. Taruffi, for the smooth collaboration and constant guidance during the experimental phase. I'm also grateful to everyone in the Aerodynamics and Wind Energy departments who offered advice or lent a hand, and to my office colleagues for making the process more enjoyable. Your help played a key role in the success of the experimental campaign, data post-processing, and analysis.

Carlos Miron Vidal
Delft, July 2025

Summary

As global energy systems transition toward carbon neutrality, offshore wind energy continues to gain momentum due to stronger and more stable wind profiles. However, deeper waters, where most offshore wind potential lies, require Floating Offshore Wind Turbines (FOWTs). Unlike fixed turbines, FOWTs are mounted on floating platforms and subjected to six degrees of freedom (6DOF) motion caused by wind and waves. These motions significantly influence the wake, the turbulent region downstream of the turbine, which in turn impacts performance, energy capture, and optimal spacing within wind farms.

This thesis addresses a critical gap in experimental wake research by investigating the impact of floating platform motions on wind turbine wake dynamics and recovery, an area where high-quality data is scarce due to the significant technical challenges of experimental setups. These challenges include the use of rotating machinery, large-scale physical models, complex scaling constraints, and a reliable platform able to perform 6DOF motions. All these affect the ability to perform accurate and repeatable measurements.

To overcome the challenges and reduce uncertainties, a 1:148 scale version of the DTU 10MW reference wind turbine was mounted on top of the commercially available Quanser 6DOF Hexapod. 3D Particle Tracking Velocimetry (PTV) measurements were used to reconstruct the flow field through DaVis software and hardware for a range between 0.6D and 5D (diameters) downstream. Four FASTCAM MINI AX100 compatible cameras recording at 400Hz were used in the setup and captured the Helium-filled soap bubbles (HFSB) used as tracers. Shake-The-Box (STB) algorithm and Vortex-In-Cell Plus (VIC+) method were later selected to reconstruct and post-process the raw image sets. The experiment was carried out in the Open Jet Facility (OJF) at Delft University of Technology, a low speed wind tunnel with high-quality baseline flow.

The investigation characterizes the wake under varying conditions, and explores the wake recovery capabilities of FOWTs compared to stationary wind turbines. Surge and pitch are the most common motions in FOWTs; therefore, two different sinusoidal motions for each were implemented to simulate typical floating behavior. In addition to the main study, realistic wave patterns were tested to complement the analysis and compare performance against the imposed sinusoidal motions.

To analyze it, unconditionally averaged velocity components and turbulence intensity fields are presented, together with vorticity around the y-axis and the Reynolds Stress component for x and z. Velocity deficit line plots are provided to clearly quantify wake recovery of all cases and compare them in a clear way. Furthermore, a frequency study using power spectral density (PSD) and proper orthogonal decomposition (POD) determine which frequencies are more intense and where do they affect the flow. Additionally, both a phase-lock analysis and a deep dive into vortex structures are presented.

Key findings include that 2Hz surge motion lead to the most favorable wake recovery ($\approx 40\%$ better than the static case at a distance of 5D), while 5Hz pitch performs the worst. Low-frequency motions enhance near-wake turbulence and accelerate the wake transition to a fully mixed state, whereas high-frequency motions only show localized effects. Vorticity and Reynolds stress analyses confirm increased mixing and earlier vortex diffusion with the motion cases. Furthermore, spectral analysis reveals a strong energy concentration at 2Hz motions, while 5Hz motions show minimal contribution to flow energy. The leapfrogging location for this turbine is found to be around 1.5D downstream of the rotor, and the near wake is estimated to last until 4D.

Contents

List of Figures

List of Tables

Nomenclature

Abbreviations

Abbreviation	Definition
1P	Turbine's rotation frequency
2D PIV	Planar Particle Image Velocimetry
3P	Blade passing frequency
BEM	Blade Element Momentum theory
CFD	Computational Fluid Dynamics
CO_2	Carbon Dioxide
CTA	Constant Temperature Anemometer
DC	Direct Current
DOF	Degrees of Freedom
DTU	Danmarks Tekniske Universitet
FOWT	Floating Offshore Wind Turbine
FOV	Field of View
fps	Frames per second
GW	Giga Watt
HAWT	Horizontal Axis Wind Turbine
HFSB	Helium Filled Soap Bubbles
HF	High Frequency
HIL	Hardware-in-the-Loop
HWA	Hot Wire Anemometry
IPR	Iterative Particle Reconstruction
kHz	Kilohertz
kW	Kilowatt
LCOE	Levelized Cost of Energy
LED	Light Emitting Diode
LES	Large Eddy Simulations
LF	Low Frequency
LPT	Lagrangian Particle Tracking
MART	Multiplicative Algebraic Reconstruction Techniques
MW	Megawatt
NLR	Netherlands Aerospace Centre
OJF	Open Jet Facility
PIV	Particle Image Velocimetry
POD	Proper Orthogonal Decomposition
ppv	Particles Per Voxel
PSD	Power Spectral Density
PTU	Programmable Timing Unit
RWT	Reference Wind Turbine
SPIV	Stereo Particle Image Velocimetry
STD	Standard Deviation
STB	Shake The Box
TI	Turbulence Intensity
TKE	Turbulent Kinetic Energy
TLP	Tension Leg Platform
TSR	Tip Speed Ratio
TWh	Terawatt Hour

Abbreviation	Definition
URANS	Unsteady Reynolds-Averaged Navier-Stokes
VIC	Vortex-In-Cell
VIC+	Vortex-In-Cell Plus
VSC	Volume Self-Calibration

Symbols

Symbol	Definition	Unit
C	Particle concentration	ppv
C_D	Drag coefficient	-
C_L	Lift coefficient	-
D	Rotor diameter	m
d_i	Distance from sensor to lens	m
d_o	Distance from plane of interest to lens	m
E	Output voltage	V
f	Focal length	mm
$f_\#$	f-stop	-
f_r	Reduced frequency	-
Δt	Interval between frames	s
ΔV^*	Normalized velocity variation	-
Δx	Displacement	m
h	Sensor size	mm
H	Object size	m
I	Current	A
M	Magnification factor	-
$\mathcal{F}$	Fourier Transform	-
Ω	Rotor rotational speed	rad/s
R	Resistance	Ω
$\overline{u'w'}$	xz-component of Reynolds stresses	m^2/s^2
rpm	Revolutions per minute	rpm
T	Thrust	N
u	Velocity component in x direction	m/s
v	Velocity component in y direction	m/s
w	Velocity component in z direction	m/s
γ	Yaw angle	deg
θ	Pitch angle	deg
λ	Swirling Strength / Wavelength	$1/s^2$ or m
δ_z	Depth of field	m
U_∞	Freestream velocity	m/s
μm	Micrometer	10^{-6} m

1 Introduction

The impacts of human activity on the environment have become increasingly evident, with climate change manifesting in more frequent and severe weather phenomena. Europe has witnessed a notable rise in extreme heatwaves and droughts in recent years, while the frequency and intensity of heavy rainfall and resulting floods are also on the rise. At the same time, the rapid retreat of glaciers is disrupting water resources, damaging ecosystems. These developments are closely tied to the steady rise in global surface temperatures since industrial times [1].

Scientific consensus has established a direct link between the rise in surface temperatures and the emission of greenhouse gases, particularly carbon dioxide (CO_2), primarily from burning fossil fuels. As the global population grows, emissions are projected to increase further unless significant action is taken to reduce them [2].

In response, the 2015 Paris Agreement marked a global commitment by 196 countries to limit the increase in average global temperature to well below 2°C, and preferably to 1.5°C above pre-industrial levels [3]. However, even the most optimistic emission transition, which aim for net zero CO_2 emissions by 2050, suggest a temporary exceedance of the 1.5°C threshold by 2030 [4].

A key element of this transition is the adoption of renewable energy, mainly solar and wind power. Wind energy, in particular, holds vast untapped potential to meet global electricity demands multiple times over [5]. To align with net zero goals, wind power generation must reach approximately 8,000 TWh by 2030, requiring an exponential increase in less than a decade [6]. Research in wind energy is highly relevant, as even small advancements can significantly improve operational performance and potentially save millions of euros. Investing in both numerical and experimental wind energy studies should be a top priority for countries and governments, as it may be one of the few viable paths to achieving net-zero emissions targets.

1.1. Goal of the Thesis

Despite the rapid development and growing relevance of wind energy, especially floating offshore wind turbines (FOWTs), experimental investigations remain relatively low. The field presents significant technical challenges: experimental setups often involve rotating machinery, large-scale physical models, or complex scaling requirements. These factors make it difficult to conduct accurate, repeatable experiments, limiting the amount of high quality data available.

In particular, multiple FOWT configurations, where wake recovery plays an important role, are still underexplored. Most existing studies rely heavily on numerical simulations, which often require simplifications and assumptions to remain computationally feasible. While simulation tools are valuable, they cannot fully capture the real world behavior, especially when it comes to complex interactions like wake dynamics or recovery. Reiterating again, experimental studies are not only important but also form the foundation for current and future research directions.

This thesis aims to address this gap by contributing experimental insights into floating offshore wind energy systems. Specifically, the focus is on characterizing the wake generated behind a FOWT. Understanding wake behavior is essential, as it directly influences the spacing, layout, and efficiency of future wind farms. By providing a clearer picture of these wake effects in a floating offshore context, this research seeks to support the design of more effective and economically viable wind energy systems.

Previous Experimental Campaign

An experimental campaign with a similar objective and setup focused on characterizing the near-wake region of a FOWT was performed in 2024 [7]. This study aimed to understand how the motions of the upstream, floating turbine influenced the flow field and, additionally, investigated the performance of a tandem configuration, where two turbines were placed in series.

The study examined how different motions affected the wake and how these translated into performance variations for the second turbine. It demonstrated that floating motion is a critical factor in wake behavior, highlighting the need to consider these effects when designing and optimizing floating wind farms.

However, despite these contributions, the study also presented limitations. The wake analysis was confined to a relatively small downstream region, which lacked analysis of wake development and recovery. Furthermore, a comparative case involving a fixed, non-floating horizontal-axis wind turbine (HAWT) was absent. Without such a baseline, it remains challenging to assess how much of the wake behavior can be attributed to the FOWT dynamics versus inherent aerodynamic characteristics.

This thesis builds on that foundation by addressing some of these gaps. Through this, the aim is to deepen the understanding of how floating motions affect aerodynamic performance and inter-turbine interactions in multi-turbine offshore wind farm configurations.

The study presented in this thesis will expand on the volumes and test cases covered by the previous campaign. A primary focus will be understanding wake recovery and development under different motions and conditions. These research interests are represented in the research questions.

Research Questions

Research Question I:
How do floating motions affect the wake characteristics of a FOWT?

This question is selected as the study aims to shed light on the wake behavior of a wind turbine subjected to platform motions. Key aspects such as the main energetic components, vortical structures, and the overall velocity field are expected to be understood by the end of this work.

Ia. How do low- and high-frequency motions differently influence the wake behavior of a floating offshore wind turbine?

This sub-question recognizes the distinction between low and high frequency for both surge and pitch sinusoidal motions. The frequency is directly linked to the amplitude of the motion, and it could be used to represent different sea state intensities.

Ib. How does the wake differ when the FOWT exhibits pitching versus surging sinusoidal motions?

Similarly, this sub-question ensures that the pitch and surge specific effects are studied independently and then compared to each other.

Research Question II:
How does wake recovery change with FOWT motions compared to a stationary wind turbine?

Answering this question can have huge implications in FOWT wind farm performance, layout geometry, and economics. By comparing the results with a HAWT farm, fast and clear conclusions on which is more efficient and profitable can be drawn.

IIa. Which motion modes and amplitudes result in the most significant changes in wake recovery?

It is expected that certain motions operating at certain frequencies will influence the wake development in different ways. Knowing the answer to this question can help wind farm designers plan for amplificating or diminishing specific motion amplitudes.

IIb. Does imposing a realistic wave-induced motion pattern lead to enhanced wake mixing compared to simplified sinusoidal motions?

With this sub-question the study aims to find if ”random” combinations of motions and frequencies have some benefits in wake development when compared with the presented sinusoidal pitch and surge motions. Additionally, whether any of the sinusoidal motions is comparable to realistic wave-induced motion patterns

1.2. Report Outline

The core of this thesis consists of three chapters:

Chapter 2: Background and Literature Study
This chapter provides a brief overview of the evolution of wind energy with a focus on FOWTs. It introduces the typical loads experienced by wind turbines and offers a detailed description of their wake characteristics. Previous studies on HAWTs, FOWTs, and floating offshore wind farm configurations are reviewed. Furthermore, the chapter outlines the most commonly used experimental techniques and flow measurement methods in wind energy research.

Chapter 3: Methodology
This chapter presents the experimental facilities, equipment, and setup used in the study, along with a discussion of their limitations. In addition, the data acquisition methods and post-processing procedures are described in detail. With the information presented in this chapter, the experimental study can be replicated by other researchers aiming to study the wake characteristics of a wind turbine.

Chapter 4: Results
This chapter presents the processed experimental data and delivers a comprehensive analysis aimed at addressing the research questions. It begins with a convergence analysis applied to all datasets to ensure result consistency. The velocity field, turbulence intensity, and phase-locked contour visualizations are then examined in detail. Emphasis is placed on comparing the effects of various motion types, frequencies, and amplitudes, including those induced by wave-like motion. To facilitate these comparisons, velocity deficit line plots are used to quantify wake recovery.

Tip vortex behavior is also briefly analyzed across different cases. Furthermore, energy spectra are evaluated to identify the most dynamically significant scenarios. The chapter concludes with a quantification of experimental uncertainties to assess the reliability and accuracy of the results.

A conclusion is present at the end of the thesis to answer the research questions and summarize the most relevant findings from the experiment.

2

Background and Literature Study

Wind energy has existed for a long time as a renewable energy source, like in old windmills used for milling grain and pumping water. The modern era of wind energy began in the late 20th century, fueled by the urgent need for sustainable alternatives to fossil fuels. Early large-scale turbines, often faced challenges such as reliability issues and high costs [8]. However, thanks to significant advancements in technology and engineering, wind energy has now evolved into a reliable and cost-effective power source. Today, we can even build wind farms at sea, taking advantage of the stronger and more consistent wind speeds found offshore.

Offshore wind energy has become a critical component of the renewable energy landscape [9]. Within this domain, FOWTs have emerged as a groundbreaking solution. These advanced systems enable the harvesting of wind energy in deep waters where traditional fixed-bottom turbines are not feasible, opening up new locations and possibilities for green energy generation.

2.1. Floating Offshore Wind Turbines

The concept of FOWTs was first explored in the 1990s, with the first prototype deployed in 2007. The technology has advanced rapidly, with global installed capacity projected to grow from 121 MW in 2022 to 264 GW by 2050 (out of the 2,000 GW of total global wind energy production by 2050) [9]. Unlike bottom-fixed wind turbines, FOWTs utilize floating platforms tethered to the seabed, allowing deployment in water depths exceeding 60 meters, where 80% of offshore wind resources lie [10].

While it implies massive engineering challenges, the idea is very simple: place a wind turbine on top of a floating platform and anchor it to the ground so it does not float away. Modern commercial wind turbines are predominantly designed following the upwind, three-bladed Danish configuration.

These turbines consist of three main structural components: the tower, the nacelle, and the rotor. The nacelle houses critical machinery such as the generator, which converts kinetic energy into electricity, and often a gearbox that links the main shaft to the generator. At the front of the nacelle is the hub, which supports the three blades. Each blade is made up of multiple airfoil sections that vary in chord length and thickness, optimized for aerodynamic efficiency. The rotor surface is the area swept by the blades, and it is a key factor in energy capture.

Wind turbines operate under varying wind and rotational speed conditions. To manage that, wind turbines are equipped with actuation systems like pitch motors on each blade to be rotated around its axis, and yaw motors rotates the nacelle to face the wind direction. The control system then regulates generator torque and blade pitch to optimize power output based on wind conditions. As wind speeds increase, the turbine adjusts blade pitch to maintain rated power and prevent over-speed. In extreme wind conditions, the blades are fully pitched to minimize aerodynamic loading, and the turbine is shut down to avoid structural damage.

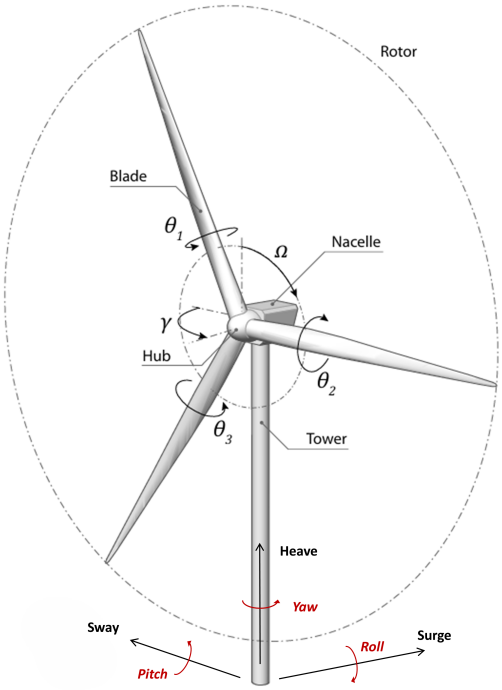

Figure 2.1: Illustration of a Wind Turbine with some of it's main components. The figure shows the degrees of freedom corresponding to blade pitch control (θ), yaw control (γ), and rotor speed control (Ω).

Among the benefits that FOWTs offer, they reduce visual impact, and mitigate ecological concerns associated with seabed disturbance. Several types of FOWT platforms exist, including spar, semi-submersible, tension-leg platforms (TLPs), and hybrid designs (see Figure 2.2). Each type employs distinct stabilization mechanisms, such as gravity, waterplane area, or mooring tension, tailored to site-specific requirements [10].

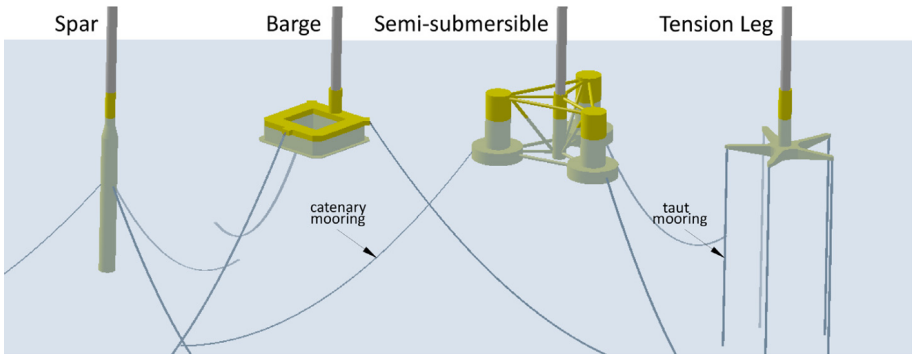

Figure 2.2: Common platform types used for FOWTs. Mooring lines secure the structure to the seabed to maintain its position. Image from [10].

However, challenges remain, including higher costs, structural complexity, and the need for robust mooring systems. The absence of a solid foundation results in a 6 DOF system which complicates the operation of the offshore wind farm (Figure 2.1). Additionally, it is currently impossible to eliminate the motions associated to waves and wind, thus understanding and mitigating the motions of a FOWT is a hot topic and should be considered in the design of an offshore wind farm [11].

The future of wind energy will heavily rely on the continued evolution of FOWT technology. With the integration of larger turbines, as well as reducing the levelized cost of energy (LCOE), FOWT farms will become not only more profitable but also an increasingly attractive investment opportunity for a wider

range of countries and private entities [12]. Industry trends suggest an emphasis on both standardization for mass production, and specialization for specific environmental or economic purposes. Novel approaches, such as multi-turbine platforms and hybrid systems combining wind and wave energy, are also being explored [10] [13].

2.1.1. Loads of FOWTs

FOWTs experience complex loading conditions which combine aerodynamic, hydrodynamic, and structural interactions. Unlike fixed-bottom wind turbines, FOWTs are subject to additional dynamics because of their floating nature.

FOWTs are subjected to various forces, which affect the motions of the platform and ultimately will alter the power output of the rotor. The aerodynamic forces are generated by wind interacting with the blades and are essentially the source of power. However, wind conditions are inherently unsteady, and the wind speed and direction fluctuations affect the loading. Similarly, hydrodynamic drag fluctuations are responsible for platform motions which influence the rotor's aerodynamic performance. Additionally, forces from the mooring lines are to be considered as well, as they constrain the location of the FOWT and can pull from different angles depending on the direction of the wind and waves. When we include the force of gravity and buoyancy we have the complete system that characterizes a FOWT. Internal stresses and deformations will arise from the interactions of these forces.

The floating platform's dynamics are characterized by the six DOFs seen in Figure 2.1:

- Translational Motions: Surge (forward-backward), Sway (side-to-side), and Heave (vertical).
- Rotational Motions: Roll (tilting side-to-side), Pitch (tilting forward-backward), and Yaw (rotation about the vertical axis).

Dynamics of FOWTs

Wave-Induced Dynamics: Studies on Spar-buoy FOWTs demonstrated how wave loads predominantly influence surge displacement and pitch and yaw rotations [14]. Other studies focused on individual challenges, like the study of freak waves (unpredictable waves with increased intensity). The low-frequency wave motions induced long-period platform motion specially when considering pitch. It was also proved that elevated waves intensify heave motion, leading to vertical movement of the floating platform [15].

Aerodynamic and Wake Effects on Wind Turbines: The aerodynamic effects on a wind turbine are mainly produced by the turbulence in the mean flow. Large scale turbulent eddies in the atmospheric boundary layer are responsible for local velocity field variations and, under specific circumstances, the meandering of the flow [16]. Moreover, wake inflow conditions within a wind farm influences platform dynamics. Wake-induced asymmetry results in uneven fluctuations in platform motions, mainly in surge and pitch. Half-wake conditions increase pitch instability, with standard deviation (STD) exceeding 30% [17]. However, at rated wind speeds, average wind speed has a more significant impact on platform motions than wake-induced variations.

Coupled Dynamic Responses: Wave effects cannot be considered on its own, but coupled dynamic responses between wind and wave effects must also be accounted for. A study with dynamic simulations under varying wind and wave conditions showed significant differences in FOWT responses: At below-rated wind speeds with constant wind conditions, damped transient surge motion was observed. In contrast, at above-rated wind speeds, the dominant motion was pitch oscillation at the platform's natural pitch period [18]. Moreover, the complexity of coupled aerodynamic and hydrodynamic effects is also highlighted in [14]. The rotor hub yaw moment is clearly dependent on the interactions between the out-of-phase rotor blade flap response and spar buoy pitch motion. The authors propose a combined use of blade pitch and generator torque as control variables to be able to provide good performance in a wide frequency range.

Thus, the motions that affect the loads of FOWTs are mainly pitch and surge [14, 15, 17, 19], with yaw being a secondary motion, and heave only relevant when the amplitude of the waves is high. Both surge and pitch motions create fluctuations in thrust and power output. High surge frequencies and amplitudes will increase fatigue loads on turbine components such as blades, shafts, and support structures. High pitch frequencies and amplitudes will incite aerodynamic fluctuations, with variations as high as

32.8% [20]. While backward pitch promotes wake recovery and average power increases, forward pitch results in elevated thrust and torque loads, but risks blade stall. Compared to surge motion, pitch-induced aerodynamic fluctuations are approximately five times larger, with power fluctuations twice as significant [20].

Effect on Performance

Several studies have analyzed the effects of the main motions in the performance of the FOWTs. An increase in thrust variation by up to 150% compared to the quasi-steady state situation when the turbine is under pitch or surge motions was observed for a 1:148 scale model of the DTU 10MW reference wind turbine [19]. A different study investigated the effects of coupled pitch-yaw platform motions with the use of numerical simulations, using a CFD-URANS approach [21]. Results indicated that platform pitching is the main influencing factor of power fluctuation when compared to yaw (Figure 2.3). Additionally, increasing the frequency of the motion will aggravate the fluctuations in both thrust and power.

In the experiment from Suzanne Hendriks, the focus was rather on the the effect of the motions in a FOWT on a stationary downstream turbine. The experiment was comprised of two scale models of the DTU 10MW setup in tandem configuration (only offset in streamwise direction). The results showed that low frequency motions had a much greater effect on the second turbine when compared to high frequency motions. Moreover, pitch was the most influencing parameter, closely followed by surge (see Figure 2.4). The effects of second turbine placement with respect to the first one were also analyzed, showing more than 15% and 50% of improvements for power and thrust respectively when the second turbine is moved 2D streamwise or 0.5D spanwise [7].

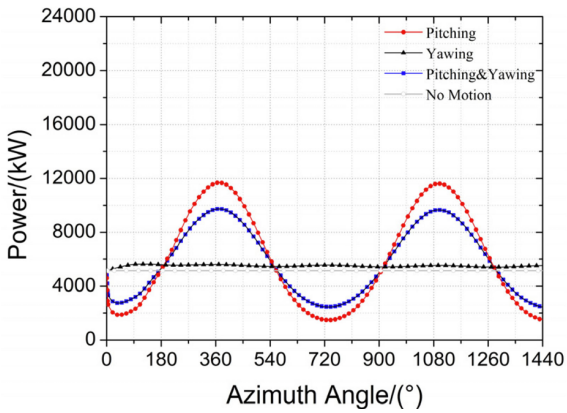

Figure 2.3: Variation in power performance for a pitch/yaw amplitude of $4°$ and a frequency of $0.1Hz$. Image from [21].

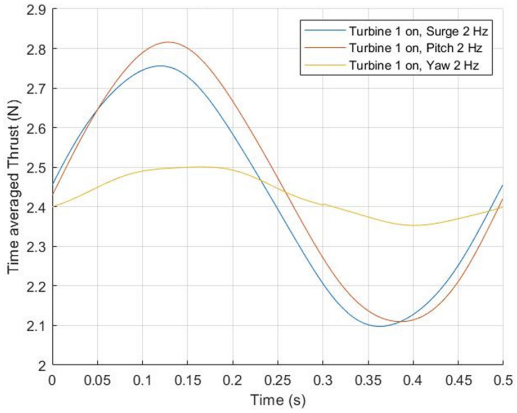

Figure 2.4: Variation in thrust performance for a normalized velocity variation of 0.05 and a frequency of $2Hz$. Image from [7].

Additionally, in a study focused on wake influence based on wind farm design, it was seen that wake recovery and power output were affected differently when considering aligned versus staggered wind farms configurations. For staggered configurations, power output depends on the geometric mean of spanwise and streamwise turbine spacings, while aligned configurations rely predominantly on streamwise spacing [22]. Interestingly, staggered configurations generally achieve higher power output due to enhanced mixing. On the other hand, vertical kinetic energy flux is more localized in aligned farms which, according to the authors, leads to faster wake recovery.

2.1.2. Wakes of FOWTs

A wind turbine generates electricity by extracting kinetic energy from the wind, which lowers the wind velocity behind the turbine. This downstream region of reduced velocity is known as the wake. It is characterized by higher turbulence levels that contribute to flow unsteadiness, which can increase fatigue loads on turbine components.

In the boundary of the wake an annular shear layer exists, dominated by a helical vortex structure (see Figure 2.5). This structure, is produced by the tip vortices of the rotating blades, which is the reason for being helical. The stability of this vortex structure plays a critical role in the development and evolution

of the wake, as the vortex will eventually break down downstream and turbulence will spread across the wake. Additionally, the hub of the wind turbine also sheds vortex structures that have an influence in the flow behind the rotor, although it is not as strong as the helical vortex. The strength of the shear layer surrounding the wake can impact wake mixing, influencing downstream flow dynamics and wake recovery [23].

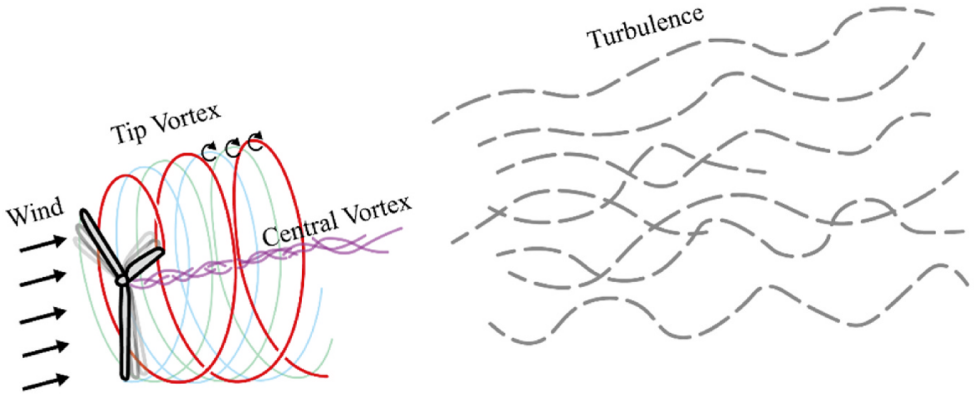

Figure 2.5: Schematic representation of the wake generated by a wind turbine. Structured vortices are observed near the rotor, while flow becomes more irregular further downstream. Visualization by [24]

Wind turbine wakes interact with downstream turbines in complex and not fully understood ways, leading to increased mechanical loads, reduced operational lifespan, and a decrease in overall energy output. A numerical study focused on the power output of the Horns Rev I off-shore wind farm connected to the Danish power system [25] showed a loss of 12% in energy yield during one simulated month when compared to a wind farm without wake effects. To mitigate the efficiency loss, and bring the cost of wind energy down, when a wind farm is designed, these wake effects are taken into consideration. However, due to economic constraints and other practical factors, such as limited available space, it is impossible to eliminate wake losses entirely [26].

Wakes are typically divided into two distinct regions:

- Near wake: It is the region immediately behind a wind turbine's rotor, where the effects of blade aerodynamics, tip vortices, and rotational forces are still dominant. This region is highly three dimensional, with complex flow structures such as root and tip vortices that quickly lose strength [27]. The near wake length is dependent on the incoming flow [28], and research in this area focuses on turbine performance and power extraction.
- Far wake: It extends beyond the near wake and is characterized by a more uniform velocity deficit and turbulence intensity (TI) [27]. The combined effects of the tower wake and the overall rotation of the wake create an asymmetric condition in the far wake, this is shown experimentally in [28]. In this region, the detailed effects of individual turbine blades are less significant, and research is more focused on turbulence interactions and the influence of turbines in wind farms, which is very relevant for optimizing wind farm layouts and energy efficiency.

The exact definition of the region is not consistent in literature, with the transition point ranging from 5D to 15D. In Figure 2.6, the far wake is even defined to start around 4D [23]. In some studies, also a middle region is considered, named as intermediate wake [29]. In these cases near wake is considered to transition after a distance of approximately 2–3D. Then the switch to far wake occurs around a distance of 7-10D. Interestingly, the inner wake reaches a far-wake state around 5D, way earlier than in the outer parts of the wake. In any case, it is safe to assume that the far wake state is fully reached by 10D.

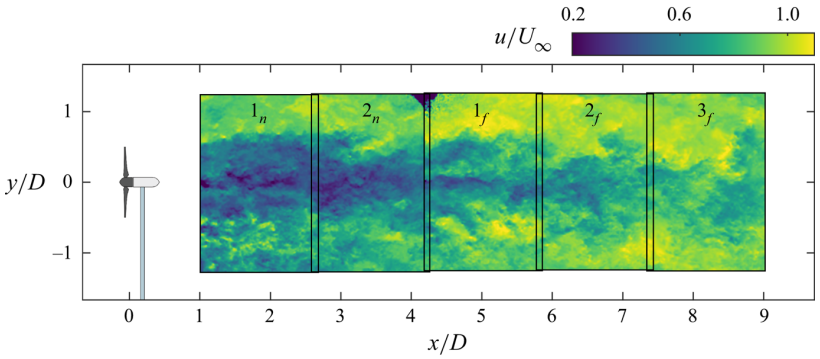

Figure 2.6: Instantaneous estimate of the streamwise velocity in the turbine wake. 1_n & 2_n denote the near wake, while $1_f, 2_f,$ & 3_f denote the far wake. Visualization by [23]

Mixing Properties of the Wake

The wake flow structure of a wind turbine is strongly influenced by the rotor tip-speed ratio, which determines the stability and intensity of vortices. When wake instability increases, vortex leapfrogging occurs, a phenomenon where vortices interact and exchange positions along the free-stream before breaking down [30]. This process enhances wake mixing, as the vortex coherence is lost, resulting in increased turbulence and re-energizing of the wake [31].

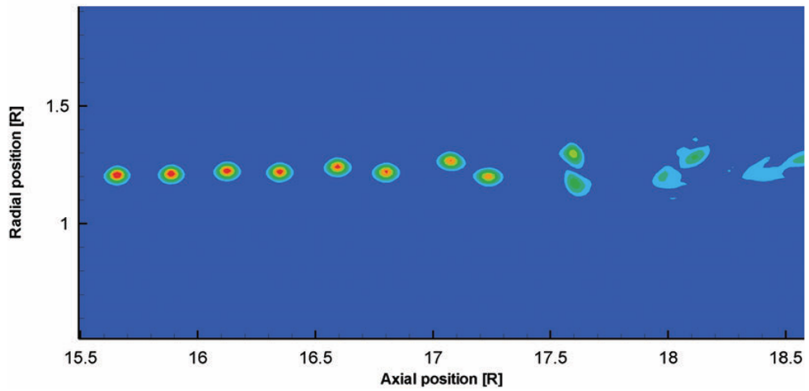

Figure 2.7: Visualization of leapfrogging phenomena of two vortices. Image from [32]

Atmospheric conditions play a significant role in shaping the wake of wind turbines, the incoming turbulence intensity and overall flow quality affect the wake of turbines as studied in [23]. Particularly in offshore environments where the surface roughness is lower than in land, meandering is observed as a key feature of the flow. The phenomenon is initially caused by the natural oscillations within the wake and highly amplified by the large eddies present in the atmospheric boundary layer. Experiments have shown that the Strouhal number associated with wake meandering remains constant at around 0.25 [16], regardless of inflow velocity. Whether this effect affects positively or negatively the power output of wind farms was not discussed in literature, however the increase of instabilities surely poses a challenge for control and structural loads for wind turbines.

Motions inherent from FOWTs such as pitch or surge affect the wake by modifying the already existing vortices and wake shape, and by introducing new turbulent structures. In example, surge motion influences the blade-tip vortex travel speed causing periodic stretching and contraction of the spiral wake vortex following the surge frequency [20]. Additionally, vortex rings are formed periodically further altering wake behavior and adding complexity to the system. Forward motions result in wake expansion and enhanced mixing, while backward motions leads to reduced vortex interaction and wake contraction. These effects contribute to a narrower wake with increased energy concentration in its outer regions [33].

Wake Recovery

Wake recovery is a critical parameter for wind farm performance, faster recoveries can allow for smaller distances between turbines increasing wind farm efficiency and energy outcome. The wake recovery process in floating wind turbines differs from that of fixed-bottom turbines, particularly concerning different motions. Some studies indicate that wake energy recovery is more efficient in FOWTs at 8D–10D downstream, while at 4D–5D, fixed-bottom turbines tend to recover more energy [24, 34]. These findings emphasize the need to optimize turbine spacing and wake interactions in floating wind farm layouts.

However, there are studies relating TI directly to increased mixing in the wake that suggest that, regardless of the diameters downstream and the motion applied on the platform, FOWT should experience faster wake recovery than conventional bottom-fixed turbines [22, 35]. Additionally, in another study it was confirmed that tip-vortex breakdown significantly contributes to wake recovery [31]. Since there are additional vortex structures being created by the motions of the platform, it is expected to see faster recovery for FOWTs. As it was explained in [36], ”the movements of the platform enable a faster transition to the far-wake, meaning that the recovery processes start closer to the rotor”.

2.2. Previous Studies on Offshore Wind Energy

Wind energy is a trendy rapidly developing field, yet experimental investigations remain relatively limited. The complexity of experimental setups, often involving rotating components, large-scale models, or significant scaling ratios, poses substantial challenges. These factors contribute to the difficulty of conducting accurate and controlled studies, making wind energy a particularly demanding area of research.

2.2.1. Horizontal Axis Wind Turbines

As presented by a study looking into existing data from experiments and simulations; more efforts need to be placed in wind energy research. The focus of the study is understanding how the wake of wind turbines under controlled conditions dissipates downstream [27]. While a substantial amount of data and research is available for analysis, the authors find the quality of the data lacking. Numerical methods show reasonable agreement with experimental results, but only when certain assumptions or simplifications are applied, which not always hold across different flow conditions. Additionally, the variation in wind tunnel setups and rotor models presents a challenge in combining and comparing the available knowledge.

To decrease the difficulty of testing complicated wind turbine rotors and simplify the analysis porous disks are often used as physical actuator disk equivalent for wind turbines (see Figure 2.8). Porous disk can replicate the wake of a rotating wind turbine when modeled properly. This often requires testing several disks and comparing them with the real scaled model of the wind turbine. This is precisely what is done in a study where similarities and differences of two porous disks, one solid disk, and a model wind turbine are assessed by wind tunnel testing from the near wake to up to 30 diameters downstream [28]. This study showed that, while one of the disks was able to closely replicate the wind turbine wake, the asymmetric wake shape of the scaled model might be impossible to ever achieve with a porous disk. The necessity of selecting a correct porous disk design is further highlighted as the authors noted that only one of the porous disks was producing vortex shedding, and the turbulence in the wake varied depending on the design.

While porous disks might be a valid solution for the medium to far wake of wind turbines, they cannot be used to analyze the near wake or a HAWT, as all the individual components such as blades, hub, and tower are not represented in the flow. Experiments focussed on the vortex wake behind the rotor of the turbine, like in [37], are forced to use model wind turbines. By having all the components present, their experiment was able to reveal the presence of an ”important sheet vortex structure downstream the hub”. The results showed that tip vortices from the blades expand radially, increasing the flow tube diameter, contrary to linear propeller theory.

A more specific study into tip vortex development is performed up to 5 diameters downstream by [31], where leapfrogging location and effect on the wake is investigated experimentally. By analyzing the wake axial velocity and the pressure and stagnation enthalpy, it was observed that the leapfrogging

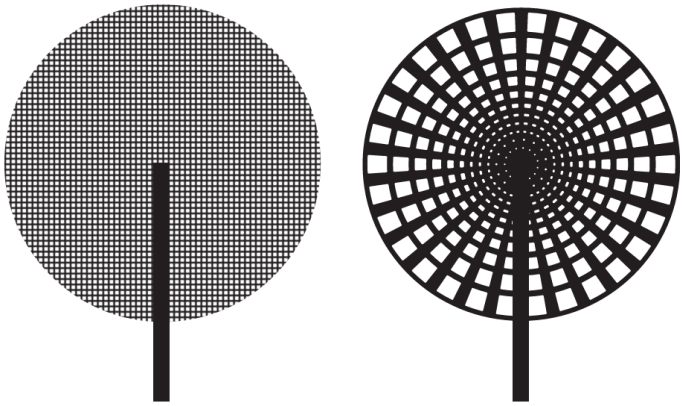

Figure 2.8: Porous disks designs used in [28] to mimic the wake characteristic of a scale wind turbine.

phenomena impacts the momentum deficit recovery of the wake. This essentially means that there is a re-energizing region after the vortex coherence is broken, which affects positively the wake recovery.

In addition to the main area of interest, a direct relationship between general wake instability and the rotor tip-speed ratio was found in [31]. A different study, rather than looking into the velocity relative to the blade, the freestream velocity effect was taken into consideration through the Reynolds number [29]. The effects of high Reynolds numbers (from 2.7 to 7.2 x10^6) were analyzed in a wind tunnel experiment, expecting to obtain a relation to instabilities like in the previously explained study. However, results only showed variations in the wake core of the near wake, mainly in axial velocity. There was self-similarity in all the other locations downstream, hinting to very little effect due to the Reynolds number.

To fully understand HAWTs, studies have also focused in the rotor and wake interactions in wind farms. A study performing steady-state and dynamic simulations concluded that efficiency depended on both the spacing between turbines as well as the wind regime they experience, making geometric distribution the most sensible design parameter to adjust [38]. It was shown how the energy production was reduced due to single wakes or interaction between multiple wakes considerably reducing the speed and and increasing turbulence downstream. Some other researchers decided to focus their wind farm study into wake meandering and their effect downstream by means of a 3×3 wind farm in an atmospheric wind tunnel [16]. This effect, induced by large-scale turbulent eddies in the flow, was amplified for the downstream wind turbines inside the farm, showing higher meandering strength.

2.2.2. Floating Offshore Wind Turbines

FOWTs introduce a new level of complexity: mooring lines, incoming waves, and resulting motions all affect the performance of the turbine, and indirectly the wind farm. Partially coupled analysis can be useful to understand certain characteristics of interest, but the best solution is a fully coupled aero-hydrodynamic investigation [39]. Unfortunately, not even previous HAWT aero-elastic studies will be accurate when the operational conditions of FOWTs are considered [40, 41].

A more complicated system requires of specific modeling to accurately reflect the motions experienced by a FOWT, and the higher performance computing resources that come together with it. Previously, Blade Element Momentum (BEM) theory served as a valid solver for HAWT, however for a turbine subjected to motions, BEM over-predicts the maximum amplitude of the motion by more than a 50% [42]. This is proven in an investigation comparing BEM to a state-of-the-art vortex solver able to perform aero-hydro-servo-elastic simulations for HAWTs and FOWTs. Large Eddy Simulations (LES) are a good solution for analyzing offshore conditions: in [43] it successfully predicted wake pulse modes induced by motions and the meandering mode originating from yaw and sway. Different inflow TI and length scales were analyzed for a FOWT showing that higher TI had a stabilizing effect on the wake, smoothing out high frequency levels. The option of changing flow conditions quickly and precisely is one of the advantages that numerical simulations offer, however it is important to note that there are limitations. For example, in [43], linear and axis-symmetric assumptions simplified the model and guaranteed efficiency.

Implementing motions to an already rotating component can increase the complexity of experimental campaigns. Researchers from different institutions have taken different approaches, motivated by their main motions of interest. For a simple one dimension surge motion, a linear motor is used in [44]. This is a cost effective solution, but when more motions are required a second actuator is required. Researchers in Politecnico di Milano used a setup with two hydraulic actuators that allow for both pitch and surge [45, 46, 33, 47]. In their lasts iterations of the set up, hardware-in-the-loop (HIL) was introduced; a real time system that is able to measure the aerodynamic loads in the FOWT and reproduce the combined motion of waves and wind. To simulate other motions and widen the possibilities during studies, 6-DOFs systems can be used. For example, more HIL tests were conducted by Politecnico di Milano, this time using a 6-DOFs parallel kinematic robot [48], and a 6-DOFs commercially available Quanser hexapod is used for experiments in TU Delft [19, 7].

FOWT motions affect both the wake of the turbine and the performance of the turbine in motion itself. In [19], the aerodynamic response of a 1:148 scale model of the DTU 10MW reference wind turbine rotor is studied when subjected to prescribed motions. The author uses the parameter "reduced frequency" (f_r) and "normalized velocity variation" (ΔV^*) as a non-dimensional way of describing the strength of the motions (seen also in [33, 7]):

$$f_r = \frac{f D_{rotor}}{U_0} \tag{2.1}$$

$$\Delta V^* = \frac{\Delta V}{U_0} \tag{2.2}$$

For reduced frequencies above 1.2, it was observed that thrust variation increases by up to 150% compared to the quasi-steady behavior when there is pitch, surge, or yaw motions, irrespective of motion amplitude. Additionally, 6-DOFs FAST-derived simulations were imposed by the Quanser hexapod to explore the validity of the setup and the model. The obtained results presented reasonable agreement with the simulations, confirming the coherence of the experiment.

The effects of surge motion on FOWTs have been investigated through both experimental and numerical studies. Rotor thrust force measurements indicate that quasi-steady theory accurately predicts turbine response up to a reduced frequency of 0.5, with wake energy increments aligning with blade tip motion [33, 46]. Compared to bottom-fixed turbines, a study observed that, FOWTs in surge motion exhibit reduced Reynolds shear stress, which would lead to longer wake dissipation distances and potentially require increased spacing between turbines in wind farms [49]. However, further investigations using actuator disk models suggest that, under certain extreme motion regimes, surging turbines may exhibit mildly enhanced wake characteristics, with reduced turbulence intensity and turbulent kinetic energy (TKE) in most cases [44]. This is also backed by LES performed on surging FOWTs [50]. In this study, faster wake recovery observed in surging turbines is not due to an increase in turbulence levels, as previously assumed, but rather results from enhanced advection caused by surge-induced periodic coherent structures [50].

Studies indicate that pitch motion has a greater influence on wake characteristics than surge, significantly altering the velocity field. At higher pitch frequencies, wake velocity fluctuations increase considerably compared to low-frequency cases, an effect not observed in surge motions [7]. This stronger wake influence means that floating wind farms might require greater spacing between turbines to allow sufficient wake recovery. Exactly this is what is suggested in a study covering free-pitch motion of a FOWT [34]. Vortex-based studies confirm the high velocity fluctuations, however they reveal that the turbulence induced by the pitch oscillations will promote faster vortex breakdown, leading to a more mixed and dynamic wake [42]. Other numerical simulations, like the $3DM\_FP$ model used in [51], are being developed trending high accuracy (97.6% match with experiments at distances up to seven rotor diameters) with low error percentages (maximum of 5.3%), and will be used to investigate further the effects of pitch on a FOWT wake in future studies.

2.2.3. Floating Offshore Wind Turbine Interactions

Limited research exists on floating offshore wind farms, with most studies relying on simulations that incorporate assumptions and simplifications to optimize computational efficiency. While more experimental studies are expected in the future, the few available experiments currently serve as valuable guidelines for current research and to shape expectations.

Experiments and simulations on tandem FOWTs have revealed significant wake dynamics and performance implications for the downwind turbine. Wind tunnel experiments measured the wakes of both bottom-fixed and freely oscillating tandem turbines, as suspected the turbulence characteristics of the upstream wind turbine far wake strongly influence the near wake of the second turbine. Reynolds stresses and turbulence production in the near wake of the downwind turbine were found to be damped, with smaller vertical fluctuations but an increase in the mean vertical velocity component [34]. A follow-up study confirmed that pitch motion causes an upward displacement in all velocity components of the wake, reducing kinetic energy in undisturbed flows above the turbine [52].

Numerical simulations using Large Eddy Simulation coupled with a vortex particle-mesh method have been applied to tandem FOWTs to investigate wake aerodynamics. These studies emphasize the impact of different turbulent inflow conditions on wake meandering and turbine performance, demonstrating the importance of accurately modeling inflow turbulence for reliable predictions [53]. A recent study uses active sway control strategies for enhancing wake recovery at the wind farm level by artificially creating wake meandering. The effects on a downstream turbine were positive: the wake of the first turbine recovered faster and power output was increased, particularly in low-turbulence environments. However, the effectiveness of active control strategies depends on wake instability properties and inflow turbulence levels, underscoring the complexity of wake interactions in floating wind farms [54]. Positive wake recovery effects are also seen in [55], as vortex structures are broken down faster with the introduction of floating motions.

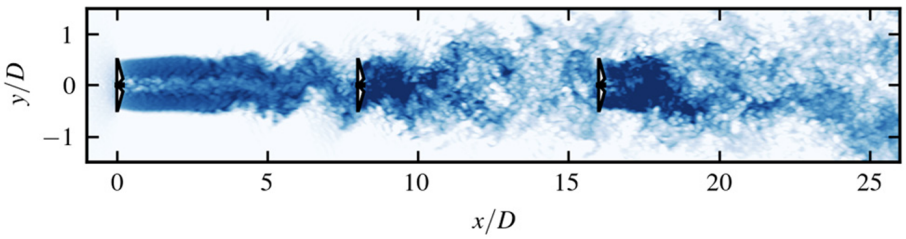

Figure 2.9: Streamwise velocity deficit at hub-height plane used to visualize the effects of wake and rotor interaction for wind turbines in line configuration. Retrieved from [54].

However, the same study also did simulations of five floating wind turbines in a row and revealed more dynamic interactions. In below and rated wind conditions, the relative power of the fourth and fifth turbines is notably lower in floating farms. Additionally, in above-rated wind conditions, floating turbines exhibit greater fluctuations in both power and thrust compared to bottom-fixed counterparts (about 50%), with these variations intensifying further downstream [55]. This indicates that a loss of efficiency in floating farms is unavoidable unless the flow is re-energized with bigger spacings between turbines or active control methods. The reduction of available energy for power production is discussed briefly in [52], where the authors believe that worse wake recovery should occur. It is important to remember at this point, and as previously mentioned, the little experimental data available and that simulations make assumptions which lead to the questioning of these statements.

Focusing in mean thrust and power production of the downstream turbine, simulations indicated an increase relative to operation behind a fixed turbine due to the enhanced wake mixing from the upstream FOWT [55], as seen in exploratory experiments [7]. However, the power performance of the second turbine varies based on its wake inflow condition. When positioned just outside the wake (1D lateral offset), power output follows a similar trend to free-stream conditions but is not symmetrical across lateral positions. Furthermore, it was observed that in half wake conditions the effect varied whether the half wake was incoming from the right side (upwards flow) or left side (downwards flow) of the rotor [17]. The experimental study [7] also shows that lateral positioning affects thrust forces, with thrust nearly doubling at 0.5D lateral offset and increasing further at 1D lateral offset.

2.3. Common Experimental Measuring Techniques

Among the various measurement techniques available, Hot-Wire Anemometry (HWA) and Particle Image Velocimetry (PIV) are the most commonly referenced in the literature. This section provides an overview of both methods to build an understanding before selecting the most suitable approach for the current study.

2.3.1. Hot Wire Anemometry

Hot-Wire Anemometry is a well-established technique for the measurement and analysis of velocity fields. This technique is known for its ability to provide continuous output signals and detect very rapid fluctuations in the velocity field.

The principle of HWA is based on the cooling of a hot wire when exposed the colder flow stream. The predominant method of operation is to maintain the wire at a constant temperature using a Wheatstone bridge circuit, known as the Constant Temperature Anemometer (CTA). The velocity of the flow will affect the convective cooling rate, and it must be balanced by the electrical energy input in accordance with [56]:

$$I^2R = hA(T_W - T_f) \tag{2.3}$$

where, (I^2R) represents the electrical energy input, (h) is the convective heat transfer coefficient, and ($T_W T_f$) represents temperature difference between wire and fluid.

Initial calibration to set all parameters with precision is a must, but additionally, the wire probe resistance will increase as the temperature increases. Thus as temperature changes and affects the resistance, the bridge will become unbalanced. A DC amplifier can sense the unbalance and produces a change in voltage, which will change the current through the wire to keep the bridge balanced. A relation between output voltage (E) and fluid velocity (U) named “King’s Law” is given by:

$$E^2 = A + BU^n, \tag{2.4}$$

where, A, B, and n are coefficients that can be determined during the initial calibration with a pitot tube.

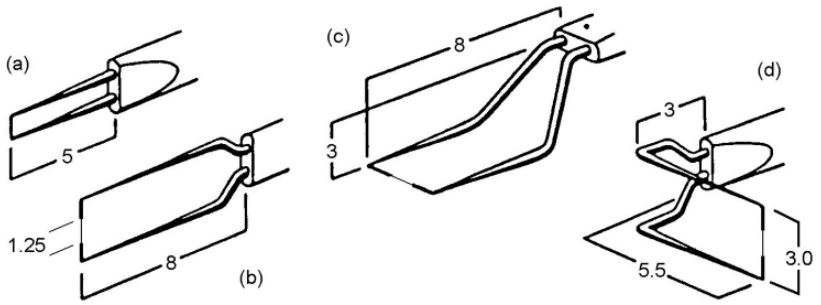

Figure 2.10: Types of hot wire probes from DANTEC, D = 5 µm, ℓ = 1.25 mm.(a) miniature, straight, (b) ordinary, straight, (c) boundary-layer, straight, (d) straight 90◦ probe with wire perpendicular to the probe axis. Retrieved from [57].

Commercially available hot-wire probes are designed to measure one, two, or three components of the velocity vector at specified points within the flow field. Despite of long calibration procedures in some cases, these instruments are valued for their data acquisition simplicity and ease of signal processing. For example, it is suitable for measuring velocities at precise locations within a flow field, and capable of detecting velocity fluctuations at frequencies up to several hundred kHz. This is a much higher temporal resolution than other measuring devices. Some other advantages discussed in the book from H.H. Bruun [56] are:

- Cost: HWA systems are relatively cheap in comparison to other techniques.
- Accuracy: very accurate results (0.1-0.2%) in carefully controlled experiments.

- Size: Even though it is an intrusive method, the probe and arm are very compact and minimally interfere with the flow. Hot-wire sensor are typically about 5 μm in diameter and 1.25 mm long.
- Signal-to-noise ratio: Hot-wire anemometers have very low noise levels. A resolution of one part in 10,000 is easily accomplished.

On the other hand, as previously mentioned, the accurate measurements require careful calibration to account for variations in wire properties and environmental conditions. But also, it has limitations, as turbulence intensities above 35% can introduce significant error [57].

2.3.2. Particle Image Velocimetry

Particle Image Velocimetry (PIV) is a cutting-edge flow measurement technique used to visualize and measure fluid flow fields. PIV operates by introducing tiny tracer particles into a fluid and capturing their location over time using advanced imaging techniques. By analyzing the displacements of these particles, the velocity vector of each particle in the fluid can be calculated. The process requires illuminating the fluid with a sheet of laser or LED lights and using (one or multiple) high-resolution cameras to visualize particles at two time intervals. Through image processing, the displacement of particles is converted into velocity vectors. It is assumed that the particles accurately follow the fluid's motion.

One of the most significant advantages of PIV is its non-intrusive nature. Unlike traditional methods such as pitot-static tubes or hot-wire anemometers, PIV does not disturb the flow field, making it especially suitable for complex or high-speed flows. PIV has also advanced to measure three components of velocity within a plane or volume, expanding its applicability to study specific flow phenomena [58].

Types of PIV Techniques:

- **Planar PIV (2D PIV):** Planar Particle Image Velocimetry measures two velocity components (typically u and v) within a two-dimensional plane of the flow field. Seeding particles are illuminated by a thin laser sheet, and two successive images are captured with a short time interval Δt. The resulting particle displacements are computed using cross-correlation within small interrogation windows, from which the velocity vectors are calculated. This classical PIV technique is limited to in-plane velocity components, with out-of-plane components being lost due to perspective distortion.

  This technique is applied in [37], with focus in radial and axial components of velocity of the vortex wake of a wind turbine. A laser is shot through an optical opening and a single camera captures up to 2D downstream of the rotor in six smaller planes [37]. On other experiments, span-wise and stream-wise direction were the priority, thus the laser sheet was placed in the horizontal plane [16]. In the wind tunnel experiment from A. Fontanella et al., blade tip vortices of a wind turbine in surge conditions are visualized thanks to planar PIV [33]. In these experiments, the double-pulsed laser sheet and the two adjacent cameras are adjusted to capture the wake structure at various distances downstream, providing insights into the development of vortices.

- **Stereo PIV (SPIV):** This technique extends planar PIV by adding a stereoscopic imaging setup. Using two cameras at offset angles, SPIV captures three velocity components in the illuminated plane. By applying calibration to the captured images, the camera views are mapped onto a common 3D coordinate system. This method enhances spatial resolution and it has been widely used for the study of wind turbine wakes.

  For example, SPIV was used to investigate the influence of pitch motion on the wake of a model wind turbine. This method was able to capture the averaged development of the blade tip vortices under both pitching and motionless cases [52]. SPIV was also used for free pitch wind turbines in tandem formation. Here, the turbulence and wake characteristics of the flow at different stream locations was studied [34]. In [59], planar PIV was initially used to study helium-filled soap bubbles (HFSB) as tracers for PIV in large-scale wind tunnels, however in a later iteration the set-up was upgraded to account for the third component of velocity, which contributed to a more thorough and insightful analysis.

- **Tomographic PIV:** Tomographic PIV extends the PIV technique into three dimensions by employing 3 to 4 cameras viewing a seeded flow volume from different angles. A thick laser sheet or illuminated volume excites the particles, and the camera images are used to reconstruct a 3D

distribution of light intensity (voxel volume). Velocity vectors are then obtained by applying 3D cross-correlation between consecutive volumes, yielding all three components of the velocity field in a 3D space. Tomo-PIV provides high spatial resolution and is well suited for analyzing complex flow structures such as vortex interactions, shear layers, and turbulence.

The method was introduced in 2006, using the reconstruction algorithm Multiplicative Algebraic Reconstruction Techniques (MART). The authors noted that "The effect of the number of cameras is clear: adding camera gives additional information on the object, which increases reconstruction accuracy." [60]. In the later years, this method has been used across different disciplines from which inspiration can be drawn. In example, tomographic PIV has been used to visualize the flow field around a cyclist [61], with the introduction of a robotic arm, the experiment obtained superior optical access to complex geometries such as concave or enclosed regions.

- **3D PTV:** This method uses a similar setup to Tomographic PIV, however the reconstruction process is different. It is purely a particle-based technique using Iterative Particle Reconstruction (IPR) and making use of the time-information for track reconstruction. In 3D-PTV, particles are identified based on their peak intensity in images, and then their positions are triangulated in 3D space. This technique is particularly effective in capturing detailed flow structures and allows for the reconstruction of complex dynamics. However, it can be sensitive to noise and may require high particle seeding density to obtain accurate results [62].

  In [13], a laser sheet is used instead of LEDs. To increase the experiment region, the sheet is thickened by a set of optics bringing the thickness to 30mm. In other experiments [7], [35], LEDs illuminated a much bigger volume. This was a design necessity, as the studies were based on the wake of medium sized wind turbine models under imposed motions .

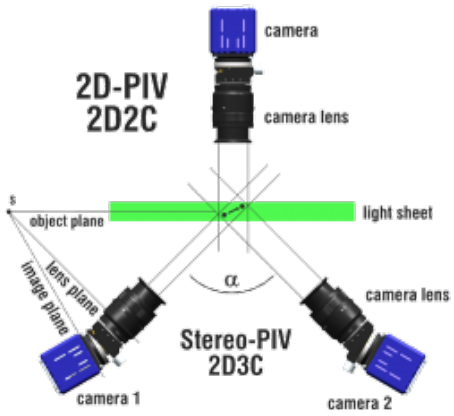

Figure 2.11: Common setups for 2D PIV and Stereo PIV. Retrieved from [63].

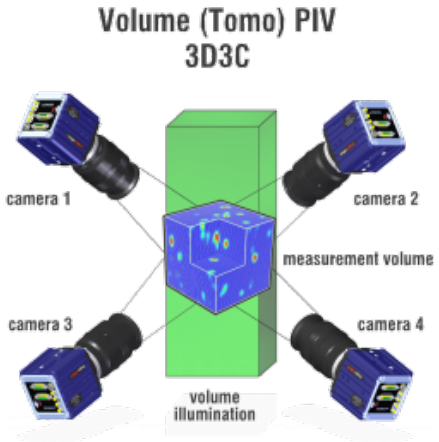

Figure 2.12: Common setup for Tomographic PIV and 3D PTV. Retrieved from [63].

Several methods and techniques are applied for introducing particles in the flow. Using oil droplets as the light-reflecting tracer particles is considered as "the most common method of producing micrometer droplets for PIV" [59], in [16] a particle size of 1-5µm was achieved using this substance. Another elegant solution for PIV is metal oxide powders, as they are inertness, have high melting point and generally have a low cost. Due to possible agglomerations the powder must be carefully introduced in the flow by shaking and braking up these particles prior to the seeding, or by aerating the powder with a vertical tube creating a fluidized bed and then forcing the flow though a nozzle into the fluid [64].

For bigger volume methods, like 3D PTV, Helium Filled Soap Bubbles (HFSB) are commonly used due to their bigger size while being neutrally buoyant. These bubbles are bigger and a seeding concentration of 1 bubble/cm3 is usually good enough [65]. The NLR bubble generator is able to consistently produce 10 to 50 thousand bubbles per second with a diameter between 0.42-0.6 mm [59]. Those bubbles were introduced in the settling chamber of the wind tunnels, however in certain situations there is a benefit in introducing them directly in the test section like in [35].

3

Methodology

The experimental setup consists of a scaled wind turbine model mounted on a six-degree-of-freedom hexapod and tested in the Open Jet Facility (OJF) at Delft University of Technology. The methodology closely follows that of [7] and [19], as this research builds upon and extends those previous studies.

Flow field velocity measurements and wake characterization are performed using the 3D PTV technique with HFSB as tracers. LaVision Davis10 software is utilized to calibrate, capture, and post-process the flow field of interest. Six different volumes are measured, requiring of three traversing system movements, quadruplicating the measured size from [7].

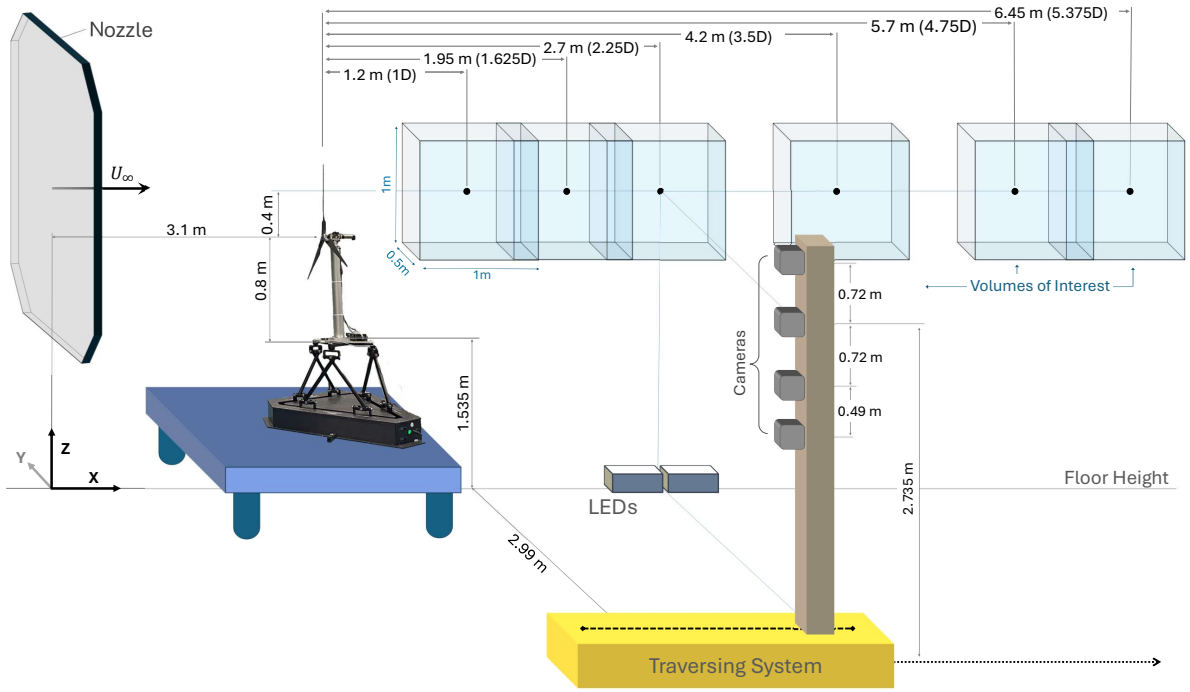

Figure 3.1: Schematic of the experimental setup used in this study. Cameras and LEDs were strategically positioned at varying distances from the rotor to capture different measurement volumes within the wake.

For consistency purposes: the streamwise direction is defined as the positive X-axis, the spanwise direction, towards the left when viewed from the exit of the wind tunnel nozzle, as the positive Y-axis, and increasing vertical direction as the positive Z-axis.

3.1. Experimental Setup

3.1.1. Wind Tunnel

The experiments were conducted in the Open Jet Facility (OJF) at Delft University of Technology, a closed-loop, open-jet wind tunnel. The OJF features an octagonal nozzle measuring 2.85m × 2.85m with a contraction ratio of 3:1, directing airflow into a 13m-long, 8m-high open test section. Powered by a 500kW fan, the tunnel can achieve wind speeds up to 35m/s, although the experiments performed were in the range of 4m/s freestream velocity. The OJF includes a diffuser, corner vanes, fine mesh screens to reduce turbulence, and a cooling radiator to maintain stable flow conditions. Thanks to these features, a turbulence intensity of 0.5% up to 1m from the nozzle exit and below 2% at 6m downstream can be achieved [31]. As a later addition to the initial wind tunnel design, the settling chamber is equipped with a seeding rake for Particle Tracking Velocimetry measurements, which slightly increases the turbulence intensity to 0.8%.

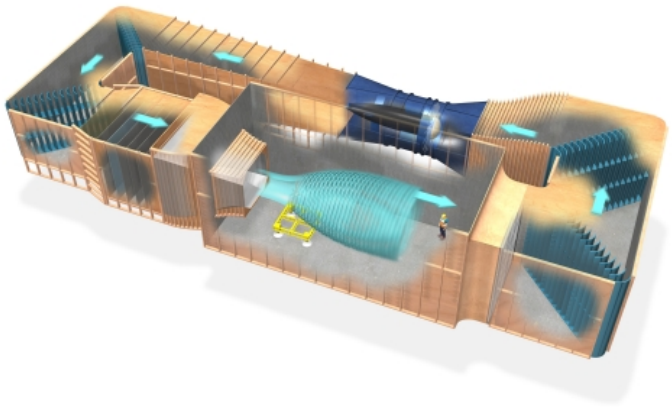

Figure 3.2: Visual representation of the TU Delft Open Jet Facility, showing key components such as the fan, test section, and turning vanes. Retrieved from [66].

3.1.2. Wind Turbine Model

The wind turbine model used in this setup is a 1:148 scale version of the DTU 10MW reference wind turbine (RWT) [67]. Designed as a three-bladed upwind rotor, it operates at a velocity scale of 1:3. The rotor is constructed from carbon fiber layers bonded with epoxy resin, resulting in a lightweight but rigid structure. It features a static blade pitch of 0°, ensuring consistency in aerodynamic performance. The rotor is powered by a Maxon EC-4pole 30200W servomotor coupled with a Maxon GP32C5 8:1 gearbox, which regulates speed through a Maxon Escon 7010 servo drive. The nacelle and rotor assembly are mounted on a stiff cylindrical aluminum tower designed to limit deflections and vibrations. The tower's has a fore-aft natural frequency of 12.5 Hz which is well above the tested motion frequencies, avoiding resonance effects with the 1P and 3P frequencies of the rotor.

The wind turbine model follows a performance-oriented scaling approach rather than a purely geometric one, prioritizing accurate thrust force reproduction over Reynolds number matching. Due to the low Reynolds number (Re < 100k) at model scale, standard full-scale airfoils would perform poorly. Instead, the SD7032 airfoil, designed for low-Reynolds applications, was chosen to ensure aerodynamic similarity with the full-scale turbine (Re ≈ 1.5×10^7). This approach ensures that the lift (C_l) and drag (C_d) coefficients at model scale closely match those of the full-scale rotor at operational conditions. While neither Froude nor Reynolds scaling is perfectly matched, the selected 1:148 length scale and 1:3 velocity scale provide an optimal tradeoff between aerodynamic fidelity and practical testing constraints. Numerical validation of the aerodynamic performance was carried out in both wind tunnel testing, and with a FAST model incorporating the scaled blade polars, confirming that the chosen scaling methodology effectively reproduces the thrust, power, and torque characteristics of the full-scale wind turbine [68].

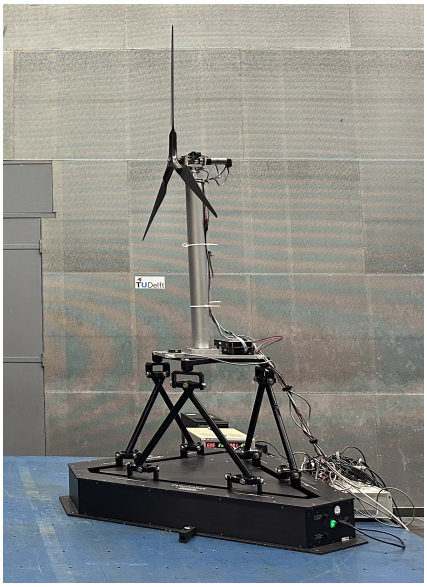

Figure 3.3: DTU 10MW Scale Model and Quanser Hexapod.

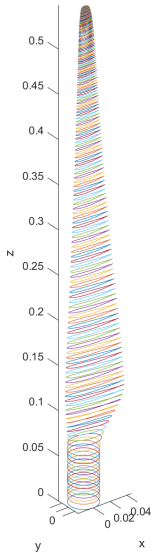

Figure 3.4: Blade geometry as designed by [68].

Parameter	Value	Unit
Rotor Diameter	1.2	m
Hub Height	0.8	m
Blade Pitch Angle	0	deg
Tilt Angle	0	deg
Rated Thrust	0.012	kN
Rated Torque	0.529	kNm
Design TSR	7.5	-
Hexapod Height	0.75	m

Table 3.1: Parameters of the DTU 10MW Scale Model.

The blade geometry as seen in Figure 3.4 shows a region where the airfoil is circular (r/R < 0.18). Later it gradually transitions to the SD7032 airfoil profile. This circular profile, which surrounds the hub, does not extract energy from the flow as an streamlined profile would, thus it does not slow down the flow. This will become evident in the analysis of velocity profiles in later sections, where high velocity will be experienced in this region with respect to the rest of the wake.

3.1.3. Hexapod

The experiments described in this thesis that required motions utilized a six-degree-of-freedom parallel kinematics robot, commonly referred to as a hexapod, to replicate such floating wind turbine motions. Specifically, the commercially available Quanser Hexapod was used, offering advantages such as compactness, lightweight design, and ease of transport, allowing for quick setup and potential replication in different test facilities. This system was chosen over standalone, custom-built alternatives due to its precision and reliability. In previous experimental campaigns [19], tests were conducted to evaluate the hexapod's capabilities and limitations beyond its standard specifications, ensuring accurate motion tracking during the experiments.

The Quanser Hexapod is capable of handling payloads up to 100 kg, with a maximum motion frequency of 15 Hz under no-load conditions and small displacements. However, when supporting a rotating turbine, these limits are reduced. Calibration, performed via a Simulink model provided by the manufacturer, was carried out after each test to maintain precise positioning. The workspace of the hexapod is constrained to approximately ±10 cm for surge and sway, ±5 cm for heave, and rotational limits between 10° and 25°, with yaw allowing for the largest motion range [69]. Prior assessments established that with a rotating turbine at rated wind speeds, the maximum frequency was limited to 5 Hz. Motion constraints were also determined, with maximum translation amplitudes of 75 mm at low frequencies and 10 mm at maximum frequencies, while rotational amplitudes ranged from 10° at low frequency to 1° at maximum frequency.

3.1.4. 3D PTV-Specific Equipment

As briefly discussed previously, a seeder is permanently existing inside the settling chamber of the TU Delft OJF wind tunnel. The seeder is able to produce HFSB with a mean diameter of 300 µm. Helium is used to achieve neutral buoyancy so that the particles can follow the motion of the flow. The seeder can be seen in Figures 3.5 & 3.6. Although the seeder dimensions inside the settling chamber are 2m height x 1m width, as the nozzle contracts, the bubbles reach an effective area of about 1.2m x 0.6m.

Figure 3.5: Close up of the OJF Seeder inside the settling chamber. Image retrieved from [13].

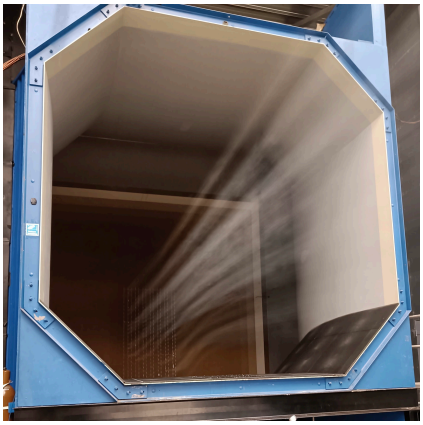

Figure 3.6: HFSB exiting the wind tunnel nozzle.

In order to capture the bubbles as the flow moves them downstream, high speed cameras are used. Four FASTCAM MINI AX100 cameras are used (Figure 3.9), two equipped with 50mm lenses and the other two with 60mm lenses, due to the limited availability of 50mm lenses. The cameras have a sensor size of one MegaPixel, with a pixel pitch of 20 microns, and a capability of shooting at 4000fps, or even higher when operating at reduced resolution. Additionally, their gigabit Ethernet interface enables rapid data transfer to the acquisition PC, which reduces wind tunnel time loss.

Complementing the high-speed cameras, the HFSB are illuminated with two LaVision LED Flashlights (Figure 3.7) to enhance image sharpness and guarantee high-quality data acquisition. Both the LEDs and the high speed cameras are controlled from the acquisition pc with the commercial software LaVision Davis v11. This versatile platform allows for easy calibration, real-time adjustments, preliminary data analysis, and comprehensive post-processing. All commands are then synchronized using a Programmable Timming Unit (PTU) from LaVision (Figure 3.8).

Figure 3.7: LaVision LED Flashlight.

Figure 3.8: LaVision PTU-X High-Speed Controller Unit.

Figure 3.9: FASTCAM MINI AX100 High Speed Camera.

Additionally, a traversing system facilitates easier downstream movement of the setup. The cameras and other components are mounted on top of the device, and an interface on the wind tunnel PC controls the system's movement in the X and Y directions. The system was used to move in the X direction without requiring PTV recalibration after each volume. With a maximum range of 1.5m, the traversing system enabled the measurement of three consecutive volumes.

3.1.5. Setup and Volume of Interest

By assuming symmetry, the focus of the experimental volume can be limited to only half of the wake. However, since the wake expands and a velocity gradient exists between the wake and the freestream region, an area beyond the blade-tip remains relevant for understanding wake recovery. In this study, a region extending approximately 0.2D beyond the wingtip is considered. Therefore, a minimum region of 0.7D (0.84m) is required for a high-quality analysis. To ensure the entire hub is included, an additional 0.1m beyond the blade root was incorporated. Finally, rounding up and accounting for potential misalignment during setup, the total volume considered was 1m in both height and stream direction (see Figure 3.10).

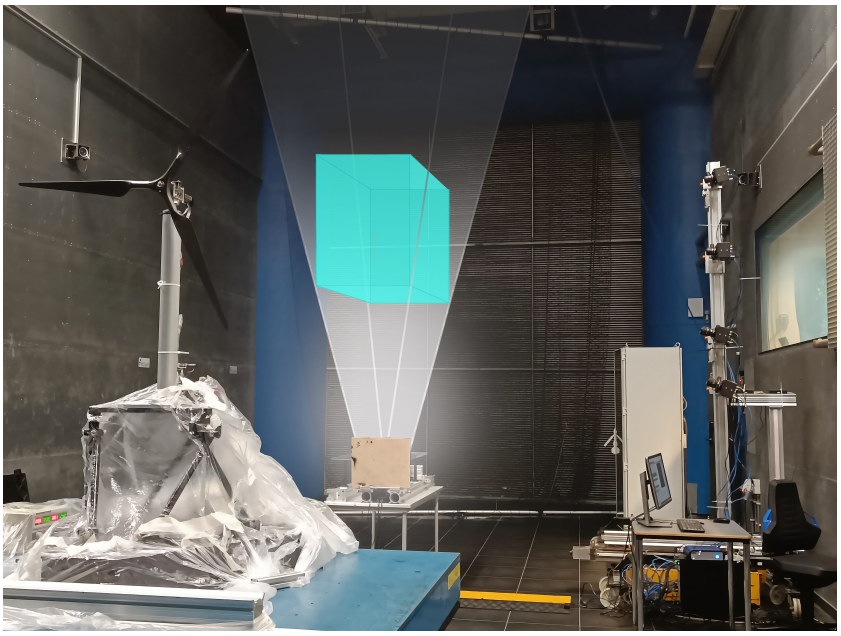

Figure 3.10: Volume illuminated by LEDs and captured by High Speed Cameras.

To obtain a 1m × 1m window in the lateral view, the camera placements need to be adjusted. Using the Thin Lens Equation the distance to the center of the volume can be calculated:

$$\frac{1}{f} = \frac{1}{d_i} + \frac{1}{d_o} \tag{3.1}$$

Where d_o is the distance from the camera lens to the plane of interest (which we need to determine), d_i is the distance from the camera lens to the sensor, and f represents the lens (focal length), which is known.

Considering the ratio between sensor size (h =pixel size x resolution of sensor) and object size (H = desired FOV), known as Magnification Factor (M),

$$M = \frac{h}{H} = \frac{d_i}{d_o} \tag{3.2}$$

and combining Equations 3.1 and 3.2:

$$d_o = \frac{f(1+M)}{M} \tag{3.3}$$

With this derived equation, the distance from the cameras to the center of the volume is no longer unknown. However, it is important to consider that, due to availability, two different lenses are being used: 50mm and 60mm. This difference is very relevant when determining camera placement. For a 50mm focal length, a distance of 1.74m is sufficient to capture the entire FOV. However, when using a 60mm focal length, a distance of 2.99m from the camera sensor to the center of the volume is required. This latter distance was chosen for the experiment to ensure that both lenses could capture the desired FOV. A visualization of the available FOV for each camera is shown in Figure 3.11, where the two bottom cameras are equipped with 60mm lenses, and the top two cameras use the wider 50mm lenses.

It is also important to note that all cameras are positioned at an angle, meaning the tangential distance is longer than the previously calculated 2.99m. While the required distance could have been precisely calculated, it was instead decided to manually adjust the distances during the experiment setup to ensure that the minimum FOV of 1m was achieved for all cameras.

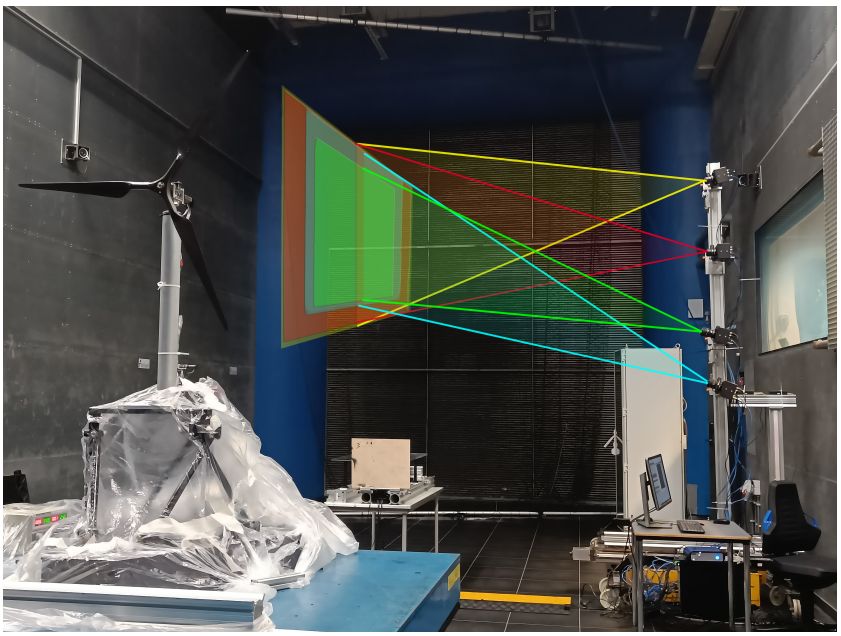

Figure 3.11: 3D PTV Camera Setup: Blue and Green cameras make use of 60mm lenses, Red and Yellow cameras make use of wider 50mm lenses.

These camera angles are necessary to ensure high-quality post-processing of the image sets. While mounting all cameras on a single vertical beam offers advantages in terms of simplicity and structural integrity, experienced experimental researchers from the TU Delft Faculty of Aerospace Engineering recommended maintaining a total angle difference of 40°. Based on this, the cameras were assigned angles of $[15, 0, -15, -25]$ from top to bottom. The second camera from the top (highlighted in red in Figure 3.11) was first placed at the same height as the center of the volume (2.745m from the ground, corresponding to 1.21m from the base of the turbine), and the other cameras were positioned accordingly.

The streamwise length and vertical height of the volume have been determined. The final variable to specify is the lateral component of the volume. Unlike the other dimensions, the width is not dependent on the camera positions but rather on the lens settings and is constrained by the illuminated region containing bubbles. Each lens allows for aperture adjustments, which control the amount of light reaching the sensor. A higher aperture results in a narrower depth of field (the region in focus), while a lower aperture increases the depth of field. The aperture is defined by the f-stop parameter ($f_\#$), and the desired one can be found with the following formula:

$$f_\# = \sqrt{\frac{\delta_z}{4.88\lambda(\frac{M+1}{M})^2}} \tag{3.4}$$

Where M is the previously introduced Magnification Factor, λ is the speed of light, and δ_z is the depth of field. Generally speaking, a greater depth of field is preferable, as it allows for more data acquisition within the same measurement, potentially leading to deeper insights. However, in this experiment, we are constrained by the dimensions of the seeder. The maximum width of the seeded region is 0.6m, but this width will vary significantly as the bubbles dissipate due to turbulence introduced by the wind turbine. Therefore, extending the depth of field beyond 0.6m holds no practical significance.

Using the formula, an f-stop of 9 is obtained as the theoretical result. However, f-stop values on camera lenses are preselected and follow a sequence where each step represents a halving of light intensity, progressing in factors of the square root of two. The available f-stop values closest to 9 are 8 and 11. If f/8 were selected, the resulting depth of field would be 0.38m, which is insufficient. Therefore, f/11 is the correct choice, providing a depth of field of 0.72m, allowing for a safety margin.

Camera	Focal length f	Camera height	Camera angle	Distance d_o	F-stop $f_\#$
Camera 1	50mm	3.52m	15º	2.99m	11
Camera 2	50mm	2.75m	0º		
Camera 3	60mm	1.97m	-15º		
Camera 4	60mm	1.48m	-25º		

Table 3.2: Summary of the four camera setups used in the experiment, detailing their location, orientation, and lens settings.

The final influencing parameter to consider is the volume illuminated by the LEDs, as particles outside this illuminated region will not be detected during post-processing. The LEDs were positioned below the volume at a height of approximately 1.3m, arranged in a line with a spacing of around 0.2m between them. Due to the emitted light angle, which ranged between 5° and 10°, the illumination in the streamwise direction was sufficient to cover 1m. However, in terms of width, the theoretical maximum illuminated region in the Y direction was approximately 0.45m. This was confirmed during the experiments, where the illuminated width ranged between 0.45m and 0.5m. This dimension is of lesser importance to the study, thus setup was considered acceptable as it was.

Therefore the theoretical final volume is 1m x 1m x 0.45m, giving a total of $0.45m^3$ (final volume ended up being smaller due to HFSB limitations: discussed in section 3.3).

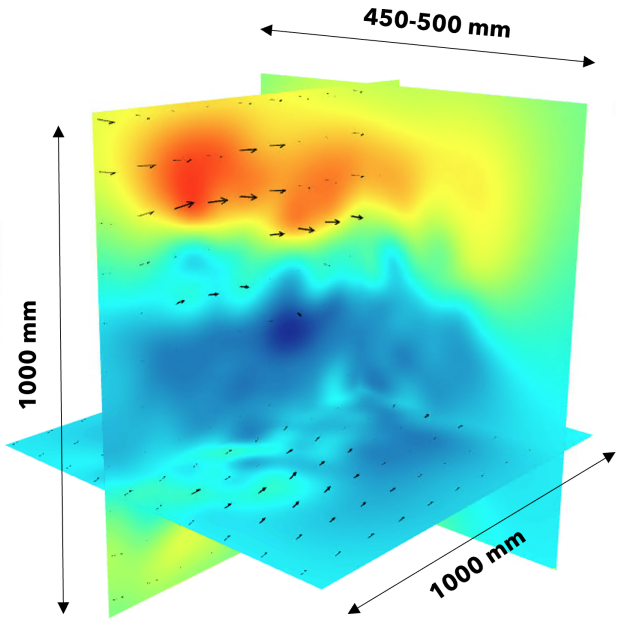

Figure 3.12: Maximum theoretical measurement volume of the 3D PTV setup, featuring a larger extent in the streamwise and vertical directions, and a thinner spanwise thickness.

3.2. 3D PTV Measurements

3.2.1. Acquisition procedure

Before acquiring images, the entire system must be calibrated for each volume. This involves manually adjusting the cameras to align with the center of the volume and ensuring proper focus so that the particles are clearly visible. Thanks to the traversing system, multiple volumes can be recorded using the same calibration, as the small movement of the platform will not affect the focus or . Only when the traversing system as a whole

Calibration can be performed automatically using a calibration plate positioned at the center of the volume. With LaVision's DaVis software, image sets with the calibration plate in the frame are captured and subsequently a coordinate system is established, setting the global zero at the plate's center.

In addition to plate calibration, Volume Self-Calibration (VSC) is highly beneficial for 3D PTV. Achieving sub-pixel calibration accuracy across the entire volume is relevant, as calibration errors can lead to reconstruction inaccuracies [70]. The disparity map represents the pixel-wise difference in particle positions as observed from different camera perspectives. It is a key element of stereo vision, enabling the reconstruction of 3D particle positions through triangulation. Disparity maps from multiple recordings are summed for better statistics, and by monitoring the uniformity in particle positions across the grid a good calibration is obtained (see Figure 3.14).

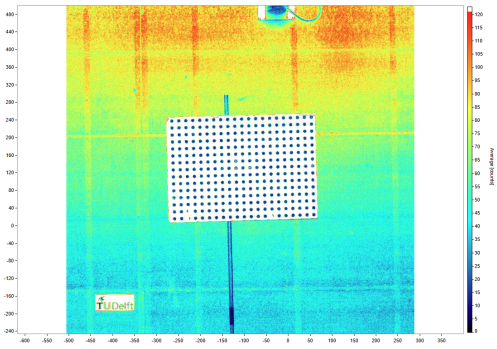

Figure 3.13: Calibration plate as seen from DaVis. Coloring corresponding to pixel intensity.

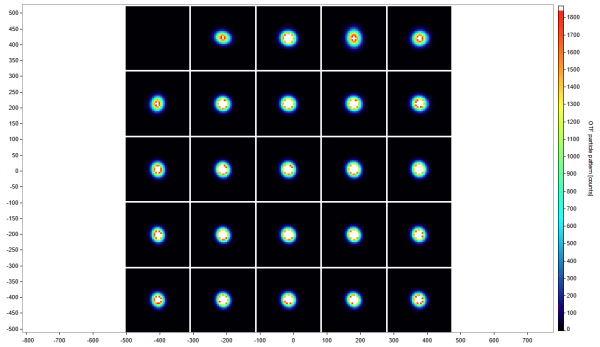

Figure 3.14: Disparity map resulting from VSC. All sectors exhibit signal clustering with minimal deviation, as indicated by the grouping of data points into compact circular regions.

When the system is calibrated and ready to be used the following procedure was followed:

1. Set cameras and LEDs to standby mode in DaVis, awaiting a trigger action.
2. Start the wind turbine rotor (only after ensuring the wind tunnel is secured and safe for operation).
3. Activate the HFSB seeder.
4. Load and activate the imposed motions in the hexapod.
5. Begin recording, either manually or automatically triggered.
6. End recording; the image set is automatically stored on the acquisition PC.
7. Shut down the HFSB system, wind turbine rotor, and hexapod.

Each recording lasts 10 seconds in total, with cameras operating at a frame rate of $410\mathrm{Hz}$. This frame rate is determined based on the requirement that the particle displacement should be approximately 10 pixels per frame. Given that the field of view is 1024 pixels corresponding to $1\mathrm{m}$, the flow velocity is $4\mathrm{m/s}$. The displacement per frame can be calculated as:

$$\Delta x = \frac{10}{1024} \times 1000 \text{ mm} = 9.77 \text{ mm} \tag{3.5}$$

To determine the required frame interval (Δt) for a 10-pixel displacement, we use the relationship:

$$\Delta t = \frac{\Delta x}{U} = \frac{9.77 \text{ mm}}{4000 \text{ mm/s}} = 2.44 \text{ ms} \tag{3.6}$$

Thus, to achieve the desired 10 pixel displacement per frame, a time interval of $\Delta t = 2.44ms$ is required, corresponding to approximately 410Hz. This confirms that the chosen frame rate of 400Hz is sufficiently accurate for the intended measurement.

3.2.2. Post-Processing

Each dataset for every test case consists of four combined sets of 4000 images, all of which require post-processing. All steps are performed inside DaVis platform. The first step involves applying a subtract minimum filter to the raw images to eliminate unwanted background light.

Next, the Shake-The-Box (STB) algorithm is employed to reconstruct particle trajectories from high-density data. This algorithm is based on the Lagrangian Particle Tracking (LPT) principle, by tracking the particle positions from the previous timestep, the particle can be identified in the current timestep, and the position ”shaken” such that the all cameras place it in the same coordinates [71]. By adjusting the threshold for 2D particle detection in DaVis, each different case is reconstructed based on the number of particles and overall light intensity. For some cases where the quality of the first iteration of STB does not deliver the desired quality, a second iteration can be included by selecting the multi-pass option. This option allows for optimized tracking for each area in the flow by setting individual velocity limits for each pass [72].

Before proceeding to the next step, overlapping particles in adjacent volumes are merged where appropriate. This is particularly relevant for the first three measurement volumes, which each share an overlap of 0.125m. In DaVis, the merging is performed by combining the volumes into a single file, allowing them to be post-processed together from this point onward. The overlapping regions ensure continuity in the reconstructed flow field, enabling continuous spatial data visualization without gaps or missing information.

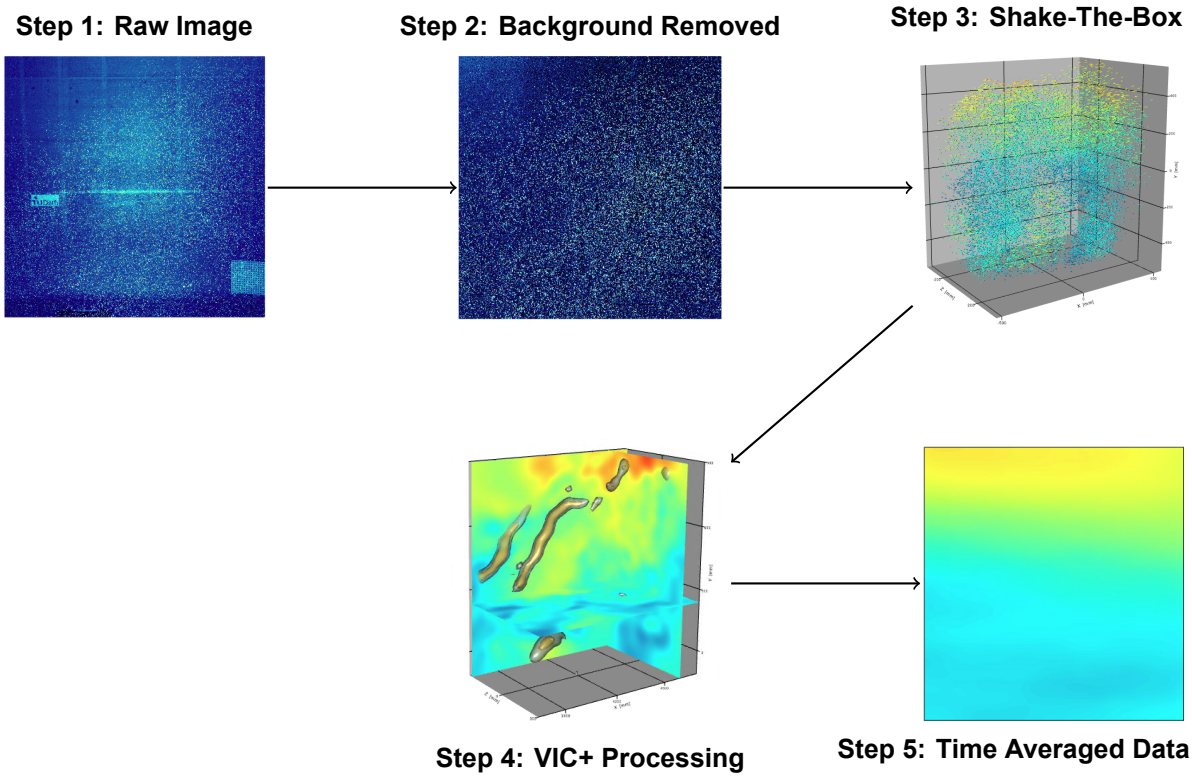

Figure 3.15: Step-by-Step Processing Workflow.

To obtain instantaneous velocity fields, the Vortex-In-Cell Plus (VIC+) method is applied. This technique integrates particle tracks with the vorticity transport equation, leading to higher spatial resolution and improved accuracy compared to conventional methods. To convert the volume into a vector field, a grid spacing that makes truncation errors negligible is needed. A ratio relating particle concentration (C) to the grid node spacing (h) is given by [73]:

$$h = \frac{1}{4} C^{-1/3} \tag{3.7}$$

While the particle concentration in the recordings changes from recording to recording, most of the volumes show a C of around 2×10^{-6} particles-per-voxel (ppv), corresponding to a window size of 20 voxels. VIC+ results can then be quickly checked for coherence using the visualization parameter "swirling strength" [74]. It is a convenient vortex visualization parameter in which flow convection, with little noise, should be seen as a result of good processing (swirling structures seen in Figure 3.15, "Step 4").

Once the flow field is resolved, an averaging operation can be quickly performed directly within DaVis. To finalize the procedure, the processed data can be exported for further analysis using customized scripts.

VIC+ vs Binning

In the previous experimental campaign performed one year prior to this thesis, "Binning" was used as the post-processing technique to convert particles into a vector field. However, experimental experts from the faculty of Aerospace Engineering suggested that VIC+ should be used. In this brief section, an analysis is carried on which method is more suited for a large rotor 3D PTV experiment.

Binning approach is rather simple. A cell size is selected, and a cartesian grid is created by spatially averaging over the small cubic volumes. The simplicity comes with the advantage of smaller computational cost when compared to VIC+.

The VIC+ is an improvement of the VIC method initially created in 2014 [75]. The authors created came up with the technique when higher temporal resolution of tomographic PIV experiments was needed. The introduction of physical laws (Navier-Stokes and vorticity transport equation) demonstrated the wide use of this novel method.

Currently, VIC+ considers the velocity material derivative of the sparse tracer particles, takes into account the continuity equation, presents a novel multigrid solver, and is able to reconstruct a flow field without any initial condition given [73, 76]. These advancements allow for more accurate determination of turbulent structures, with a fraction of the seeding concentration needed for other reconstruction methods. In addition, although not relevant to this study, VIC+ is able to work out greatly the boundary layer, with great spatial resolution and excellent vorticity and dissipation statistics [77]

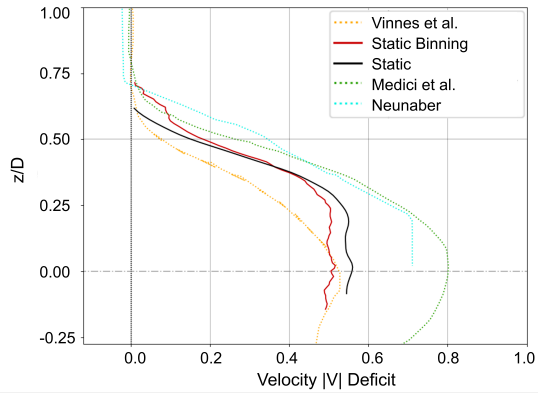

Figure 3.16: Velocity deficit $(U_\infty - |V|)/U_\infty$ comparison of VIC+ and binning methods to literature studies at a distance of 3D from the rotor plane.

Reference	Rotor D	No. blades	TSR
Medici et al. [78]	180 mm	2	3.66
Neunaber [79]	578 mm	3	6.2
Vinnes et al. [28]	200 mm	3	3.65
This study	1200 mm	3	7.5

Table 3.3: Rotor parameters from referenced studies.

The average velocity deficit when using binning method vs VIC+ method is showed in Figure 3.16, these are the curves for the static case. Additionally examples from literature where wind turbines in an experimental setup are tested are also included in dotted lines.

VIC+ shows a more smooth gradient along the vertical domain than binning. This is explained as binning creates a grid out of the volume to make the vector field and calculate the average, but if there is information in a cell for a specific time step, the cell is not considered for the average. Since VIC+ creates values from previous iterations to fill all cells, the average is taken over the 4000 images that each recording is comprised of. In other words, VIC+ will always converge faster over the same amount of samples.

On the other hand, binning achieves similar results in just a fraction of computing time. They both transition from wake to free-flow following the same trend as what it has been seen in literature. However, binning fails to predict the velocity deficit when looking at the flow right in the middle of the wake. The results fluctuate a bit in this region and they deviate around 10% from VIC+ values. Since VIC+ is a physical model and more average points have been considered, it can be trusted more. Thus binning is judged as limited in this region of the wake.

Because of this, the recommendation from TU Delft experts, and even then suggestion from LaVision software to achieve an ”unsurpassed grid resolution” [80], VIC+ is the main post-processing method used in this report.

3.2.3. Text Matrix

A simplified version of the test matrix utilized for 3D PTV experiments is shown, a more detailed view can be found in Appendix A. Here, repetition of test cases for different locations downstream are avoided.

The initially planned test matrix stopped at run 34, but due to extra time in the wind tunnel, more cases were added for completion and an attempt to improve wake characterization. Please note the distinction in amplitude of the test cases from run 35 to run 38: these are not a repetition of the previously tested 3.5D volume, but a extension of the test by including different amplitudes corresponding to a different normalized velocity variation ($\Delta V^* = 0.05$).

The core of the experimental campaign focuses on studying surge and pitch motions at frequencies of 2Hz and 5Hz, corresponding to low and high reduced frequencies ($f_r = 0.6$ and $f_r = 1.5$, respectively). These values are representative of realistic offshore conditions. Specifically, a study of a full-scale surging 10 MW FOWT demonstrated that reduced frequencies of 0.6 and 1.5 at rated wind speeds correspond to resonant platform responses and wave-induced excitation, respectively [33]. These reduced frequencies translate to full-scale oscillation frequencies of approximately 0.03Hz and 0.09Hz, reinforcing the real-world relevance of the experimental conditions. Pitch motion is also investigated, as it is, along with surge, one of the dominant and most influential motions experienced by FOWTs.

Table 3.4: Summary of Test Matrix.

Run #	Case	Frequency [Hz]	Amplitude	Rotor speed [rpm]	X Location [Diameter]
1	Flow	n.a.	n.a.	0	1D
2	Static	n.a.	n.a.	480	1D
3	Surge	2	31.8 mm	480	1D
4	Surge	5	12.7 mm	480	1D
5	Pitch	2	1.57 deg	480	1D
6	Pitch	5	0.63 deg	480	1D
7	Surge	2	31.8 mm	480	1.625D
...	...	...	...	...	...
14	Flow	n.a.	n.a.	0	1.625D
15	Flow	n.a.	n.a.	0	2.25D
...	...	...	...	...	...
20	Pitch	5	0.63 deg	480	2.25D

Run #	Case	Frequency [Hz]	Amplitude	Rotor speed [rpm]	X Location [Diameter]
21	Surge	2	31.8 mm	480	3.5D
...	...	...	...	...	...
28	Flow	n.a.	n.a.	0	3.5D
29	Flow	n.a.	n.a.	0	4.75D
...	...	...	...	...	...
34	Pitch	5	0.63 deg	480	4.75D
35	Surge	2	*15,9 mm*	480	*3.5D*
36	Surge	5	*6,4 mm*	480	*3.5D*
37	Pitch	2	*0,79 deg*	480	*3.5D*
38	Pitch	5	*0,32 deg*	480	*3.5D*
39	*Wave1*	n.a.	n.a.	*408*	*3.5D*
40	*Wave2*	n.a.	n.a.	*474*	*3.5D*
41	*Wave3*	n.a.	n.a.	*474*	*3.5D*
42	Static	n.a.	n.a.	480	5.375D
43	Surge	2	31.8 mm	480	5.375D
44	Surge	5	12.7 mm	480	5.375D
45	Pitch	2	1.57 deg	480	5.375D
46	Pitch	5	0.63 deg	480	5.375D
47	Flow	n.a.	n.a.	0	5.375D

3.3. Limitations

The presented setup has some limitations which, while not all might affect the results, it is necessary to state them:

- **Wind Turbine Placement:** Due to safety concerns, the hexapod and wind turbine model were placed $3.1\mathrm{m}$ behind the exit of the nozzle. The test section of the wind tunnel has a shear layer on each side opening up with an angle of $9.5\mathrm{deg}$, and additionally the turbulence increases with distance as it was characterized in [31]. While higher turbulence intensity might be irrelevant since the wind turbine model will be the main source of turbulence, the expansion and interactions close to the shear layer will affect the last volumes of interest which are relevant for studying wake recovery.
- **Heat Exchanger Blockage:** The final measurement volumes are positioned near the end of the test section, where a heat exchanger is located. This component acts as a physical obstruction, partially impeding the flow. Although the extent of the blockage cannot be measured, its influence could be considered visible in Figure 3.17, where a flow deceleration begins. As a result, the validity of the data acquired in the final volume may be compromised.
- **HFSB Seeder**: The seeder is comprised of a bundle of small nozzles that blow fluid and create the bubbles. During the experiments, it was noticed that some of the nozzles did not shed bubbles, this could have happen due to external blockage at the exit or bad internal fluid distribution. In the measurements without wind turbine, some gaps can be seen in the locations of the faulty nozzles. While, this does not affect much the measurements with turbine, as the induced turbulence mixes the bubbles all over the domain, it does contribute to having variating seeding densities from one case to another.
- **Negative Velocity v**: From the flow study without a wind turbine (Figure 3.17), a negative velocity is observed. It goes down constantly at around $0.17\mathrm{m/s}$ and it is observed for the entire domain. This phenomena could be caused by the bubbles not being completely neutrally buoyant, due to them being bigger and heavier, or due to the wind tunnel flow interacting with the non-moving air below the test section and creating oscillations that pull air from the area of interest. While this effect is clearly visible for the flow visualization, it cannot be instinctively noticed when looking at cases where the wind turbine is present. The effect in our data of interest cannot be fully quantified.

- **Low HFSB Density at Top of Volume**: For most measurements a lack of bubbles was seen, at some point during the measuring time, for the last $0.1\text{m} - 0.2\text{m}$ in height. As mentioned previously, the desired volume is 1m in height, and it is limited by the physical location of the seeder. When the turbine is present, oscillations can cause the flow above the volume without HFSBs to enter the measured region. This affects the validity of data in the top region of the volume. Thus the available data is cropped to avoid these regions, reducing the maximum size of the volume from 0.45m^3 to 0.38m^3 (reduction in height from 1m to 0.85m).
- **Height Misalignment**: When merging volumes together, a height difference was observed between most of them. After careful investigation the cause of it was believed to be the tilting of cameras due to gravity and loose clamping on the structure. To present the data in this report, the affected volumes were manually altered and moved to a z location that made physical sense.

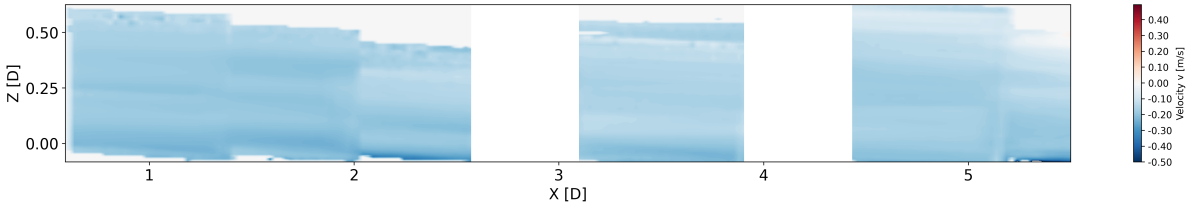

Figure 3.17: Flow average vertical velocity $\bar{v}$ in OJF's test section (no wind turbine model present).

In conclusion, due to limitations: the last volume will be ignored for flow analysis, and all volume sizes have been shrunk down by the reduction of height. However, it is also important to mention that, in spite of the limitations, the measured data shows great matching between volumes, which is remarkable considering that each volume was measured in different days and with different system calibrations.

4

Results

In this chapter, the data after post-processing will be analyzed. Detailed examinations of the velocity field and turbulence intensity for unconditionally averaged and phase-locked averaged flows are presented. Special attention is given to comparisons between different motion types, frequencies, and amplitudes, additionally studying the influence of wave-induced motion. To support these comparisons, line plots depicting velocity deficit and wake recovery are given. Tip vortices are also briefly analyzed and compared across various cases. Furthermore, energy spectra is evaluated to highlight the most significant flow conditions. The chapter concludes with an assessment of experimental uncertainties to evaluate the reliability of the results.

As previously presented, the last recorded volume will be ignored due to data suspicious of being affected by blockage from the porous wall at the end of the wind tunnel. Thus, the displayed data will be available from 0.6D to 2.6D, then from 3.1D to 3.9D, and finally from 4.4D to 5D. The position of each individual volume was manually modified to ensure proper fit with the neighboring volumes after some vertical misalignment was spotted after the experiment. Each measured volume's final dimensions are 1m x 0.45m x 0.85m giving a volume of $0.38\mathrm{m}^3$ and a combined volume of around $1.6\mathrm{m}^3$. Unless specified differently, all show data will be considered at the center plane of the wake where $y = 0$.

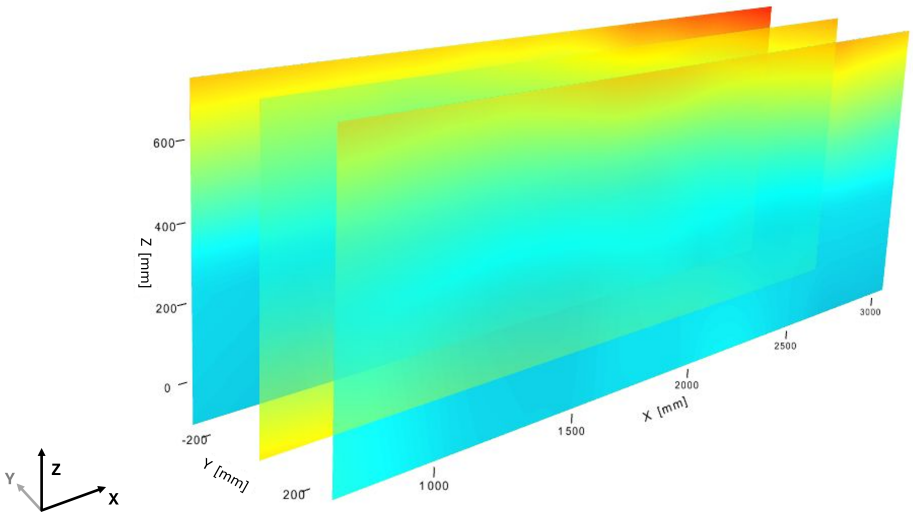

Figure 4.1: Post-processed and merged flow field for the first three measured volumes. Planes at displayed at $y = -0.22\mathrm{m}, y = 0\mathrm{m}, y = 0.22\mathrm{m}$.

4.1. Convergence Analysis

The study of the wake characteristics and the difference between platform motions requires of having a converged statistical dataset. To ensure that, a convergence study is carried out by analyzing velocity components for a large amount of samples in a wake location prone to instabilities (near the wake boundary).

Convergence study for static case is shown in Figure 4.2. Convergence is obtained for the three velocity components after around 500 samples. This ensures that when the entire set of 4000 images is used, convergence is well obtained. Additionally, a study is performed for a motion case, for example: Pitch $2\mathrm{Hz}$ (Figure 4.3). The motion of the platform is clearly visible in the line for Velocity u and Velocity w, showing a little peak every 200 samples. After 1000 samples the oscillations in the average become indistinguishable.

Since a phase-locked motion study is also within the aim of this thesis, a convergence study is presented applying phase-locking for $2\mathrm{Hz}$, which is the most critical frequency only offering 20 sample points ($2\mathrm{Hz}$ for 10s). In Figure 4.4 convergence is observed to occur around 15 samples. This is considerably lower than the previous plots, but it is expected as the aim of phase-locking is to obtain a representation of the same flow conditions, ignoring variations.

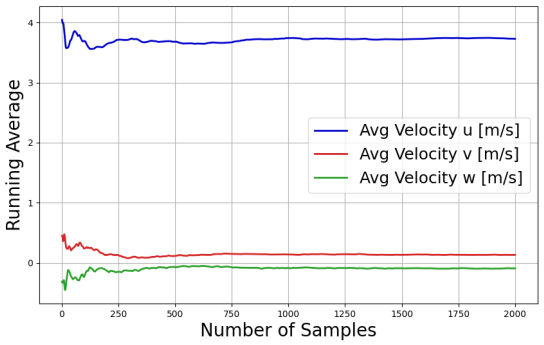

Figure 4.2: Convergence of velocity components, *u,v,w*. Values displayed for 2000 images.

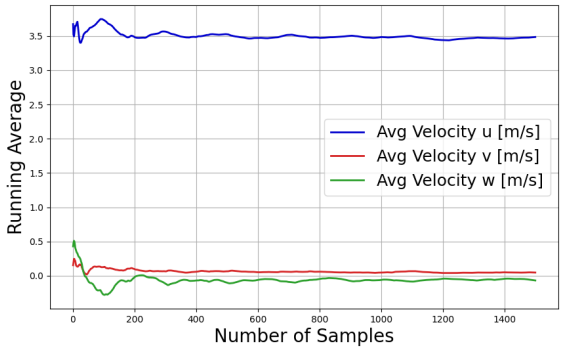

Figure 4.3: Convergence of velocity components, *u,v,w*, for a motion case (Pitch $2\mathrm{Hz}$). Values displayed for 1500 images.

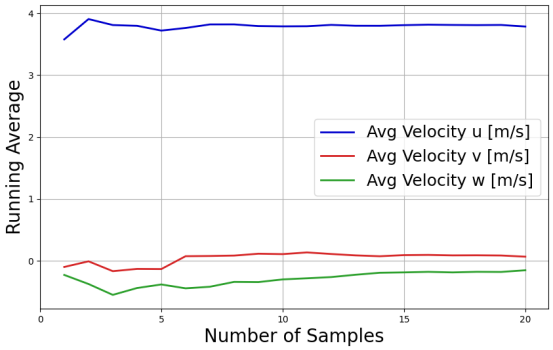

Figure 4.4: Convergence of phase-locked velocity components, $\langle u \rangle, \langle v \rangle, \langle w \rangle$, for low-frequency motion case (Pitch $2\mathrm{Hz}$). Values displayed for 20 images.

4.2. Time Averaged Wake Analysis

In this section, time averaged data is presented. The measurements are unconditionally averaged with the aim to study the characteristics of the wake. Special attention will be given to the behavior of velocity components, turbulence intensity, and the recovery and development of the wake as it progresses downstream. In addition, tests involving smaller motion amplitudes and realistic wave scenarios are conducted exclusively at one measurement location.

4.2.1. Velocity Components

This subsection presents the three velocity components of the flow: u (streamwise, x-direction), v (lateral, y-direction), and w (vertical, z-direction). Analyzing these components provides a detailed way of characterizing and quantifying the wake.

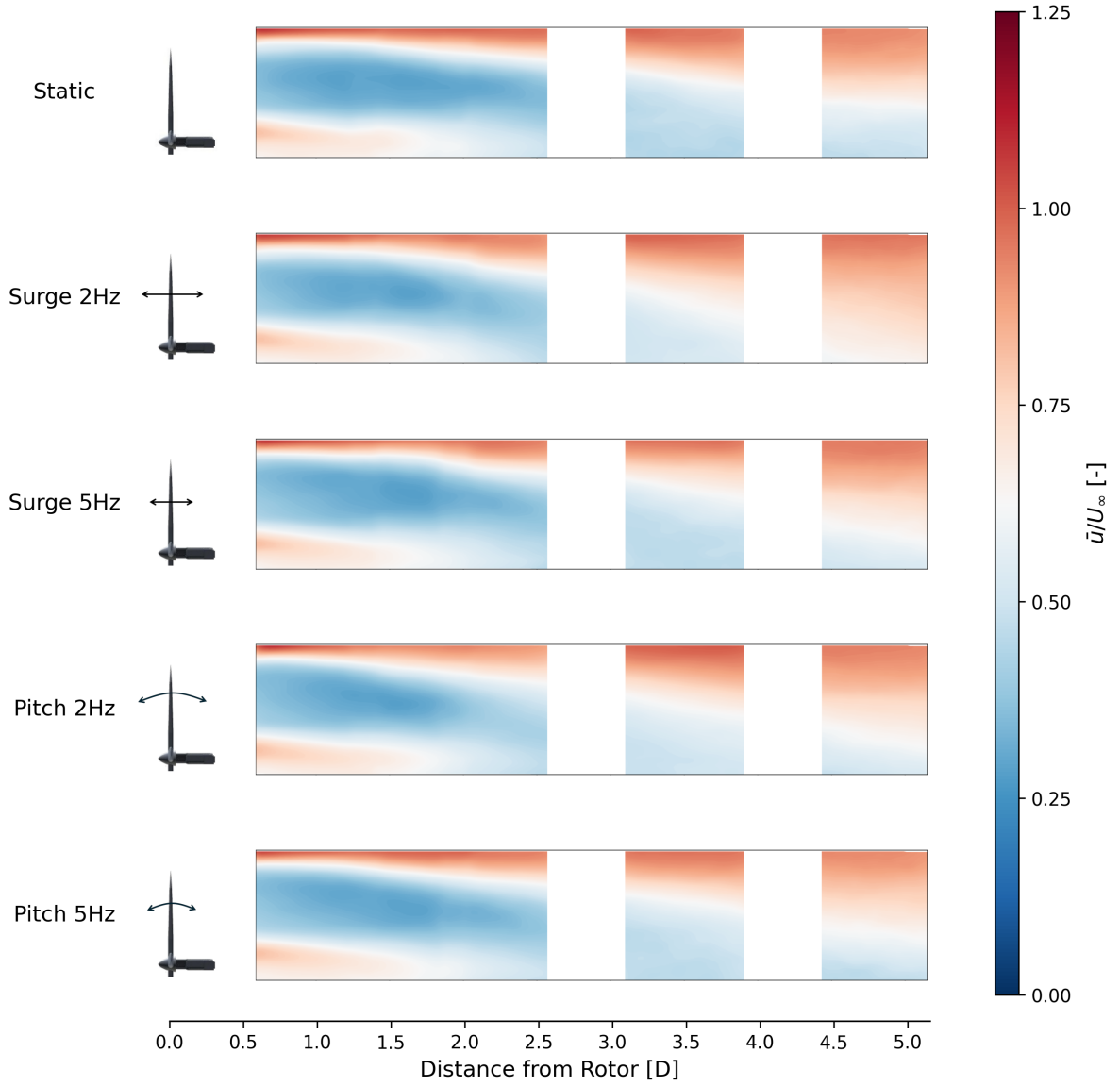

Figure 4.5: Average streamwise velocity component normalized by freestream velocity $\bar{u}/U_\infty$ for static and motion cases.

At first glance the flow field when considering *Velocity u* (Figure 4.5) does not seem to variate much when comparing cases with different motions. All cases present similar characteristics to the static wind turbine, specially when observing the closest measured locations. Wake is noticed to expand around 20% after the rotor for all cases, matching other studies [31, 28, 78, 79], and as it progresses downstream the shear layer with freestream enlarges and shifts towards the center of the rotor.

The region with the lowest airspeed is located right behind the blades of the wind turbine model with an airfoil profile, depicting the energy extraction process. The flow in this region is as low as $1.5m/s$ up to 2.5D. It is important to remember that each blade's profile for the turbine model begins at around $r/R = 0.18$ from the center-point of the nacelle and rotor assembly, and that below that, only a non-aerodynamic circular geometry exists. This is the reason why around the nacelle a red colored zone is observed, no energy is extracted from the flow there and thus the velocity is higher.

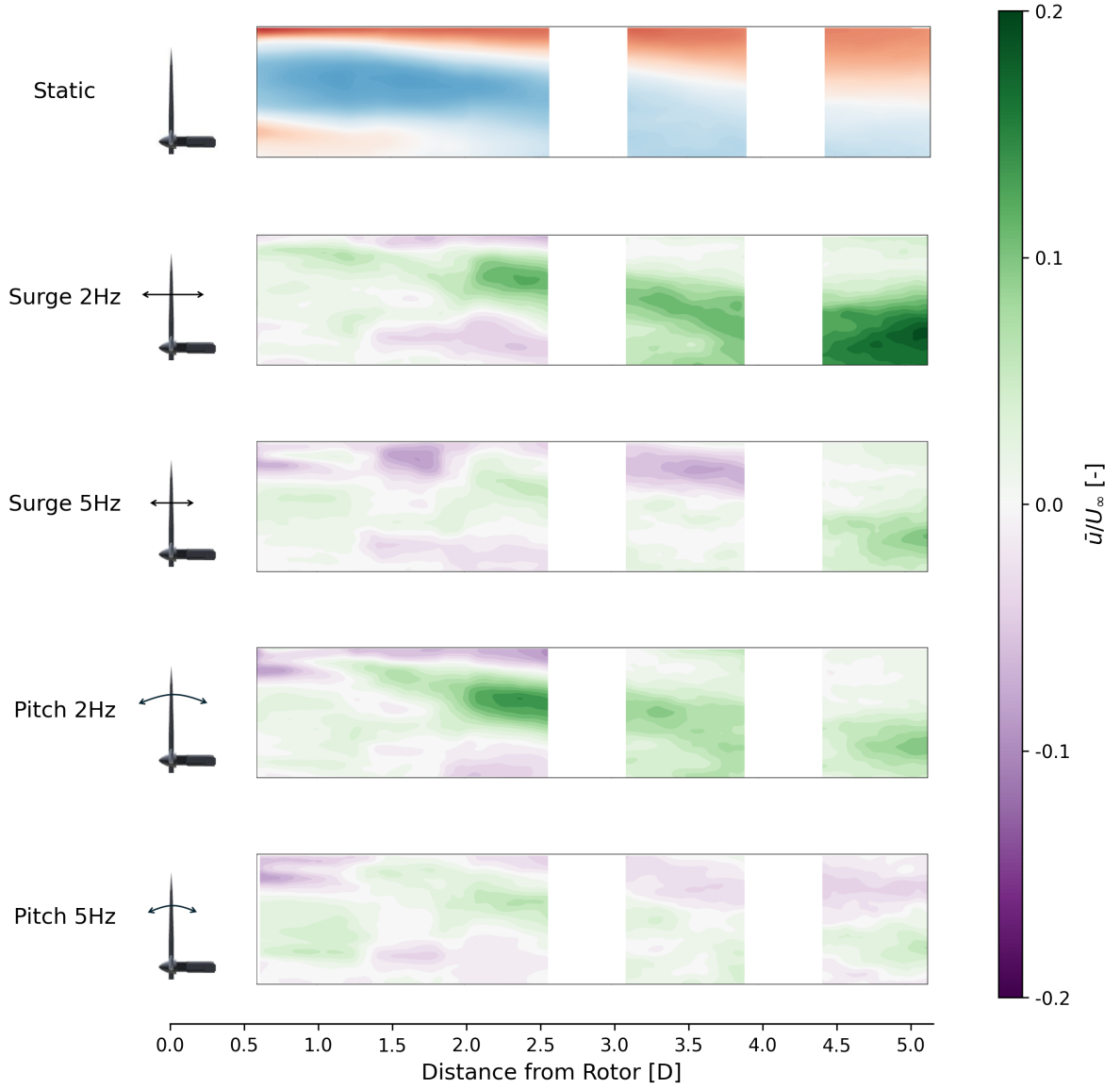

Figure 4.6: Average streamwise velocity component difference between static and motion cases normalized by freestream velocity $(\bar{u}_{motion} - \bar{u}_{static})/U_\infty$. Average normalized velocity $\bar{u}/U_\infty$ for static (top image) plotted for reference.

By computing the difference in normalized velocity with respect to the static case ($(\bar{u}_{motion} - \bar{u}_{static})/U_\infty$), more revealing and quantifiable information can be obtained (Figure 4.6).

It is now more evident that Surge 2Hz is the motion with biggest influence in the wake. With a higher velocity in most of the domain, but specially in the last volume where the motion increases the speed $0.5m/s$, it suggests a quicker wake recovery in the far wake.

Other cases also seem promising for the far wake, where improvements of $0.2 - 0.3m/s$ are seen. Only Pitch 5Hz gives unclear information of the trend of the wake behavior for distances beyond 5D.

The purple zones where a slower velocity is observed, compared to the static case, are mainly present on the upper and lower boundaries of the domain. This physically makes sense: the motions of the FOWT model induce mixing in the wake, which for the upper boundary means that the freestream velocity is mixed with slow moving air from the wake, and for the lower boundary the pocket of fast flow surrounding the nacelle is mixed with both the wake of the rotor and also the wake of the wind turbine tower.

This same mixing behavior can be used to explain the region of faster streamwise flow behind the blades of the wind turbine model. The originally slow flow is now being mixed further with the freestream flow and the flow around the nacelle due to the floating motions.

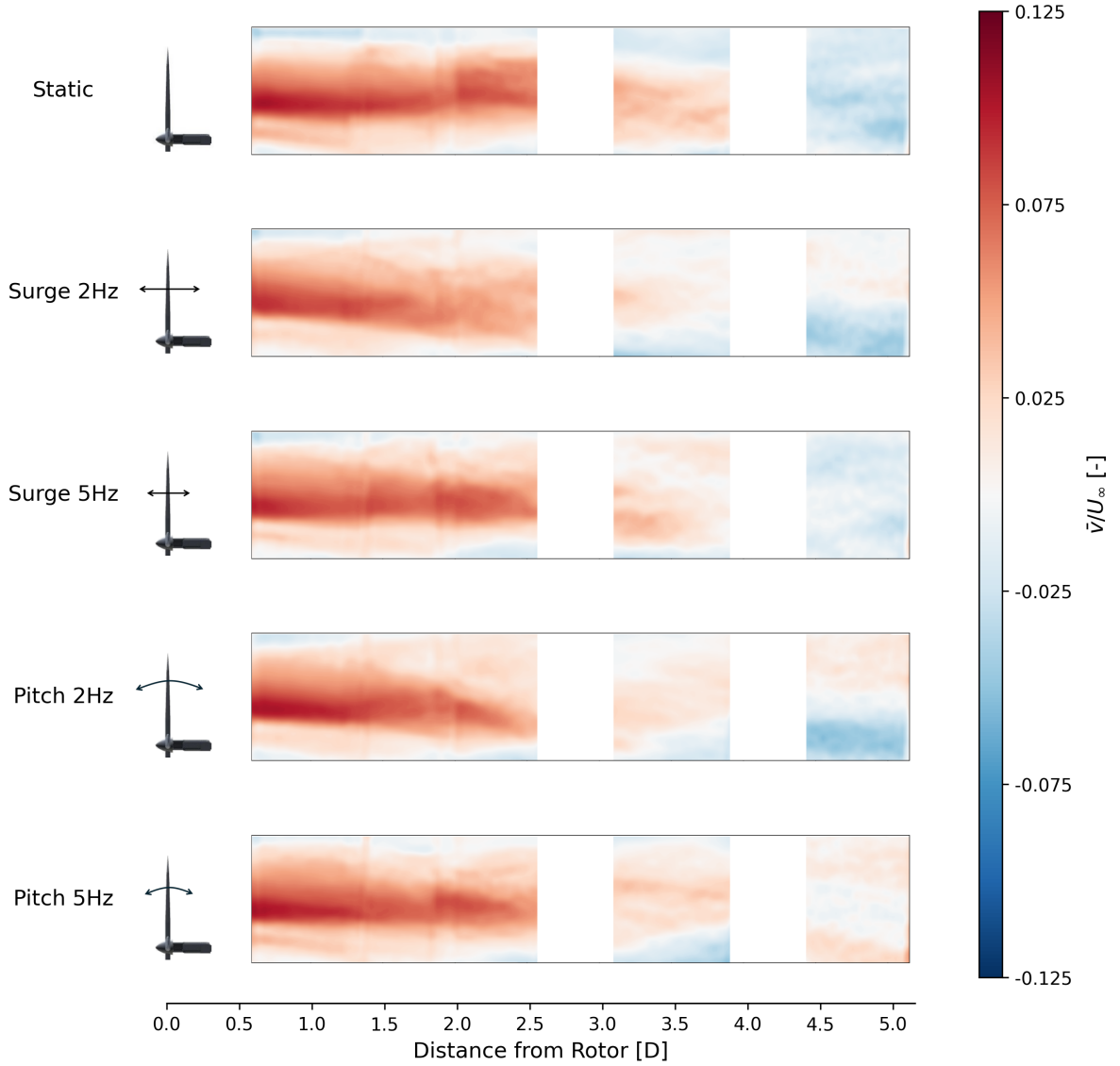

Figure 4.7: Average spanwise velocity component normalized by freestream velocity $\bar{v}/U_\infty$ for static and motion cases.

The flow in spanwise direction, *Velocity v*, is presented in Figure 4.7. The red regions with positive velocity are due to the conservation of momentum due to the rotation of the rotor: The clockwise rotating blades induce an anti-clockwise whirling flow in the near wake. The effect slowly dissipates until the rotor effects are no longer visible somewhere around 4D. Thus, at this location, the wake can no longer be considered to be in near wake state (similar location to [23] and [52]).

As the wake looses the positive spanwise velocity, it ends up with around $0.1m/s$ of negative velocity for the last volume. Especially for Static and Surge $5\mathrm{Hz}$, where the effect is seen in the entire volume, and concentrated in the lower half of the volume for the low frequency pitch and surge.

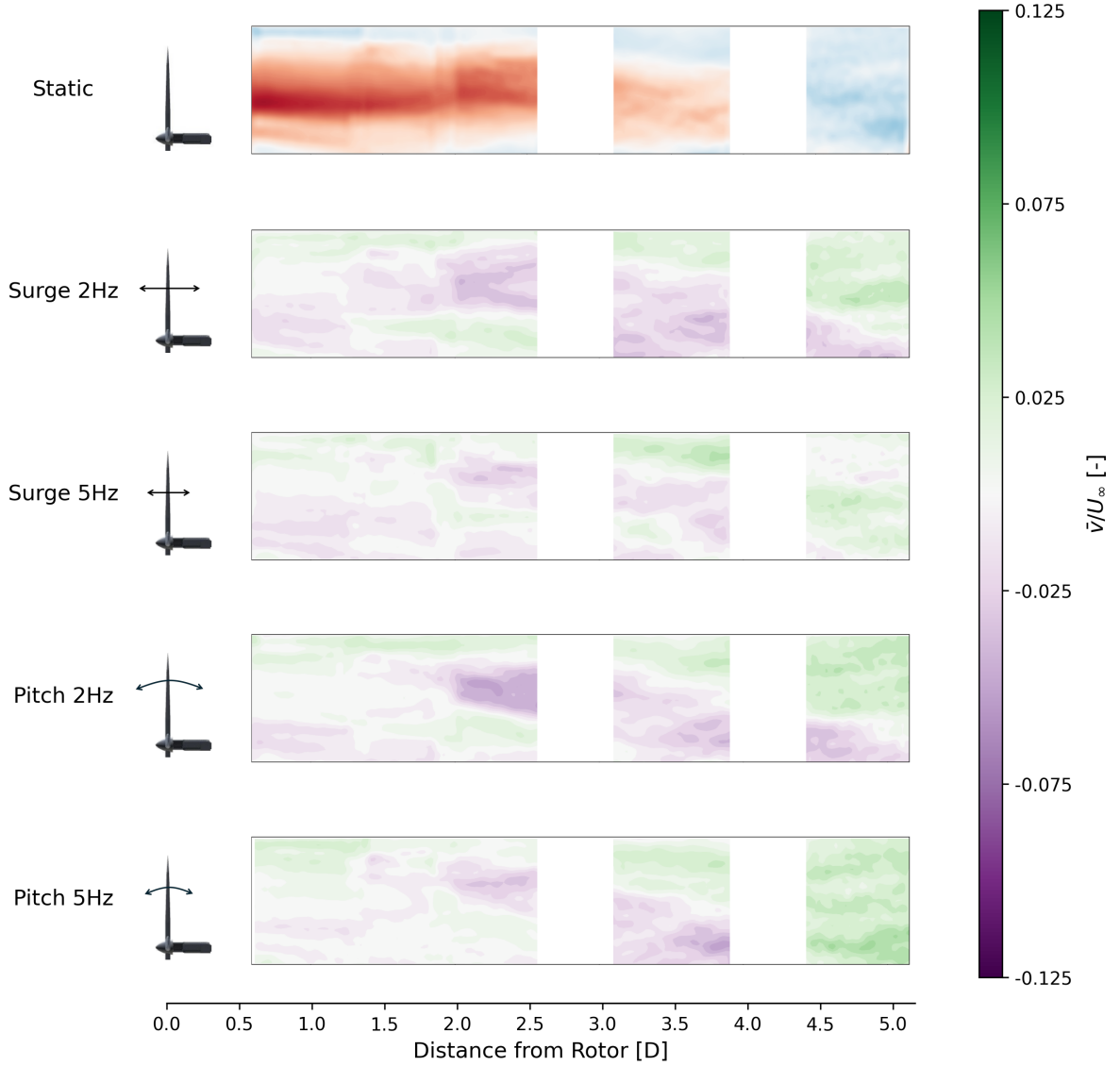

Figure 4.8: Average spanwise velocity component difference between static and motion cases normalized by freestream velocity $(\bar{v}_{motion} - \bar{v}_{static})/U_\infty$. Average normalized velocity $\bar{v}/U_\infty$ for static (top image) plotted for reference.

Using the difference in velocity plots, a similar pattern can be seen for all cases (Figure 4.8): less velocity in the center of the wake, and on the other hand, more positive lateral velocity following the shear layer with the freestream and expanding until covering the entire domain in the last volume, which essentially dampens the negative spanwise velocity seen in the static case.

Like with streamwise velocity, the additional mixing of the wake, compared to the static case, is smoothing out the regions in the near wake and reducing the maximum and minimum value peaks.

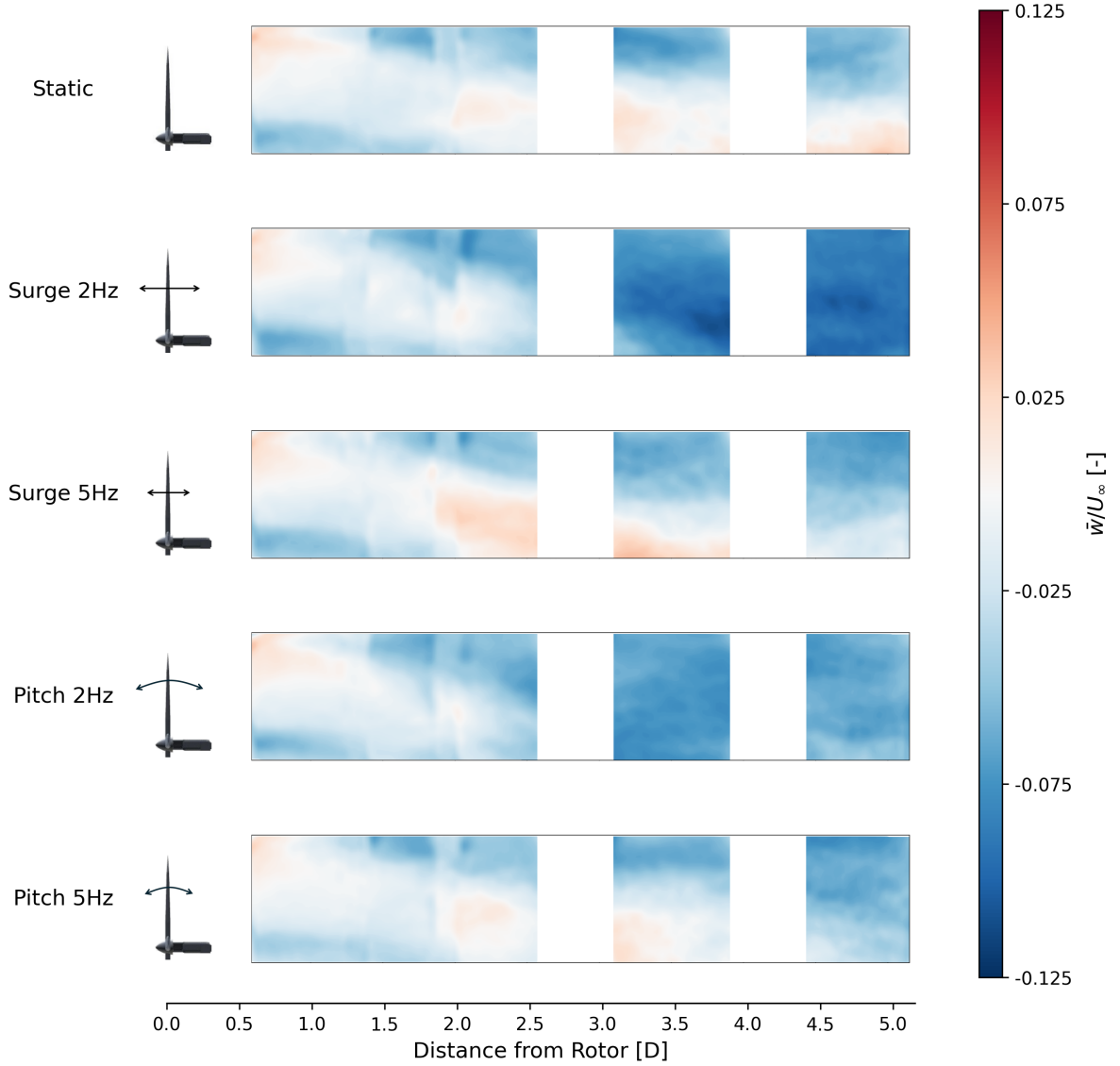

Figure 4.9: Average vertical velocity component normalized by freestream velocity $\bar{w}/U_\infty$ for static and motion cases.

The analysis of vertical velocity *w* (Figure 4.9) reveals a clear trend from the motion cases on having a considerable downwards velocity, around $-0.4m/s$, when reaching the far wake. This trend is not clearly distinguishable in the static case, but since the freestream flow also shows negative velocity, it is probable that the same state will be found as the wake develops further downstream.

This global negative velocity could be related to the observed constant negative velocity in the undisturbed flow of the wind tunnel as explained in section 3.3. However, the velocity there was only quantified to around $-0.17m/s$. This shows that even without the limitation, the studied cases present negative velocity towards the far wake. In a study characterizing the wake of a HAWT model [31], the same downwards behavior was observed. If the global negative velocity limitation is ignored, an equivalent velocity deficit to the study would be observed for these cases.

Interestingly, it is observed how the regions with positive vertical velocity match with the region where the blade passes by. The rotation of the blade, upwards motion before reaching $y = 0$ plane, has been inducing positive *Velocity w* up until this point. Exactly at this plane the blade is located at its highest point, and for the next half rotation it will shift downwards, inducing negative vertical velocity along its path.

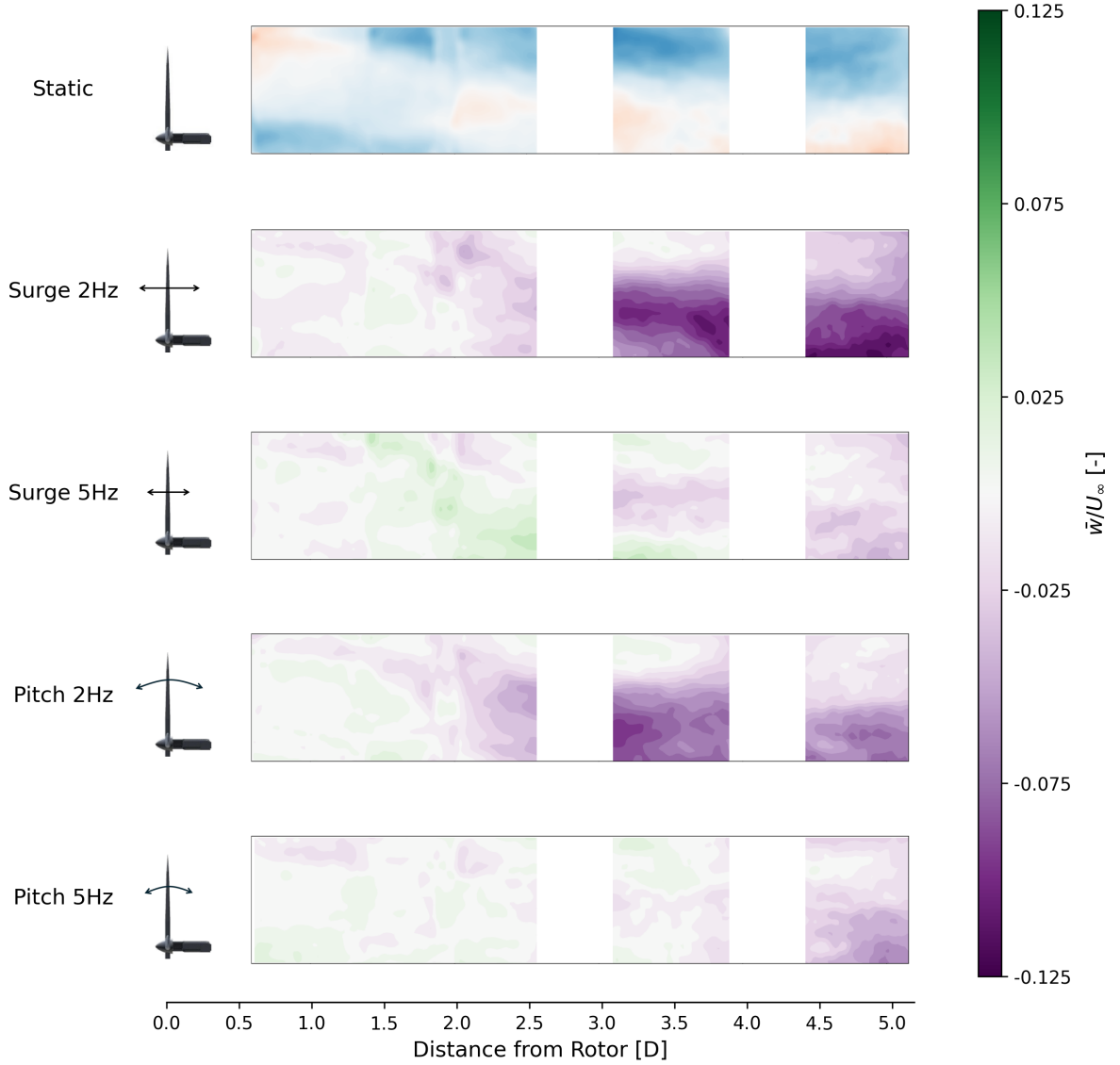

Figure 4.10: Average vertical velocity component difference between static and motion cases normalized by freestream velocity $(\bar{w}_{motion} - \bar{w}_{static})/U_\infty$. Average normalized velocity $\bar{w}/U_\infty$ for static (top image) plotted for reference.

Again the low frequency cases give the biggest differences. Both surge and pitch 2Hz have an additional $-0.4m/s$ in *Velocity w* for the last two volumes, with the effect started to be seen from just 2D distance. On the other hand, high frequency surge and pitch also see some amplification of the vertical velocity for the last volume, but it is much smaller, in the order of $-0.2m/s$.

The results and comparison for vertical velocity seem to suggest that the low frequency motions mix the wake faster when compared to the static case. Although measurements did not extend far enough downstream to precisely quantify the delay in the static case, it is estimated to take approximately 3 diameters longer to reach the same wake state. High-frequency cases also promote wake development, but they require roughly 2 diameters more than low-frequency cases to reach a similar state.

While similar conclusions can be drawn from the analysis of *Velocity u*, less straightforward information can be interpreted from *Velocity v* plots. Therefore, a more detailed discussion on wake recovery will follow in subsection 4.2.3 where the previous theories will be developed.

4.2.2. Turbulence Intensity

Turbulence Intensity (TI) is a measure of the degree of fluctuations within a turbulent flow, capturing the extent of velocity variations around the mean flow. High turbulence intensity indicates more chaotic flows, while low intensity reflects more stable and predictable behavior. The turbulence is directly related to the kinetic energy contained in the fluctuating components of the velocity field.

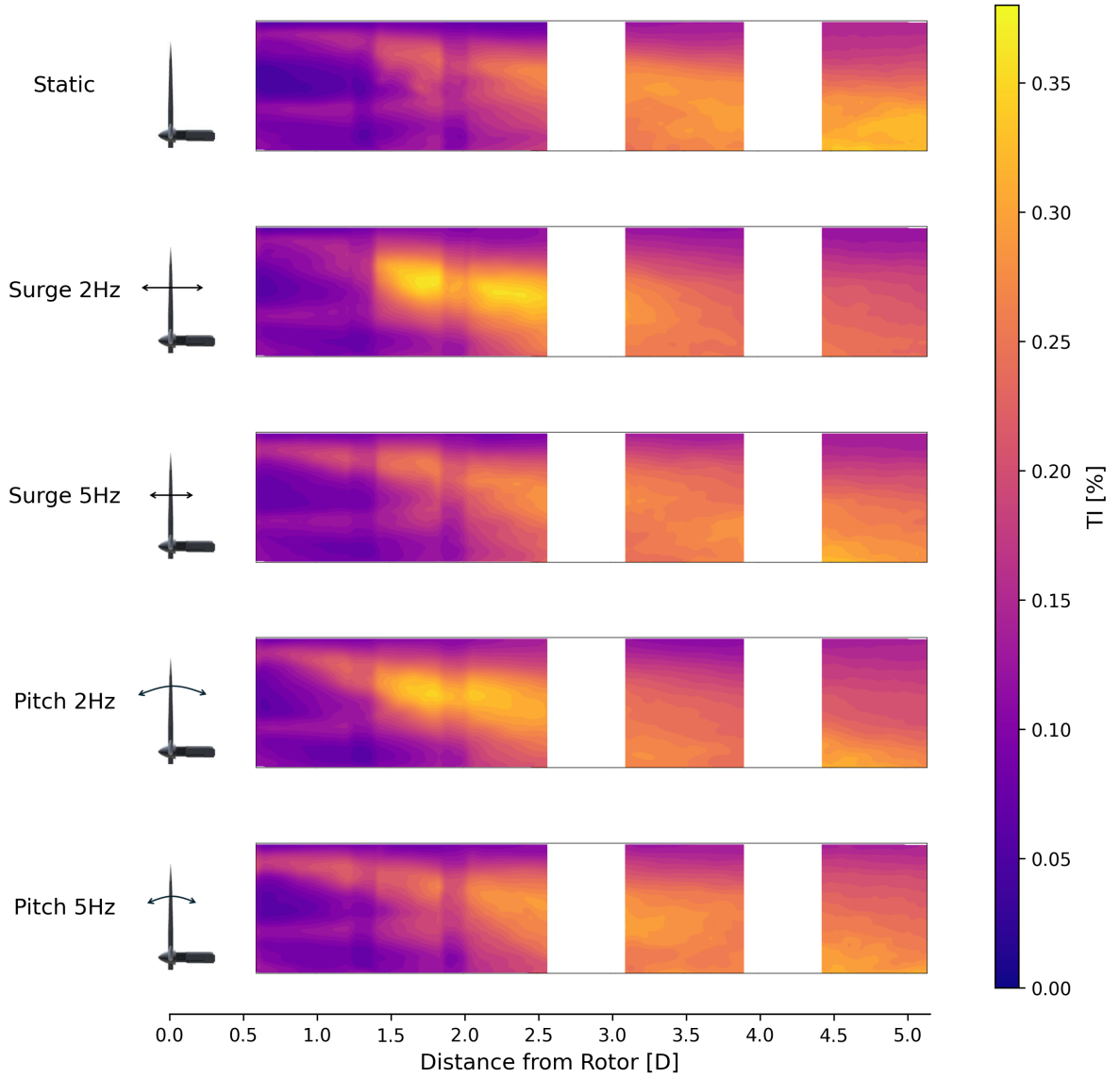

Figure 4.11: Average Turbulence Intensity TI for static and motion cases.

Shear stress between the freestream flow and the wake causes turbulence. As the shear layer expands, the turbulence reaches other areas in the domain and mixes the flow downstream. Comparing the first volume to the last, the darker areas with low turbulence gets blended with the warmer one. Additionally, with turbulence intensity, the location of blade tip and root vortices become visible. They are represented by the warmer color horizontal stripes that appear in the the first volume. While the vortices also introduce turbulence, the effects are smaller compared to the big structures caused by shear layers.

For the cases with platform motion an additional source of turbulence is introduced with the forward and backward motion of the blades. Specially for the near wake, this increases the turbulence content in the flow.

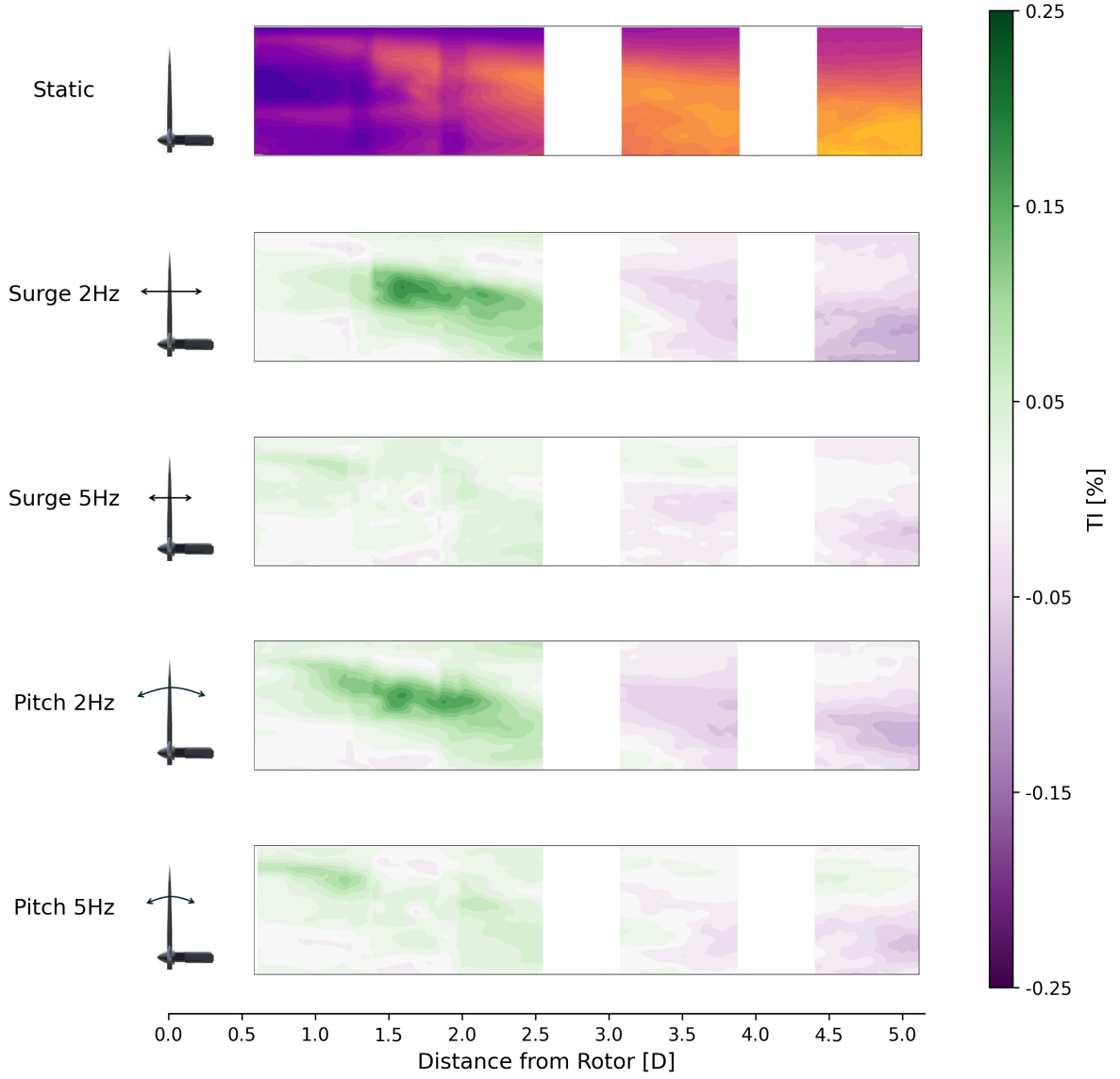

Figure 4.12: Average Turbulence Intensity difference between static and motion cases ($TI_{motion} - TI_{static}$). Average Turbulence Intensity for static (top image) plotted for reference.

Compared to the static case, motion cases induce turbulent behavior much earlier. Green dominates the first three volumes, denoting increased turbulence, and the last volumes have lower turbulence intensity because there is less turbulent energy available. Having more turbulence earlier can be seen as a benefit, as the mixing will be enhanced, and the wake can develop faster (more on this will be developed in subsection 4.2.3).

From the difference in TI plots it is, once again, evident that low frequency motions have a bigger effect on the flow. Adding up to 20% of intensity in the center of the blade wake between 1D and 2.5D. In the later volumes a lower turbulence intensity, compared to the other motions and to static, is also observed.

4.2.3. Wake Recovery

Wake recovery is a key factor in wind farm performance, as it determines how quickly the wind speed returns to its freestream value after being slowed down by the turbine. Faster recovery leads to better conditions for downstream turbines in terms of power losses and also for fatigue loading. Understanding whether FOWTs motions enhance wake development, and can therefore be beneficial at farm level, is an essential task this study.

In this analysis, wake recovery is evaluated using the velocity deficit in streamwise direction, which quantifies the reduction in wind speed relative to the freestream. This approach offers a direct and consistent measure of wake behavior across different cases. To compare the effects of turbine motion on wake recovery, velocity deficit for both dynamic and static cases are presented at several downstream distances.

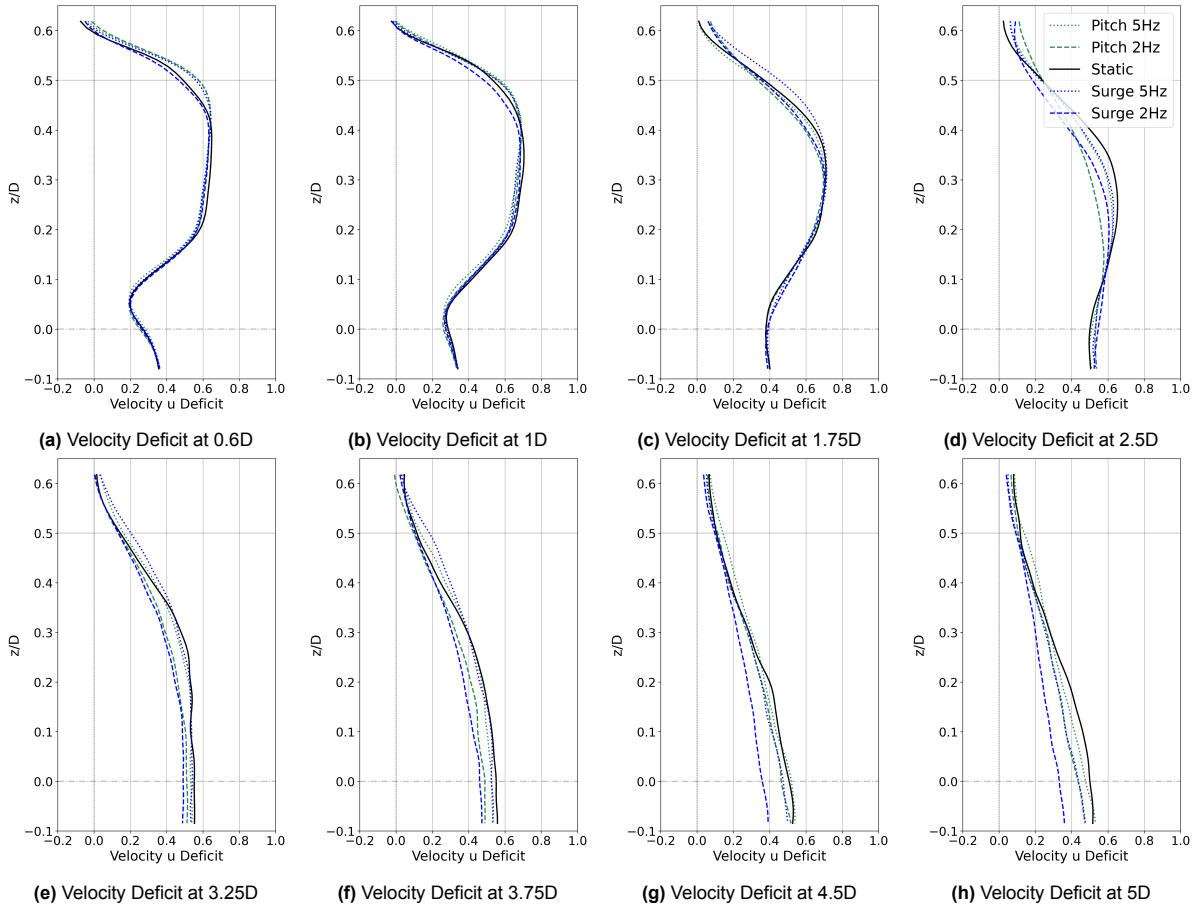

(a) Velocity Deficit at 0.6D **(b)** Velocity Deficit at 1D **(c)** Velocity Deficit at 1.75D **(d)** Velocity Deficit at 2.5D

(e) Velocity Deficit at 3.25D **(f)** Velocity Deficit at 3.75D **(g)** Velocity Deficit at 4.5D **(h)** Velocity Deficit at 5D

Figure 4.13: Wake recovery expressed as streamwise velocity deficit $(U_\infty - \bar{u})/U_\infty$ along the wake.

Surge $2\mathrm{Hz}$ exhibits the lowest velocity deficit across the entire wake among all tested configurations. It consistently outperforms the static case at all measured downstream distances. While differences between cases are minimal immediately downstream of the rotor, they become increasingly pronounced farther into the wake. At the furthest measurement location, Surge $2\mathrm{Hz}$ achieves up to a 40% reduction in velocity deficit across most of the domain (see Figure 4.13h).

Pitch $2\mathrm{Hz}$ also demonstrates improved wake recovery, with velocity deficits close to those of Surge $2\mathrm{Hz}$, though slightly less favorable overall. At the first measurement location, slightly slower velocities are observed near the wake edge ($z/D = 0.5$). Despite this, from Figure 4.13d it seems that the wake develops more rapidly downstream, with Pitch $2\mathrm{Hz}$ outperforming other cases at 2.5D. However, the effect of this motion is smaller, as for the following measured distances it only shows around 15% deficit

reduction at 3.75D (10% worse than Surge $2\mathrm{Hz}$), and close to 20% for the last distance (20% worse than Surge $2\mathrm{Hz}$).

Surge $5\mathrm{Hz}$ provides significantly less benefit compared to the low frequency cases. Up to 3.75D, its performance closely resembles the static case within the range $z/D = -0.1$ to $z/D = 0.3$, with the upper portion of the wake remaining slower. Only at the final two measurement locations Surge $5\mathrm{Hz}$ begins to show signs of improved wake recovery. At that point, its deficit profile overlaps with that of Pitch $2\mathrm{Hz}$, showing most of the deficit improvement far away from the edge of the wake.

Pitch $5\mathrm{Hz}$ shows the least improvement among all motion cases. Like Surge $5\mathrm{Hz}$, it only begins to outperform the static case in the final measured volume. In earlier measurements, its velocity deficit remains nearly indistinguishable from that of the static configuration. Nevertheless, Pitch $5\mathrm{Hz}$ consistently shows marginally higher velocities than Surge $5\mathrm{Hz}$ in the near wake region.

In summary, low-frequency motions enhance wake recovery more effectively than high-frequency ones, with surge motions generally outperforming pitch. Surge $2\mathrm{Hz}$, in particular, shows consistent and significant improvement across the entire wake, making it the most effective sinusoidal case tested. The underlying reasons for this behavior are discussed in the following sub-section with the help of the x - z component of the Reynolds Stresses.

Reynolds Stress $\overline{u'w'}$

This Reynolds stress component provides insight into the vertical transport of streamwise momentum caused by fluctuations, essentially capturing the effect of turbulent momentum exchange. Vertical mixing driven by this mechanism can draw higher momentum air from above the rotor down into the wake, helping to re-energize the flow and further reduce the velocity deficit. By analyzing $\overline{u'w'}$, one can assess how effectively and rapidly the wake recovers, offering a quantitative measure of wake dynamics and mixing behavior.

By analyzing the static case in Figure 4.14 the vertical mixing is noticed. Near the blade tip, the negative value of $\overline{u'w'}$ denotes the trend of downward transport of momentum, reveals that faster-moving air is being mixed into lower regions of the flow. As the shear layer develops downstream, the magnitude of the Reynolds stress increases, reflecting continued momentum transfer from the undisturbed freestream into the wake. In the region between the blade root and the turbine hub where there is no airfoil profile (from rotor center to $r/R = 0.18$), faster airflow is also being mixed into the wake. The red region indicates upward momentum transport, as high speed flow rises behind the wake, while the blue region below reflects downward mixing of momentum associated with the wakes from the nacelle and tower.

Focusing on the low frequency motions, a higher intensity $\overline{u'w'}$ in observed for the near wake. A higher momentum exchange leads to more mixing of the freestream with the wake, and thus explains the smaller wake deficit seen in Figure 4.13. Less mixing is happening for the last two volumes, which is probably related to the fact that the velocity difference between the wake and the freestream is not as big as for the static case, thus the need for mixing reduces. Little change is observed for the region behind the wind turbine nacelle, it remains fairly similar between all cases.

The high frequency cases barely show any difference to Static. Only between 2D and 4D a slighly deeper tone of blue is noticeable, then resulting in slightly less intense $\overline{u'w'}$ for the last volume. The $5\mathrm{Hz}$ motions are not intense enough to make an impact in the flow's vertical mixing, thus a quasi-static wake recovery is observed for the entire domain.

In summary, the larger motion associated to the low frequency cases enhance vertical mixing between the freestream and the wake, especially in the near wake region. This mixing increases turbulence and accelerates the re-energization of the wake, resulting in a faster recovery of velocity. The effects results in earlier wake development when compared to the static case. These findings align with the turbulence intensity plots presented in subsection 4.2.2, now it can be seen that the turbulence primarily originates from enhanced vertical momentum exchange. If this trend continues, the Surge $2\mathrm{Hz}$ case could potentially reach freestream velocity values up to two rotor diameters earlier than the static case (based on extrapolated data and similar studies [24], see Appendix B). However, the recovery behavior could evolve differently further downstream where no data is currently available.

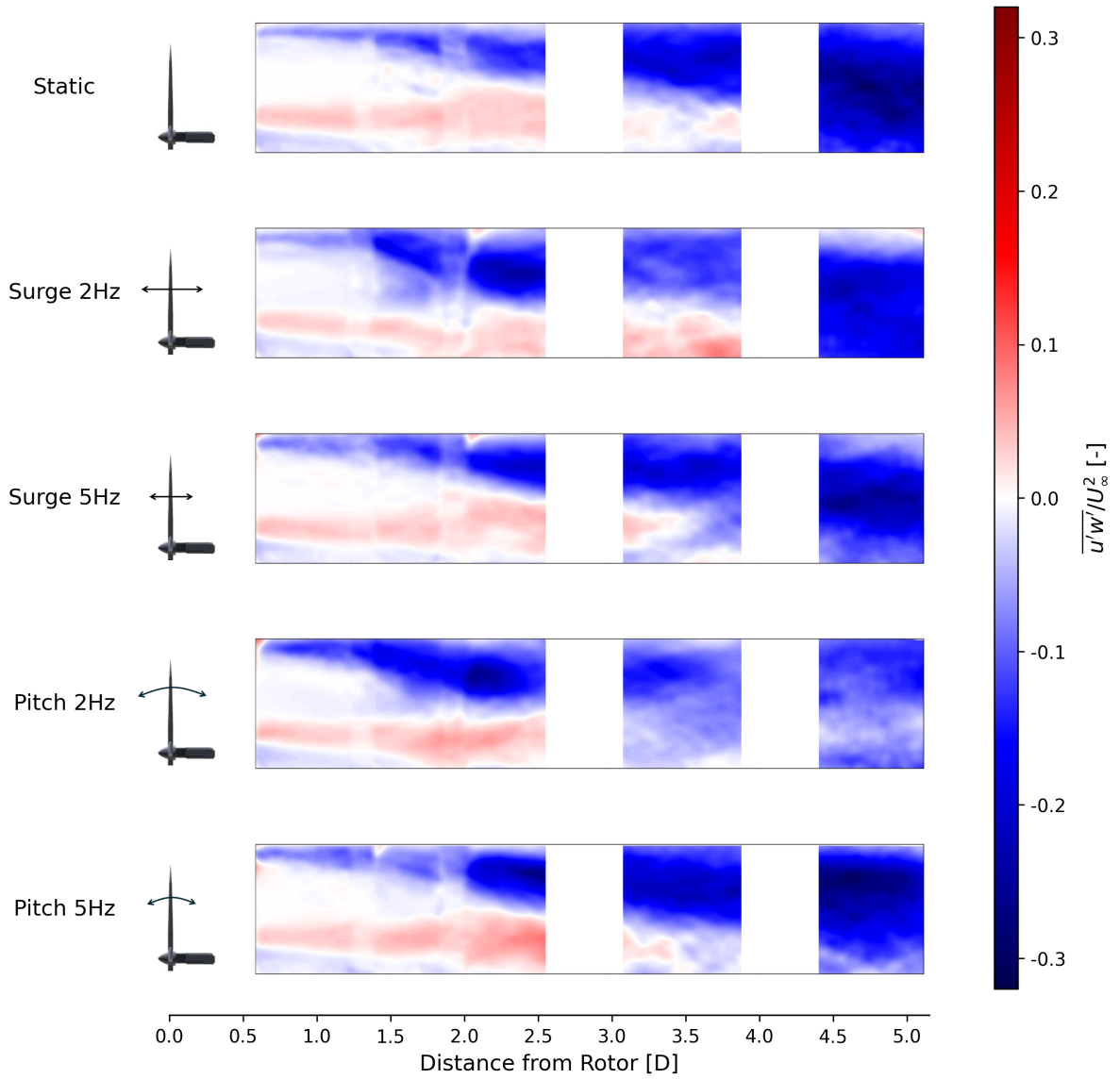

Figure 4.14: Average XZ component of Reynolds stresses normalized by the freestream velocity $\overline{u'w'}/U_\infty^2$ for static and motion cases.

4.2.4. Additional Studies: $\Delta V^* = 0.05$ & Waves Cases

Complementary to the main core of the experimental study, other cases were run with the aim of enhancing understanding and validate the observed trends. To study the influence of the amplitude of the motions, a smaller normalized velocity variation (ΔV^*) is used. And additionally two different wave cases are run, recreating real life wind and sea conditions to assess whether the tested sinusoidal motions accurately reflect the environmental dynamics experienced by FOWTs.

These cases were measured exclusively at a distance of 3.1 to 3.75 rotor diameters downstream, representing a compromise between the near and far wake regions. For the smaller ΔV^* a value of 0.05 was selected, as it builds on the study performed with a quasi-identical setup a year prior by [7]. As noted in the test matrix (subsection 3.2.3) the amplitudes of the motions are now 15.9mm and 6.4mm for surge low and high frequency respectively, and 0.79deg & 0.32deg for pitch low and high frequency respectively. The acquisition time was 10s at a frequency of 400Hz, like all the previously measured volumes.

However, for the wave cases, the run time was increased to 20s to account for longer periods within the wave pattern motions. Thanks to the HIL interactive system, the aerodynamic forces affecting the rotor are integrated within the wave simulation in real time, improving the reality of the cases. Two different wave cases were tested, each representing a different sea state. The first one (*Wave Case 1*) symbolizes a moderate sea state with 2.2m wave height, and the second one (*Wave Case 2*) imposes a rough sea state with higher waves. Additionally, note that the freestream velocity also changed depending on the strength of the wave case, as it can be seen in Table 4.1 below:

	H_s [m]	T_p [s]	Full U_∞ [m/s]	Full RPM	Scaled U_∞ [m/s]	Scaled RPM
Wave case 1	2.2	8	10.3	8.26	3.43	408
Wave case 2	3.04	9.5	11.4	9.6	3.8	474

Table 4.1: Wave cases with corresponding wave heights (H_s), wave peak periods (T_p), wind speeds and rotor speeds for both the full scale FOWT and the scale model used in the experiment.

Velocity deficit line plots will be used to quantitatively show the influence of the motion cases for Surge (Figure 4.15) and Pitch (Figure 4.16), and the Wave Cases (Figure 4.17). The wave deficit is additionally plotted against the surge cases, with $\Delta V^* = 0.1$, for easy comparison. In addition, complementary contour plots will be present in Appendix C.

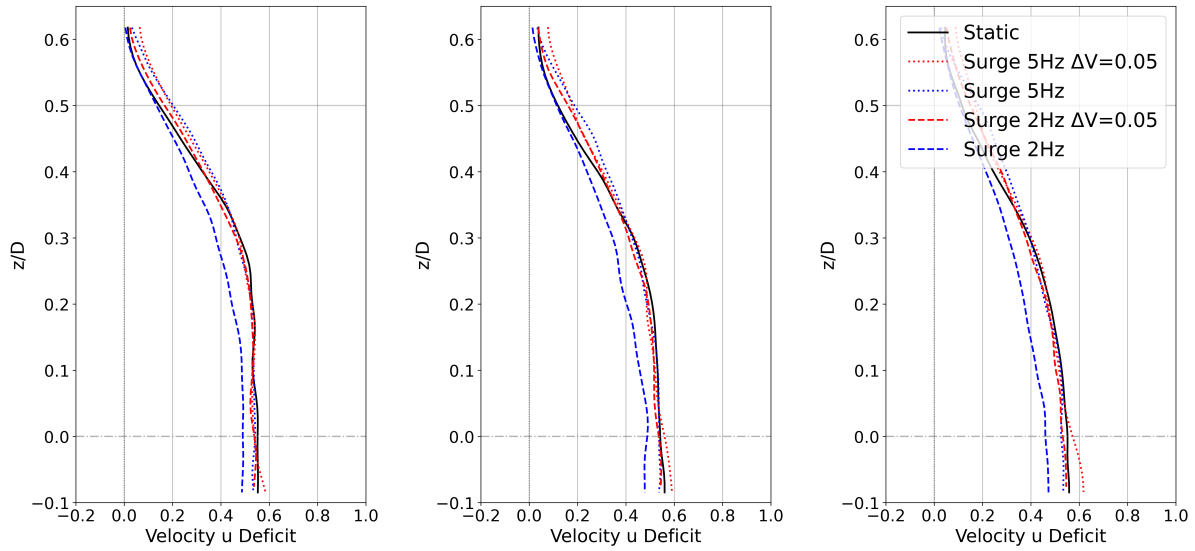

(a) Velocity profile at 3.25D **(b)** Velocity profile at 3.5D **(c)** Velocity profile at 3.75D

Figure 4.15: Streamwise velocity deficit normalized by the freestream velocity $(U_\infty - u)/U_\infty$ for Surge motions with $\Delta V^* = 0.1$ & $\Delta V^* = 0.05$

The original 2Hz motion studied in this experiment is the one giving the best overall results, especially in the area right behind the rotor (up to $z/D = 0.5$). On the other hand, the smaller amplitude 2Hz motion barely shows any improvement over the static case, and it even has a higher deficit towards the edge of the wake. Similarly, for the smaller amplitude 5Hz motion, no clear improvement is noted. In some regions $\Delta V^* = 0.05$ works slightly better than 0.1, but in others like the edges of the measured volume, a worse recovery is seen.

To try understand why $\Delta V^* = 0.05$ amplitudes do not perform as well as larger ones, delta TI with respect to Static is plotted including all cases for proper comparison (see Figure 4.18). An increase of approximately 7% in turbulence intensity (TI) is observed for the Surge 2Hz case with smaller amplitude ($\Delta V^* = 0.05$) compared to the larger amplitude case ($\Delta V^* = 0.1$). This elevated TI is likely responsible for the slower velocity profile. In contrast, the larger amplitude case induces higher TI earlier in the flow due to stronger motions, as it was seen in subsection 4.2.2, which enhances shear layer mixing and leads to faster wake recovery. The smaller amplitude, however, is less effective in promoting this mixing, resulting in delayed turbulence and slower wake recovery. For the high-frequency cases (5Hz), the differences in TI are much smaller (less than 3%), leading to nearly identical velocity profiles.

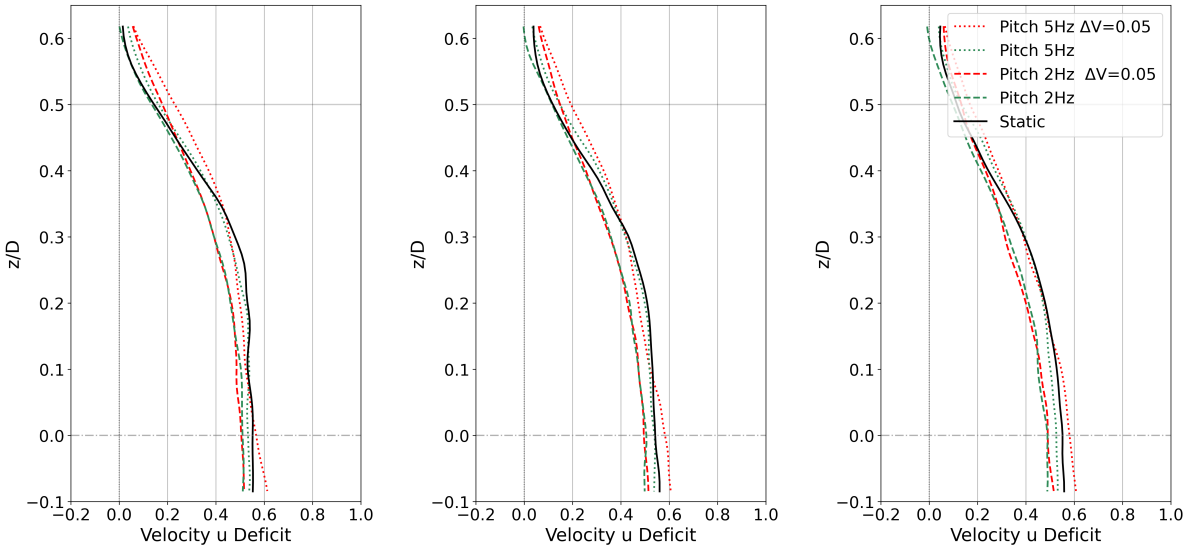

(a) Velocity profile at 3.25D **(b)** Velocity profile at 3.5D **(c)** Velocity profile at 3.75D

Figure 4.16: Streamwise velocity deficit normalized by the freestream velocity $(U_\infty - u)/U_\infty$ for Pitch motions with $\Delta V^* = 0.1$ & $\Delta V^* = 0.05$.

For the pitch motion cases, a slightly different trend is observed: both 2Hz amplitudes show a good match in velocity deficit across most of the domain, with only a slightly slower flow near the wake edge in the $\Delta V^* = 0.05$ case. As with the surge case, the 5Hz frequency does not demonstrate a clear improvement. While $\Delta V^* = 0.05$ performs similarly to 0.1 in some regions, particularly near the center, it shows a slower flow in others, such as at the bounds of the measured volume.

The plots in Figure 4.18 show that the low-frequency cases exhibit similar turbulence intensity (TI) levels, mostly below 3% across the domain, resulting in similar velocity profiles. In contrast, the 5Hz case displays more pronounced differences. In particular, the $\Delta V^* = 0.05$ case shows a significant increase in TI (exceeding 7%), especially near the top and bottom of the wake. This elevated turbulence shows that the mixing of the wake with the freestream velocity is happening at this location, rather than in earlier volumes like for Pitch 5Hz $\Delta V^* = 0.1$, and thus a slower flow is observed here in these locations.

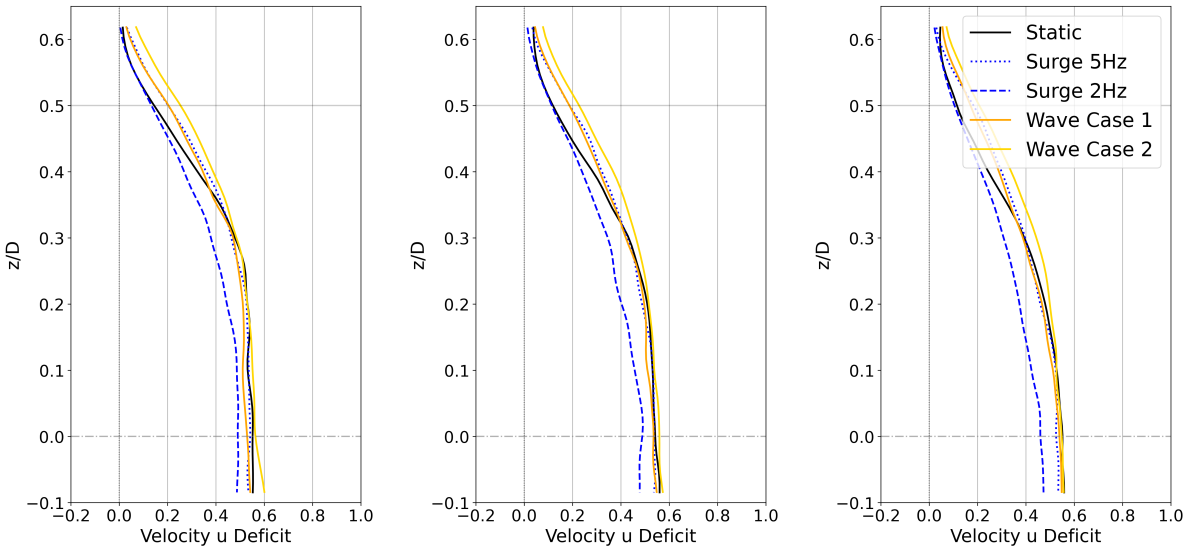

(a) Velocity profile at 3.25D **(b)** Velocity profile at 3.5D **(c)** Velocity profile at 3.75D

Figure 4.17: Streamwise velocity deficit normalized by the freestream velocity $(U_\infty - u)/U_\infty$ for Wave cases (Surge cases included for comparison purposes).

Although the two wave cases use a different freestream velocity, normalization allows for a meaningful comparison with Static and Surge. The rough wave case, *Wave Case 2*, clearly under performs when compared to the other motions. Around 5% slower velocity is consistently measured for heights higher than 0.25D. On the other hand, *Wave Case 1*, matches greatly the $5\mathrm{Hz}$ motion, suggesting that Surge $5\mathrm{Hz}$ could be a realistic representation of moderate sea state waves, in terms of effects on the wake.

The slower flow for the wave cases, compared to the static case, suggest that worse wake recovery is experienced for FOWTs compared to HAWTs. This is a strong conclusion for a very sensitive topic, as this would mean that the spacing in floating offshore farms needs to be larger to allow for the same efficiency as traditional wind farms. However it is important to note that it is difficult to judge by just looking at a small volume, and more downstream distances should be researched to verify this trend. For example, benefits could be seen later, if the moderate wave follows the same trajectory as Surge $5\mathrm{Hz}$ (see Figure 4.13h),

From the TI plots the similarities of *Wave Case 1* to Surge $5\mathrm{Hz}$ continue. Identical patterns, and also similar to Pitch $5\mathrm{Hz}$, foments the theory that high frequency, $\Delta V^* = 0.1$ motions are a good representation of a moderate sea state. On the other hand, the rough sea state show little similarity to other cases. The high intensity seen in this volume might be the representation of a delayed wake development, explaining the slower velocity. On the other hand, it probably also shows the added intensity due to the rougher motions of the sea.

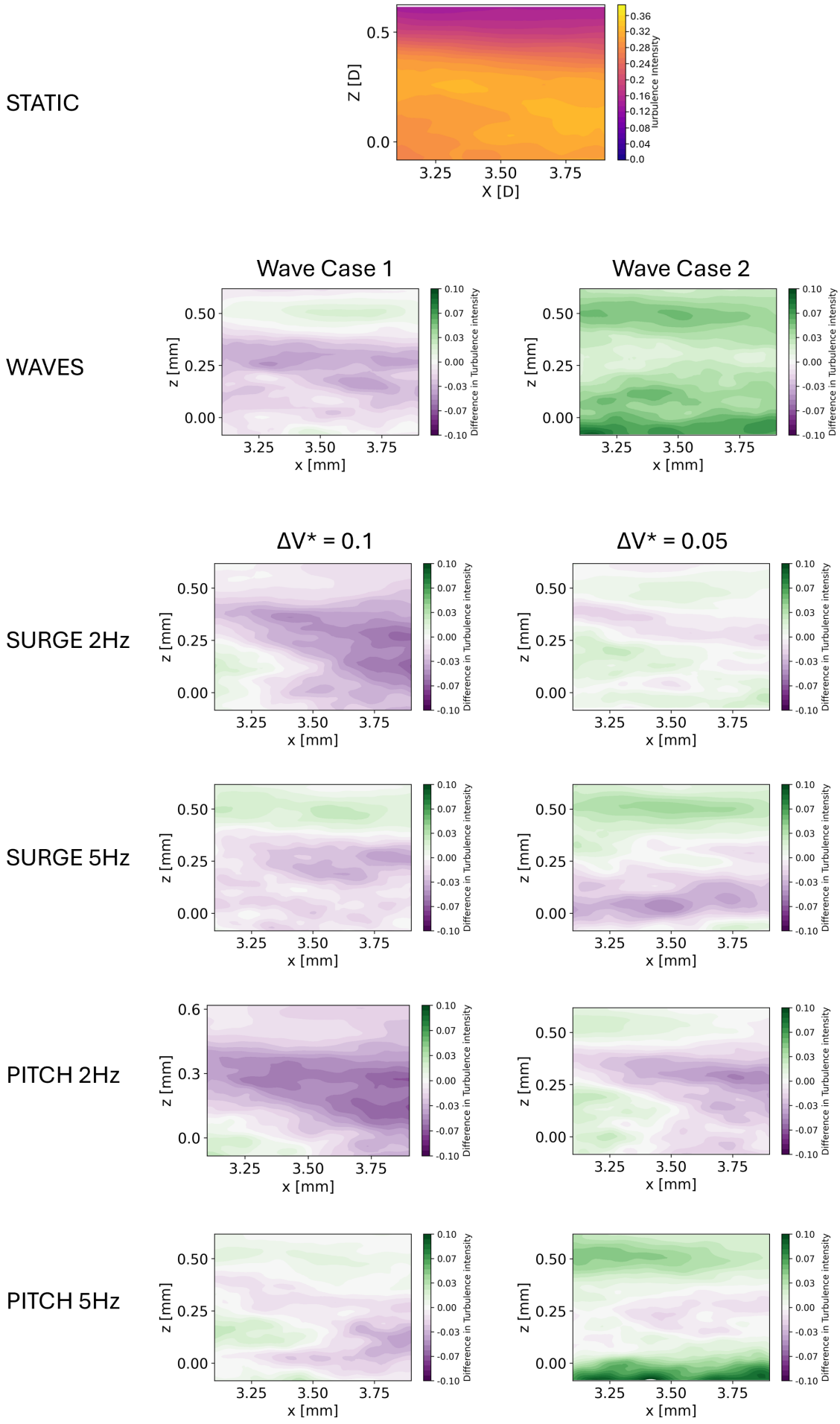

Figure 4.18: Turbulence Intensity TI for $\Delta V^* = 0.1$, $\Delta V^* = 0.05$ & Wave cases.

4.3. Phase-Locked Flow Analysis

To visualize and quantify how motions affect the flow at a specific moment in time, the acquisition is phase-locked with the floating motion. Periodically averaged flow fields are obtained by sorting instantaneous velocity fields according to different phases of the surge or pitch cycle. A trigger was activated based on the hexapod position: specifically, when the wind turbine had zero displacement and a negative velocity in the streamwise direction: moving against the wind ($x = 0$ mm, $u < 0$).

The duration of each cycle varied with the motion frequency (e.g., a $2\mathrm{Hz}$ frequency corresponds to 200 measurements per cycle), which defined the segment length used for phase discretizations. Each cycle was evenly divided into four key positions (see Figure 4.19):

- Pos 1: $x = 0$, $u < 0$ (moving against the wind),
- Pos 2: $x = -\max$, $u = 0$,
- Pos 3: $x = 0$, $u > 0$ (moving with the wind),
- Pos 4: $x = \max$, $u = 0$.

By selecting these distinct phases and applying periodic phase shifts, the average flow field corresponding to each position can be computed.

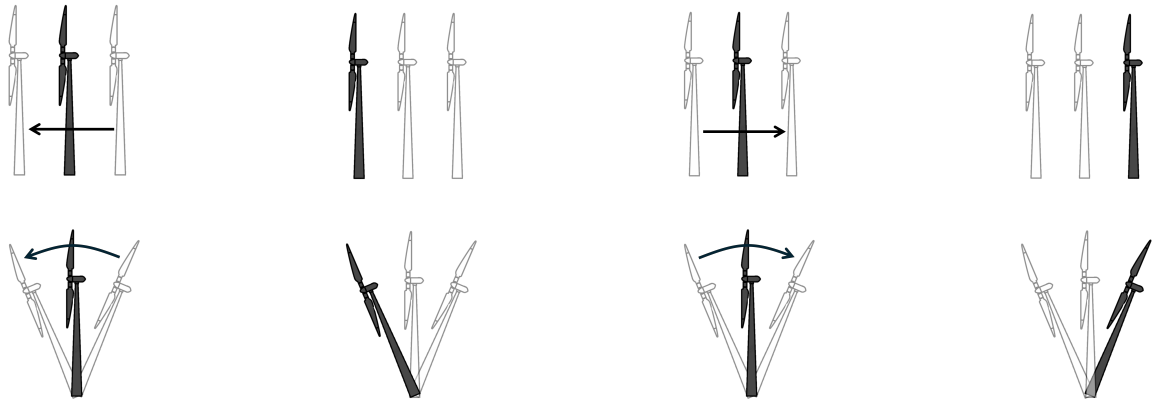

(a) Pos 1 **(b)** Pos 2 **(c)** Pos 3 **(d)** Pos 4

Figure 4.19: Studied positions for the phase-locked analysis.

Due to the fixed total measuring time across all cases, the number of instantaneous vector fields available for the phase-locked average varies with the motion frequency. For example, a full cycle consists of 80 images at $5\mathrm{Hz}$, resulting in 50 images used for averaging, compared to only 20 at $2\mathrm{Hz}$. While this discrepancy does not affect result convergence, as demonstrated in section 4.1, additional interpolation is applied during plotting to ensure comparable smoothness across datasets.

An example on how phase-locked averaging at four different positions is shown in Figure 4.20, where the vertical velocity component ”w” is used to visualize flow displacement. Based on the motion of flow structures in the plots, an estimate of the wake convection speed can be made. For the $2\mathrm{Hz}$ case, a structure displacement of 0.8D (0.96m) over one cycle (0.5s) yields a convection velocity of approximately 1.92m/s. Similarly, for the $5\mathrm{Hz}$ case, an observed displacement of 0.35D (0.42m) over one cycle (0.2s) corresponds to a velocity of roughly 2.1m/s. This represents the total convection across the entire height of measured wake, in previous chapters the slowest section of the wake, behind the airfoil profile section of the blade, was estimated around 1.2m/s.

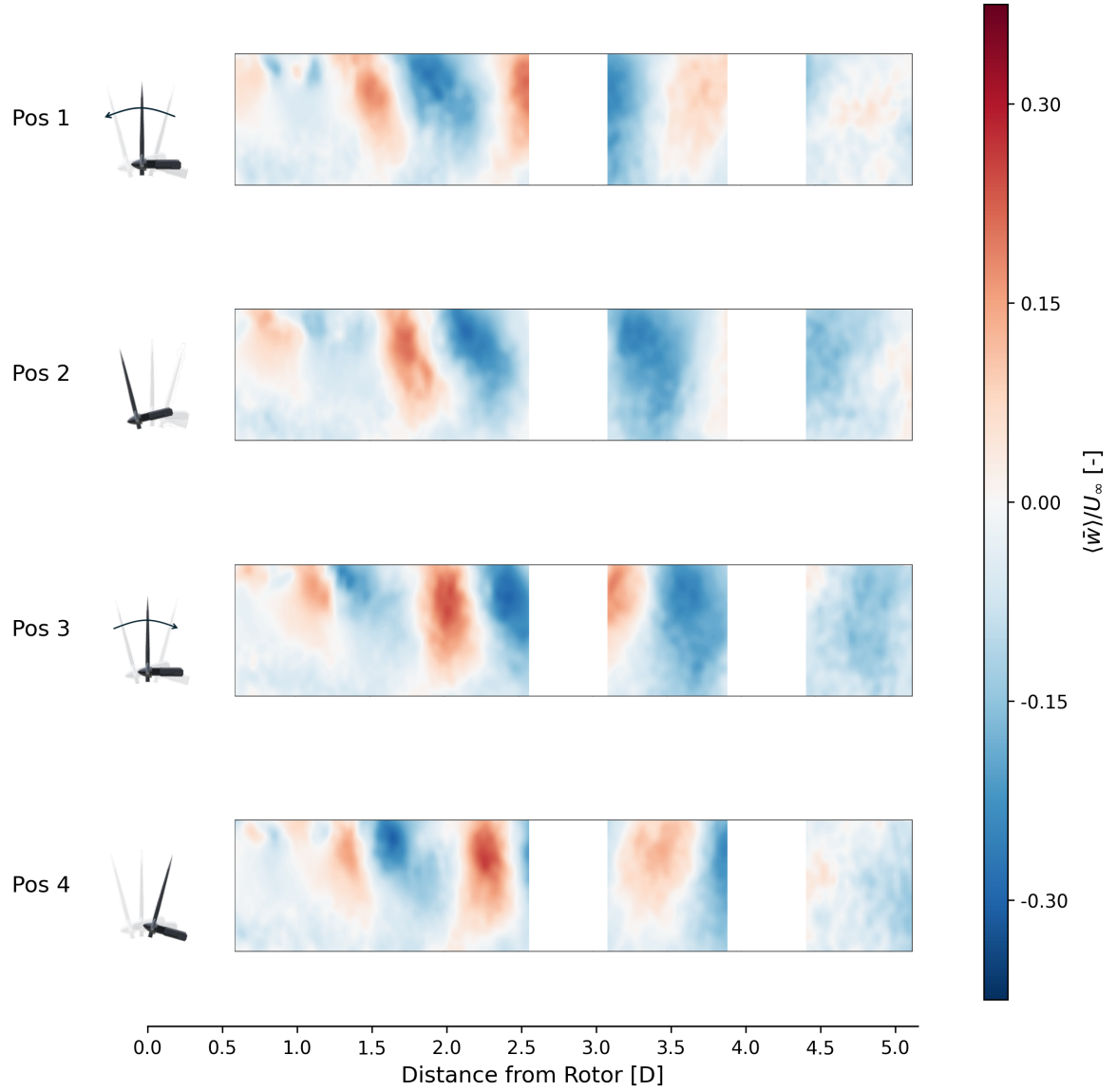

Figure 4.20: Phase-locked averaging results shown with a spacing of 50 images between positions, corresponding to 0.125s for a 2Hz frequency. Normalized vertical velocity ($\langle \bar{w} \rangle / U_\infty$) for Pitch 2Hz is used for illustrative visualization.

By plotting the flow related to the different positions next to each other, the wake movement downstream becomes evident. However, each individual plot offers limited additional insight beyond the others: knowing the convection speed, the effect of a certain motion can be related to the location in the plot. Thus, to avoid repetition of figures, only the figures for ”Pos 1” will be presented in the following subsection, while the remaining positions are included in Appendix D.

4.3.1. Velocity Components

From the x component of the velocity, a vertical oscillating, meandering-like, motion is clearly visible for the low frequency cases. Some oscillation can also be seen for the high frequency cases, however the amplitude is much smaller, and the case is more similar to Static than relatable to any motion. This can further be supported from the last volumes where there is barely any distinction with the time-averaged cases seen in subsection 4.2.1.

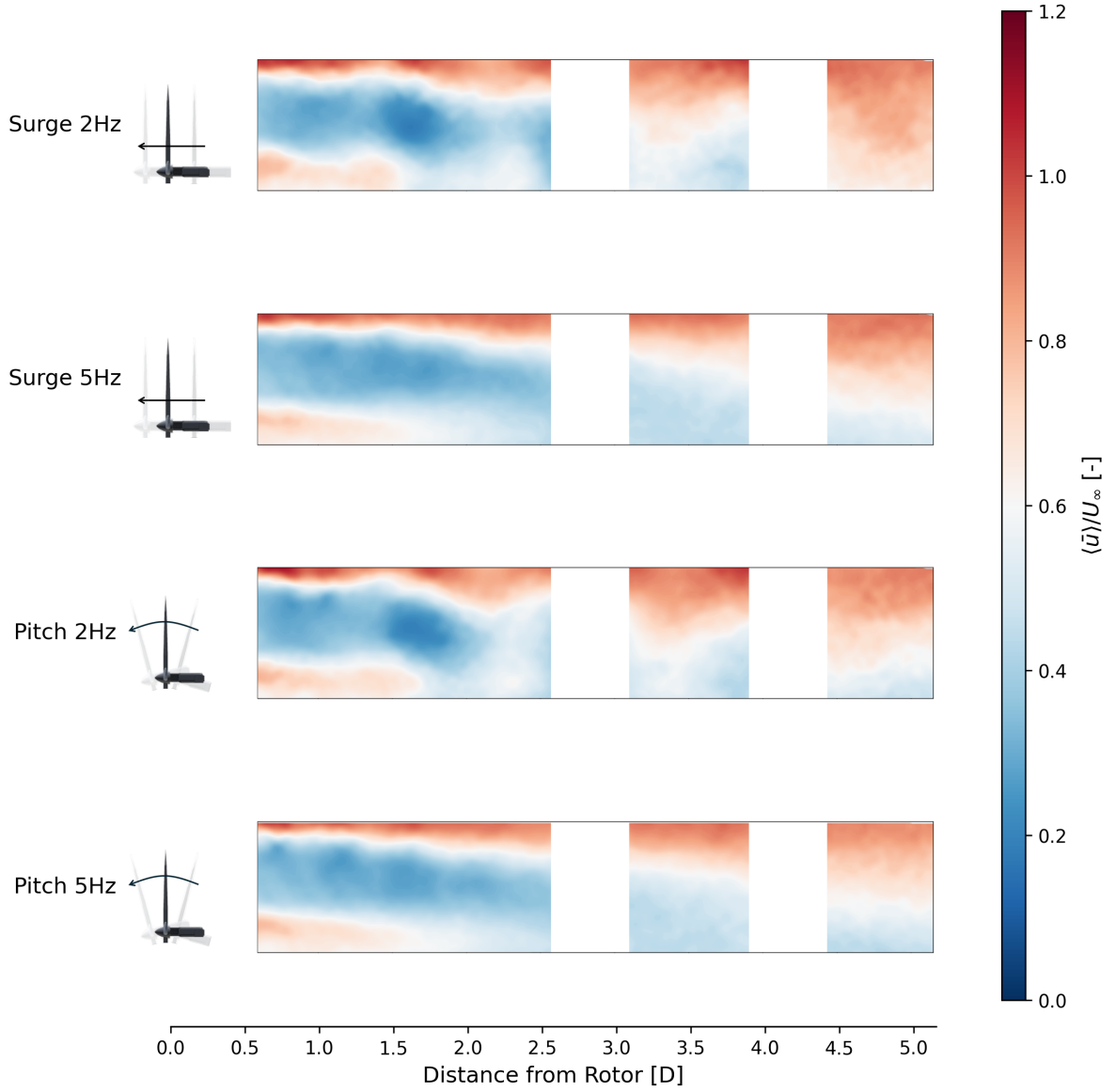

Figure 4.21: Phase-locked average streamwise velocity component normalized by freestream velocity $\langle\bar{u}\rangle/U_\infty$ for static and motion cases at Position 1.

In the low frequency cases we can see the influence of the forward motion of the FOWT thanks to the darker blue regions in the near wake. More specifically, this slower moving air is located at around 0.9D and 1.75D, which is consistent with these effects being due to the motion of the wind turbine at ”Pos 1”. Compared to the unconditioned time averaged flow seen in subsection 4.2.1 where the velocity inside the wake was around 1.3m/s, the wind turbine motion against the flow reduces the speed further to around 0.5m/s. On the other hand the contrasting regions, 1.3D and 2.2D, represent the motion of the FOWT moving with the flow: ”Pos 3”. Here the flow speed is increased to around 2m/s due to the additional rotor influence. Thus, the maximum effect of a 2Hz motion can be quantified to around $\pm$0.75m/s depending on the forward or backward motion of the wind turbine.

For the high frequency cases, the effect of the motion is less pronounced. The cycle length is approximately 0.4D, resulting in alternating patterns: darker regions appear at 0.8D, 1.2D, 1.6D, 2.0D, etc., while lighter regions occur at 1.0D, 1.4D, 1.8D, and so on. The low-velocity regions reach minima around 0.9m/s, while the high-velocity regions exceed 1.5m/s. Therefore, the maximum velocity variation due to the 2Hz motion can be quantified as approximately $\pm$0.3m/s, depending on whether the turbine is moving forward or backward.

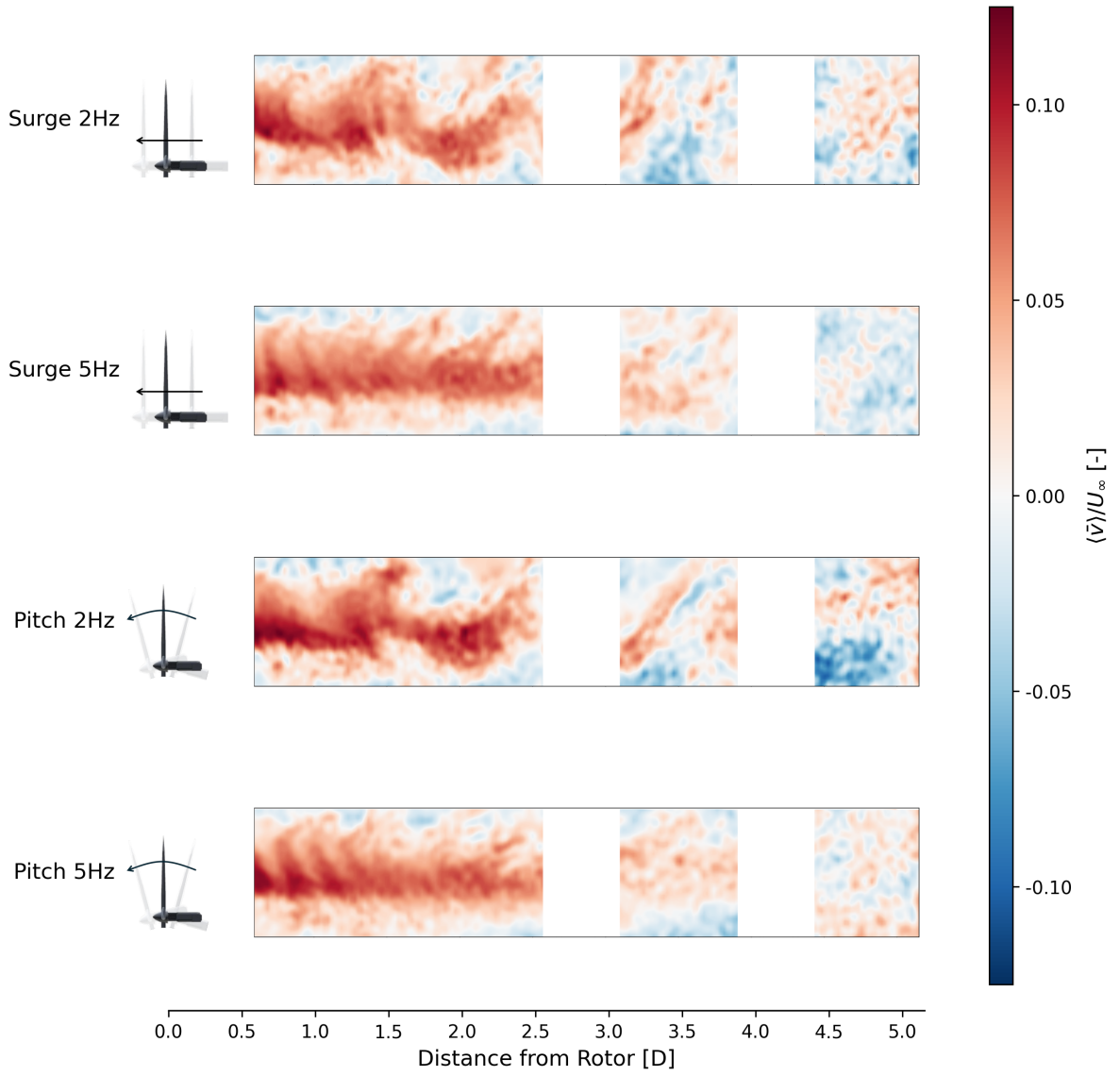

Figure 4.22: Phase-locked average spanwise velocity component normalized by freestream velocity $\langle \bar{v} \rangle / U_\infty$ for static and motion cases at Position 1.

With the phase-locked averaged cases same low frequency oscillations as before are observed for spanwise velocity *v*. But interestingly, for high frequency cases the darker positive velocity areas seem to be closer to each other than previously seen for x component of velocity. Blade passing effects are most likely affecting these plots, as they have high influence in lateral velocity.

The wake rotating effects disappear around the same location for all cases, no pattern recognizable after 4D. This matches with some experimental studies [52], while others still see wake rotation around 5D [31].

Vertical velocity *w* is probably the best possible option to visualize and quantify surge and pitch effects. The effect is most intense, in Figure 4.23 the colorbar scale has changed from ± 0.5 back in the unconditionally averaged flow, to ± 1.5 for this phase-locked analysis. The observed influence will result from a combination of both the forward and backward motion of the turbine, as well as, in pitch cases, the effect of the rotor being tilted at an angle in its most forward and aft positions. When the rotor is angled, the wake deflects in the opposite direction of the tilt. In example, when the turbine reaches its most aft position (tilted backward) the wake will naturally exhibit an initial upward trajectory.

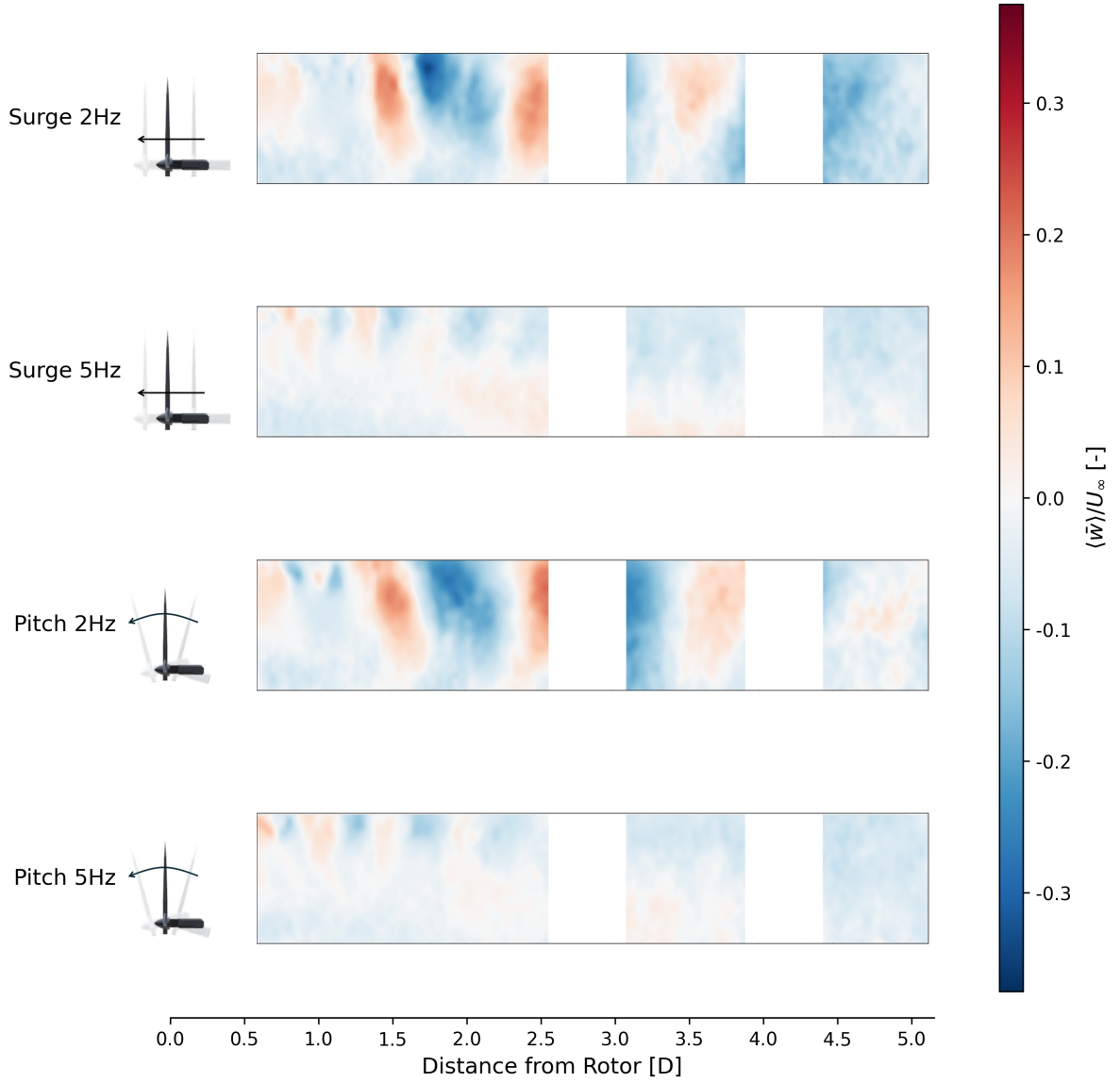

Figure 4.23: Phase-locked average vertical velocity component normalized by freestream velocity $\langle \bar{w} \rangle / U_\infty$ for static and motion cases at Position 1.

Once again, the most pronounced influence of the motion is observed in the low-frequency cases. Distinct clusters of darker regions, exhibiting consistent intensity, appear at regular intervals of approximately 0.8D. The influence gradually intensifies as the wake develops, with minimal changes observed in the first 1.2D. The effect then increases considerably, until reaching around 4.5D.

The region with the most positive vertical velocity is relatively narrow, reaching about 1m/s upward. This occurs during ”Pos 3”, when the turbine moves with the flow, displacing air outward from the wake, and continues into ”Pos 4”, where the rotor deflects air upward due to its tilt. In contrast, the regions of downward vertical velocity are slightly wider and reach higher magnitudes, around 1.2m/s. This may be attributed to the lower streamwise velocity observed in those zones (Figure 4.21). The negative vertical velocity corresponds to ”Pos 1”, where the rotor moves against the flow and air is drawn in to fill the low pressure region behind the turbine, and continues through ”Pos 2”, where the backward tilt of the rotor forces air downward.

While the influence of the high frequency cases is considerably small compared to the low frequency ones, the effect is still visible. Positive and negative velocity clusters are seen every 0.4D, but the

intensity remains just below $\pm$0.4m/s for both pitch and surge. Additionally, it is observed how the flow reaches constant negative velocity in the last volumes, which is the same behavior seen in the unconditional time averaged flow representation. Suggesting no motion influence reaches further than 3D.

4.3.2. Turbulence Intensity

Turbulence intensity in Figure 4.24 shows once again that the behavior of the $5\mathrm{Hz}$ motions is similar to the static case. The shear layer mixes the flow creating turbulence which grows until covering the entire domain around 3.5D.

Oscillations can be distinguished for the low frequency cases. Up to the last volume, the effects from *Velocity v* and *Velocity w* play an important role in mixing the flow, and similar patters are seen here. Around 1.5D a clear sudden increase in TI occurs, likely related to the vertical velocity, which then is convected downstream with similar intensity. The direction of the turbine, forward or backward, does not seem to influence the outcome of the plot. Similar intensities are experienced between 1.5D and 2.5D, where the effect of the motion already diminishes.

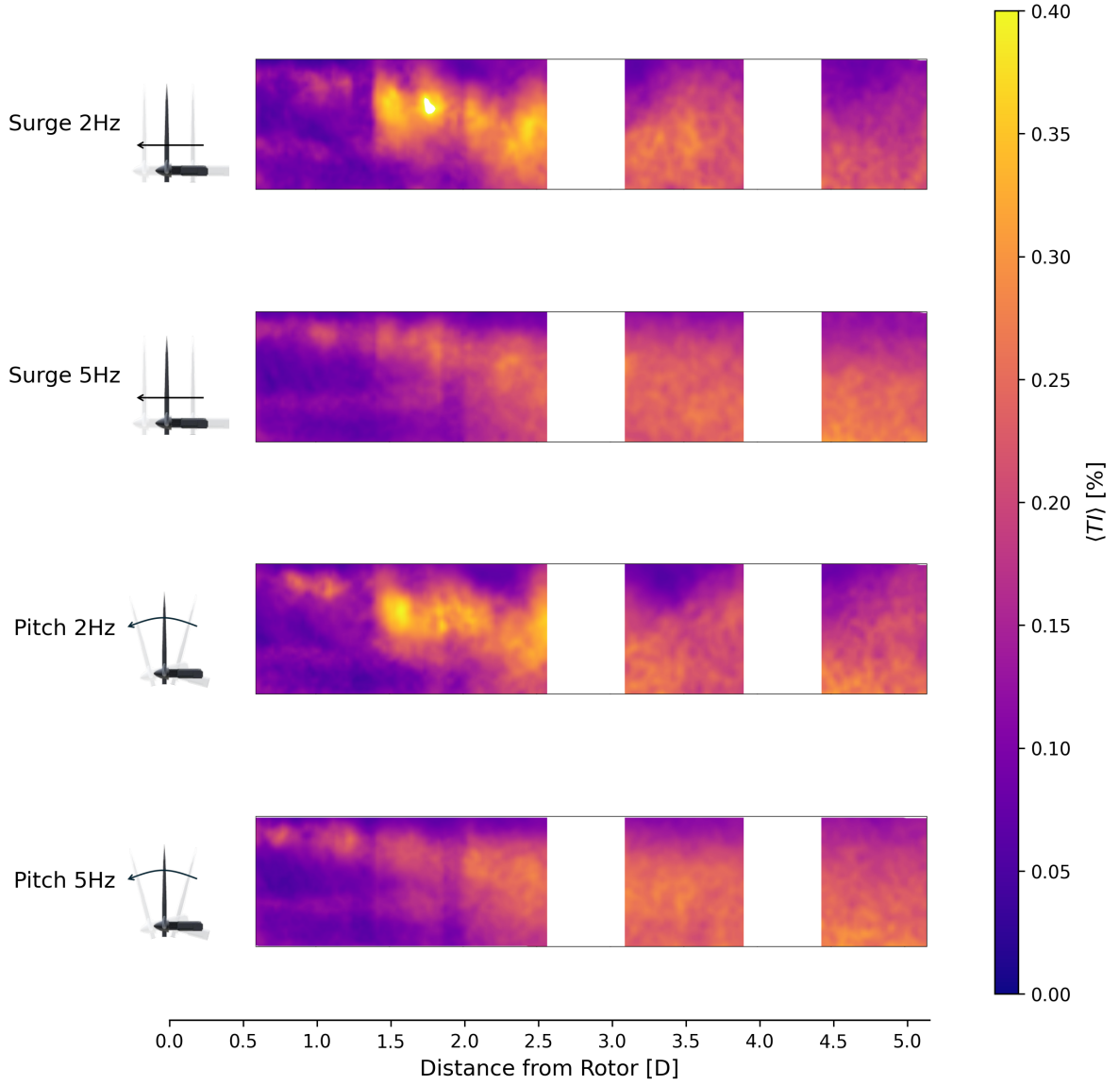

Figure 4.24: Phase-locked average turbulence intensity $\langle TI \rangle$ for static and motion cases at Position 1.

4.4. Tip Vortex Evolution

The aim of this section is to provide a detailed analysis of the vortex structures shed from the blades of the DTU 10MW wind turbine model, and to examine how these structures behave under the specific conditions of this experiment. The evolution of the wake is strongly influenced by several parameters, including the tip speed ratio [31], inflow orientation [35], and turbulence intensity [81]. Understanding this behavior provides information that complements the findings discussed in previous sections and builds a more complete picture on wake development.

The first part of the analysis focuses on identifying the location and characteristics of the leapfrogging phenomenon, where the vortices interact and exchange positions. Next, the influence of the floating motions cases is investigated. The comparison is conducted using normalized vorticity and swirling strength, which offer a clear picture of the dynamics and vortex strength.

4.4.1. Leapfrogging Location for DTU 10MW Turbine Model

By focusing on the static case, it becomes possible to identify the leapfrogging location for this specific turbine model. The leapfrogging mechanism is recognized as the triggering event that initiates efficient turbulent mixing, which, as demonstrated earlier, marks the onset of the wake re-energizing process. It is important to note that the data from 0.6D to 2.6D consist of three volumes stitched together in post-processing. Due to this, there is no temporal continuity across the full domain, and specific vortices cannot be reliably tracked as discontinuities and time shifted structures appear between volumes.

In Figure 4.25, two coherent vortical structures are tracked using red arrows to illustrate their mutual interaction. The interaction is visualized using the normalized instantaneous swirling strength field ($\lambda D^2/U_\infty^2$). The leading vortex induces a velocity field that accelerates the trailing vortex, drawing it forward. Simultaneously, the trailing vortex exerts a negative velocity on the leading one, slowing it down. As a result of this mutual induction, the vortices begin to exchange positions in both the axial and vertical directions: the first vortex is deflected downward, while the second one is lifted upward. This dynamic interaction causes the vortices to move along helical trajectories, ultimately leading to a leapfrogging event observed around 1.5D downstream of the rotor.

While the same principle applies to the vortices produced by the root of the blade, the intensity is much smaller. Thus, no leapfrogging is seen here.

The image below only represents a single instantaneous capture in time. To ensure that it is not be affected by random big structures in the flow and it is indeed a realistic behavior, other time frames were also analyzed throughout the entire measurement duration. The mean observed leapfrogging location was reaffirmed to be close to 1.5D. This is consistent with the analysis from Figure 4.14 where the XZ component of the Reynolds Stresses as plotted. There, increased momentum transfer begins to occur between 1.5D and 2D, the region now identified as the location where vortex interaction and initial flow mixing take place.

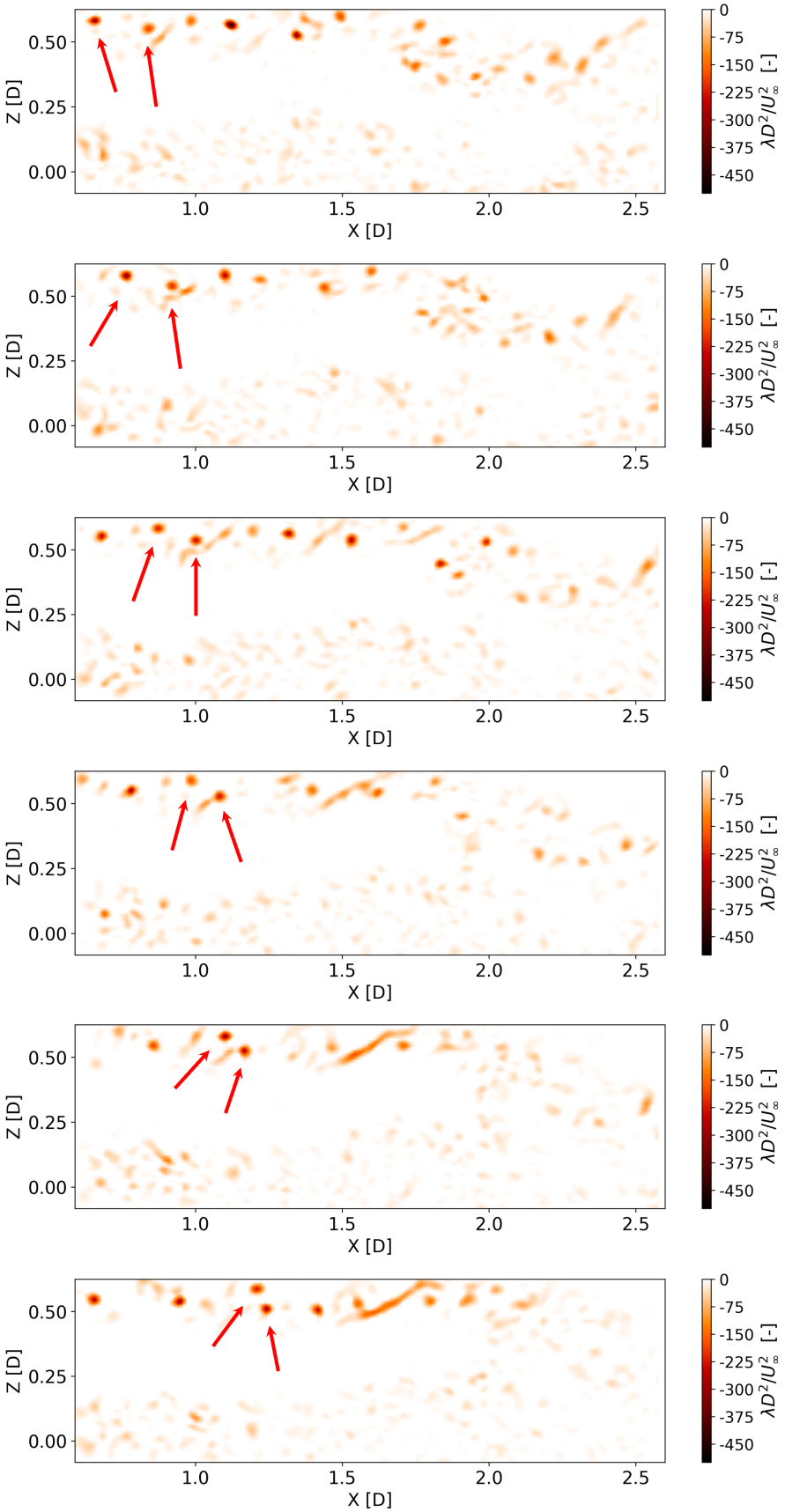

Figure 4.25: Leapfrogging mechanism illustrated by the temporal evolution of two interacting vortices. Swirling strength normalized by the rotor diameter and freestream velocity $\lambda D^2/U_\infty^2$ used to visualize the instantaneous position of the tip vortices.

4.4.2. Influence of FOWT Motions on Vorticity Dynamics

To analyze the vortex structures in the wake, the averaged non-dimensional y-axis vorticity component ω_y is computed, which represents the rotational strength of the flow about the lateral axis. This quantity is defined as:

$$\omega_y = \frac{du}{dz} - \frac{dw}{dx} \tag{4.1}$$

In Figure 4.26, positive values of ω_y (red) correspond to vortices rotating such that, according to the right-hand rule, the vorticity vector points in the positive y direction these are typically associated with root vortices. On the other hand, negative values (blue) indicate rotation in the opposite sense, often representing tip vortices. This analysis is based on the time-averaged vorticity field, so the discontinuities between reconstructed volumes mentioned earlier are irrelevant now.

At first glance, the static case displays a clearly defined and narrow band of negative vorticity near the rotor tip, indicating consistent tip vortex strength and location with low deviation. Around 1.5D downstream, the leapfrogging mechanism begins to disrupt the regular vortex arrangement, resulting in the tip vortex spreading vertically and gradually losing consistency. On the other hand, the root vortex appears as a more diffuse and broader region of positive vorticity since the beginning, which continues to diffuse downstream. By approximately 2.5D, both vortical structures begin to merge and dissipate, and only low vorticity from the tip vortex remains visible afterwards.

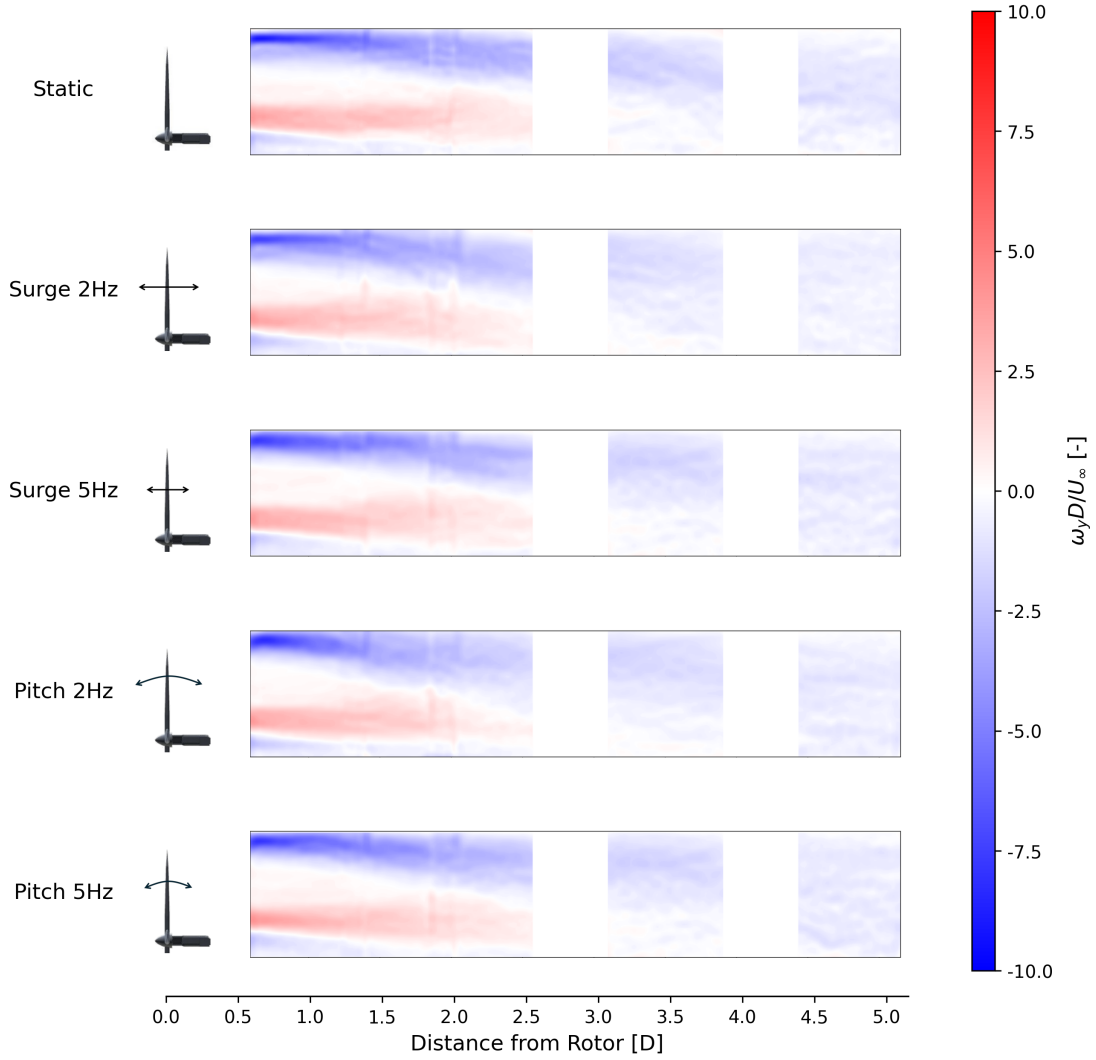

Figure 4.26: Average vorticity along the spanwise axis normalized by the rotor diameter and freestream velocity ($\omega_y D/U_\infty$) for static and motion cases.

When focusing in the motion cases, a clear distinction emerges in the behavior of the tip vortex vorticity compared to the static case. All floating motion scenarios exhibit an immediate and more pronounced diffusion of the tip vortex, characterized by a broader and less concentrated vorticity core. This rapid diffusion is likely produced by the dynamic motion of the platform shifting vortices up and down, reducing the coherence. In contrast, the root vortex remains relatively unaffected in structure and intensity compared to Static. However, it seems to dissipate slightly earlier in the low frequency surge and pitch cases.

A key observation across all motion cases, especially for the low frequency 2Hz pitch and surge, is the earlier interaction and merging of the tip and root vortices, occurring around 1.5D. This is earlier than in the static case, where mixing occurs slightly further downstream. Additionally, reduced vorticity intensity between 2D to 2.5D downstream is observed in the Surge and Pitch 2Hz cases. As it was seen from the R_{XZ} plots there was high momentum transfer and mixing for the 2Hz cases due to the motion of the FOWT. This enhanced vertical mixing appears to accelerate the breakdown of vortex structures, possibly due to the added vertical turbulence.

This breakdown of coherent structures can further validated by visualizing the average swirling strength and focusing in the root and tip vortex. In Figure 4.27 the Davis-produced iso-surfaces for swirling strength, with a threshold of 2.4 $1/s^2$, are presented and colored following normalized ω_y. Only the first three measured volumes are presented as it is where most of the relevant information is condensed.

Here is evident that the strength of the tip vortices is much smaller and spans a smaller distance for 2Hz motions. But on the contrary, the root vortex seems to be amplified, and it stretches for longer than the other cases. The 5Hz motion cases produce more compact tip vortex, particularly in the Pitch 5Hz case, their downstream reach is notably shorter, confirming the quicker dissipation.

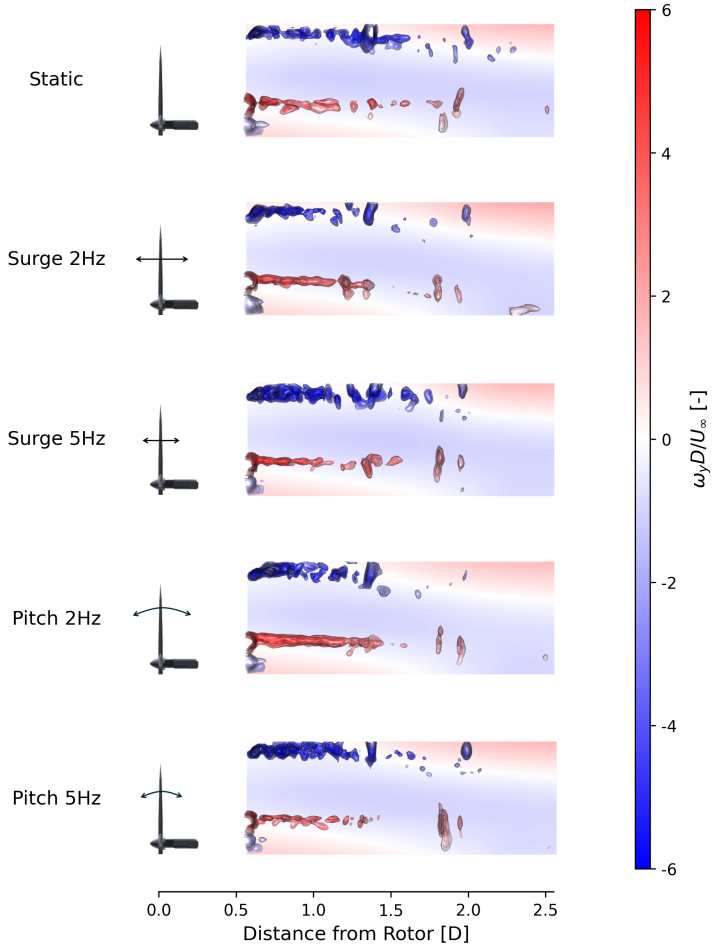

Figure 4.27: Iso-surfaces of swirling strength colored following vorticity along the spanwise axis normalized by the rotor diameter and freestream velocity ($\omega_y D/U_\infty$). Average streamwise velocity is plotted in the background for illustrative purposes.

4.5. Power Spectral Density

Power Spectral Density (PSD) is the measure of signal's power content versus frequency. It is useful to understand how much energy is present in the flow due to the platform motion frequencies.

Mathematically, for a signal $|V|(t)$, the PSD is often estimated via the Fourier Transform:

$$PSD(f) = |\mathcal{F}\{|V|(t)\}|^2 \tag{4.2}$$

Where $\mathcal{F}$ is the Fourier Transform and f is the frequency. The study is performed with the value of Velocity Magnitude $|V|(t)$, so that frequency variations in any of the three components of velocity are considered. The entire frequency domain is then discretized into points known as spectral lines, where the value of PSD is plotted.

Several measurement points in the wake are selected for study locations (Figure 4.28). The spectrum will be shown for both the near wake volumes and the further volumes for two different heights z=0.25D and z=0.6D. This heights are of special interest as they represent a location fully behind the wake of the wind turbine blade, and a location on the edge of the wake respectively. As the wake evolves and dissipates downstream, it is expected that the differences between these heights reduces.

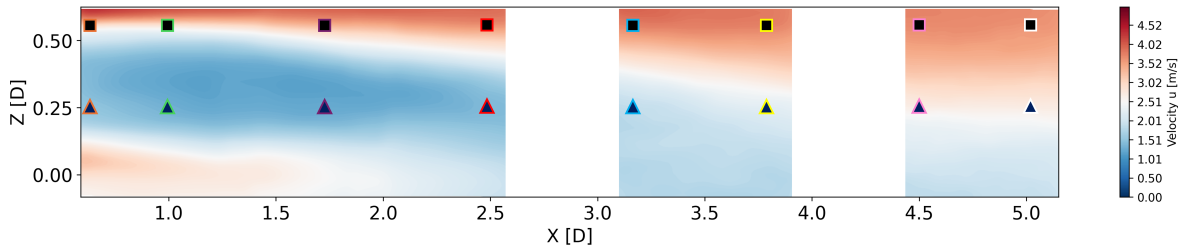

Figure 4.28: Studied locations: Square and Triangle represents heights of 0.6D and 0.25D respectively. Orange, Green, Purple, Red, Blue, Yellow, Pink, & White show the location in x: 0.6D, 1D, 1.75D, 2.5D, 3.25D, 3.75D, 4.5D, & 5D respectively.

The first thing that can be noticed from the set of spectrum below is an increase in low frequency noise occurring as the location of interest moves downstream. This is likely happening due to random fluctuations and oscillations on a higher level, maybe even related to wake meandering.

A clear peak is consistent across all locations: 2Hz. The table below is provided such that the magnitude of the frequency can be comprehended along x and z (See Table 4.2). It becomes evident then that there is an increase in PSD for 2Hz as the wake progresses, reaching its maximum influence around 2.5D before diminishing again. Additionally, Pitch amplitude is highly superior than Surge in most of the selected locations, suggesting that effects of low-frequency sinusoidal pitching motions last longer.

	Location	x = 0.6D	x = 1D	x = 1.75D	x = 2.5D	x = 3.25D	x = 3.75D	x = 4.5D	x = 5D
Surge 2Hz	**z = 0.6D**	18	28	64	280	55	62	17	8
	z = 0.25D	8	27	168	160	100	98	55	28
Pitch 2Hz	**z = 0.6D**	68	171	240	288	105	77	27	12
	z = 0.25D	14	44	142	282	220	180	24	19

Table 4.2: Amplitudes in PSD for Low Frequency Motions $[m^2 s^{-2} Hz^{-1}]$.

On the other hand the higher frequency motions do not seem to influence much the flow after 1D. It is only in Figure 4.29 and Figure 4.30 where peaks at 5Hz are visible, specially on the edge of the very near wake ($z = 0.6D$). In any aft location, the contribution of 5Hz is indistinguishable. In terms of amplitude, Pitch is substantially more intense than Surge: 55 vs 5 PSD respectively for the first location by the edge of the wake.

Near the edge of the wake, the rotation frequency of the blades can be seen distinctively right behind the plane of rotation, specially for the static case. A peak is observed at 8Hz which correspond to the rotating frequency of 480rpm and it is known as 1P. Also at 24Hz a peak is seen which represents the passing of each blade and it is known as 3P frequency. As the focus is shifted downstream, the effect

of the blades slowly dissipates. Looking at Figure 4.32 it is clear that there is no more contribution from the blades, meaning that the near wake is starting to transition to far wake.

In addition, an intense energy peak is observed for 16Hz in this experiment. This frequency was identified as the natural mode of flap-wise vibration corresponding to the blades used in the wind turbine model. Not only the blades are being excited by the low frequency motions (harmonics of 2Hz), but also, the second harmonic of the rotation of the rotor (harmonic of 1P). While there were no consequences during the experimental campaign due to this peak, it is an example of how frequency matching could potentially create unaccounted loads and influence the turbine performance, or even damage the components.

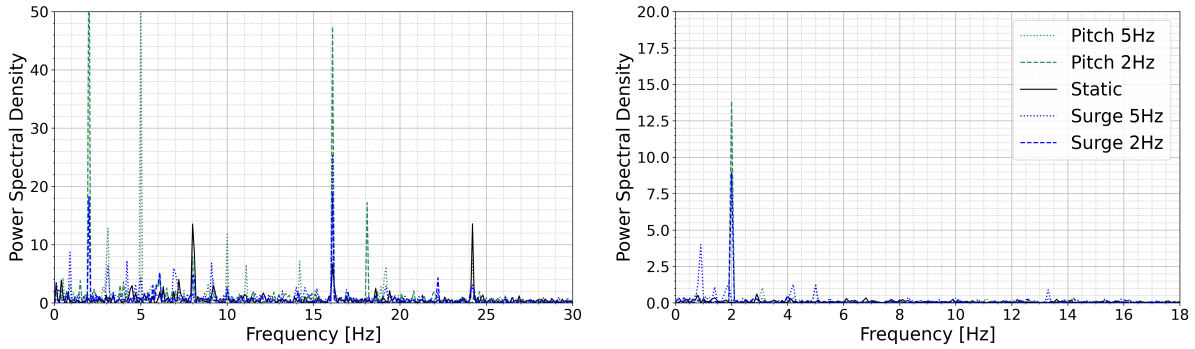

Figure 4.29: PSD at x=0.6D, Left: z=0.6D. Right: z=0.25D

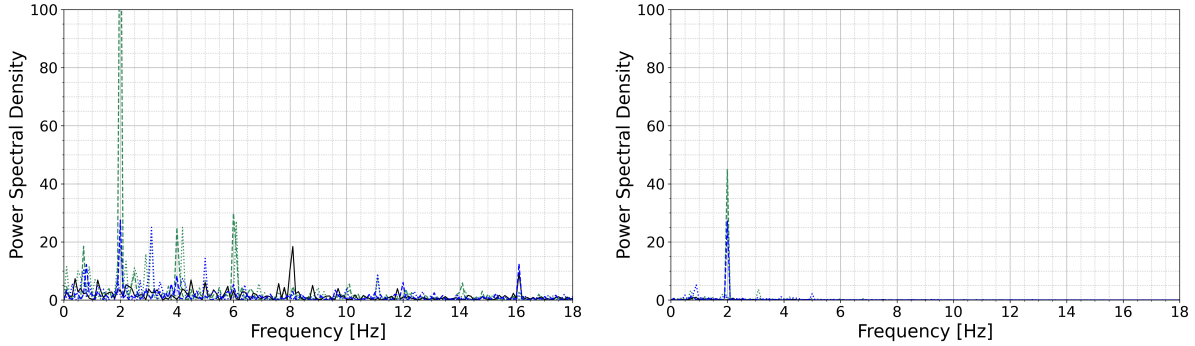

Figure 4.30: PSD at x=1D,Left: z=0.6D. Right: z=0.25D

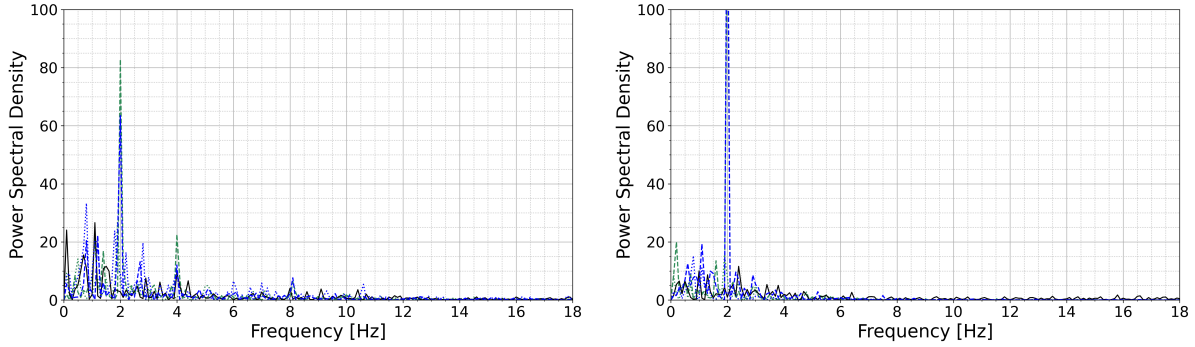

Figure 4.31: PSD at x=1.75D, Left: z=0.6D. Right: z=0.25D

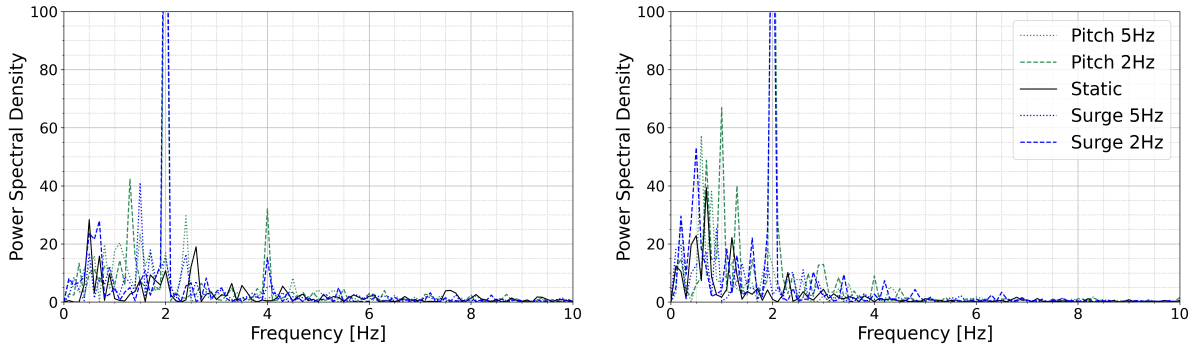

Figure 4.32: PSD at x=2.5D, Left: z=0.6D. Right: z=0.25D

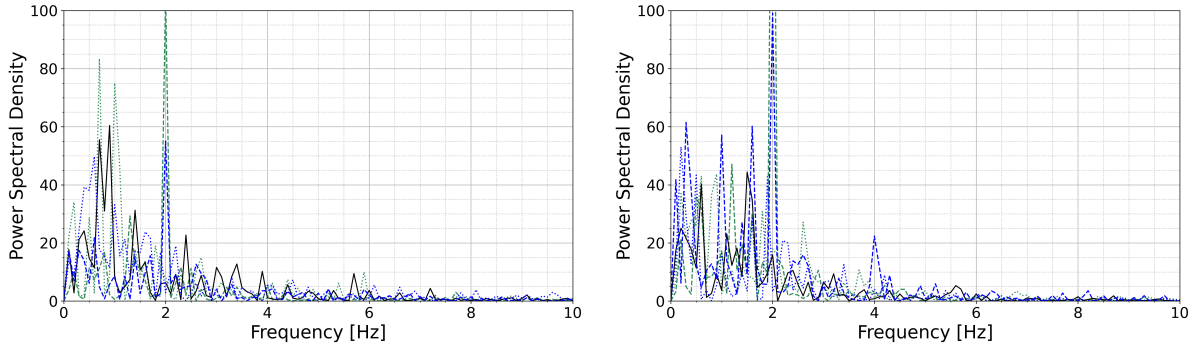

Figure 4.33: PSD at x=3.25D, Left: z=0.6D. Right: z=0.25D

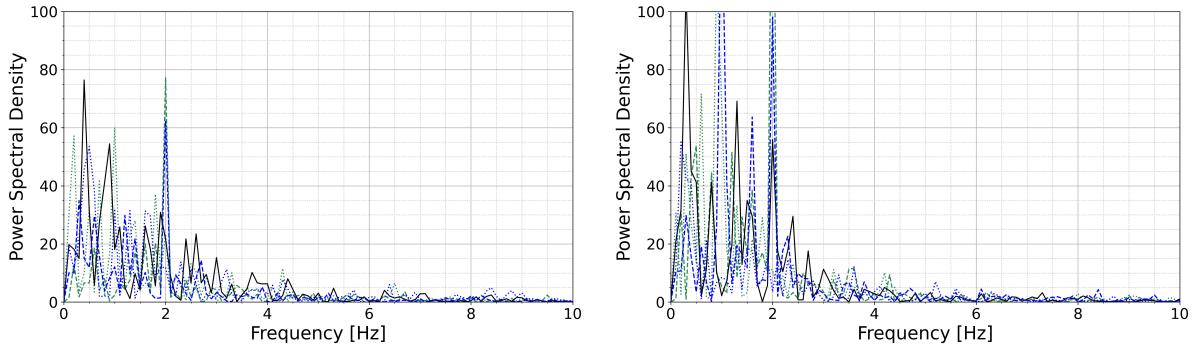

Figure 4.34: PSD at x=3.75D, Left: z=0.6D. Right: z=0.25D

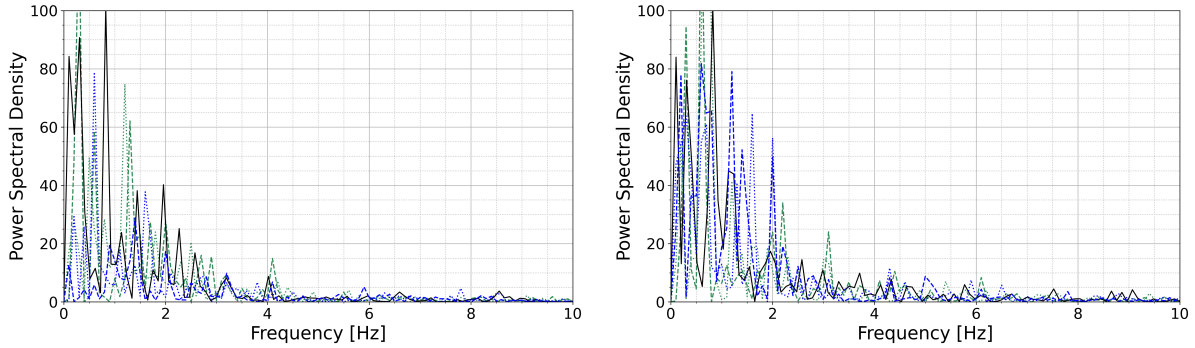

Figure 4.35: PSD at x=4.5D, Left: z=0.6D. Right: z=0.25D

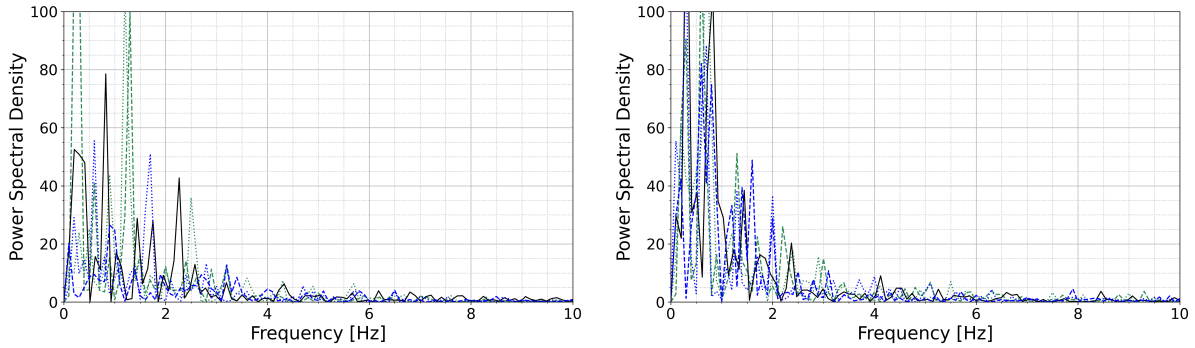

Figure 4.36: PSD at x=5D, Left: z=0.6D. Right: z=0.25D

4.5.1. POD

Proper Orthogonal Decomposition (POD) is a widely used technique for extracting dominant coherent structures from complex flow fields. It allows the decomposition of flow data into spatial modes and associated temporal coefficients, offering a compact and physically meaningful representation of the dynamics. Unlike phase-locked techniques, POD does not require synchronized measurements, making it particularly suitable for analyzing both periodic and random flow fluctuations. By focusing on the frequencies related to the main FOWT motions the impact on the surrounding flow can be interpreted.

POD is performed using the built-in functionality of DaVis, where the flow field is decomposed into a series of spatial modes, each with a corresponding time-dependent coefficient and an associated energy content. The temporal coefficients of the modes are further analyzed using Fast Fourier Transforms (FFT) to identify the dominant frequency. With this, the specific POD modes can be related to the frequencies of interest: $2\mathrm{Hz}$, $5\mathrm{Hz}$, and $8\mathrm{Hz}$ (1P frequency).

To allow meaningful comparisons between different modes, each spatial mode is normalized by the standard deviation of its temporal coefficient ($\sqrt{N_p}$). This normalization is also followed in other studies [82], and ensures that all modes are placed on a consistent physical scale, facilitating visual interpretation of their relative strength and contribution to velocity fluctuations.

In the results presented below (Figure 4.37), the modes corresponding to the frequencies of interest are shown. While these modes capture the dominant spatial structures linked to each frequency, they do not represent the full effect: additional contributions from harmonics and other phase-related modes enhance and counteract the flow behavior. Nevertheless, these plots show the biggest influence on the flow field by showing the most energetic mode for each frequency. Note the distinct difference in velocity range between the $2\mathrm{Hz}$ cases and the higher frequency ones.

$2\mathrm{Hz}$ motions influence the flow considerably. In a single mode it is seen how the influence of both surge and pitch almost reaches $\pm 5\mathrm{m/s}$. The cycles are clearly distinguishable in the flow, with the positive and negative contributions repeating every 0.8-0.9D. The energy content of Pitch is the highest, representing 20% of the total flow energy in this single mode, while the maximum energy Surge mode is 18% of the total flow.

$5\mathrm{Hz}$ frequencies are not as energetic as the low frequency ones. They are no longer the driving influencing factor in the flow, the first influence from $5\mathrm{Hz}$ is found in the 7^{th} mode for both Surge and Pitch (green dot in the energy content graph). This means that other oscillations or random structures have more effect in the flow than the prescribed motion. Focusing at the plot, the influence of $5\mathrm{Hz}$ is seen mostly around the tip of the blade rather than the entire domain as seen before. The effect is clearly lower, influencing only $\pm 1\mathrm{m/s}$ in this region.

To observe the first contribution of the $8\mathrm{Hz}$ component to the energy content, one must refer to the 17^{th} mode. The effect is rather small, representing around 1% of the total energy content, and influencing the flow only around $\pm 0.6\mathrm{m/s}$. It is important to note that this corresponds to the static case, where no other dominant frequency components are present. In cases with significant $2\mathrm{Hz}$ motion, and to a lesser extent $5\mathrm{Hz}$, the influence of the 1P frequency is expected to be even smaller due to the overshadowing effect of these more energetic motions

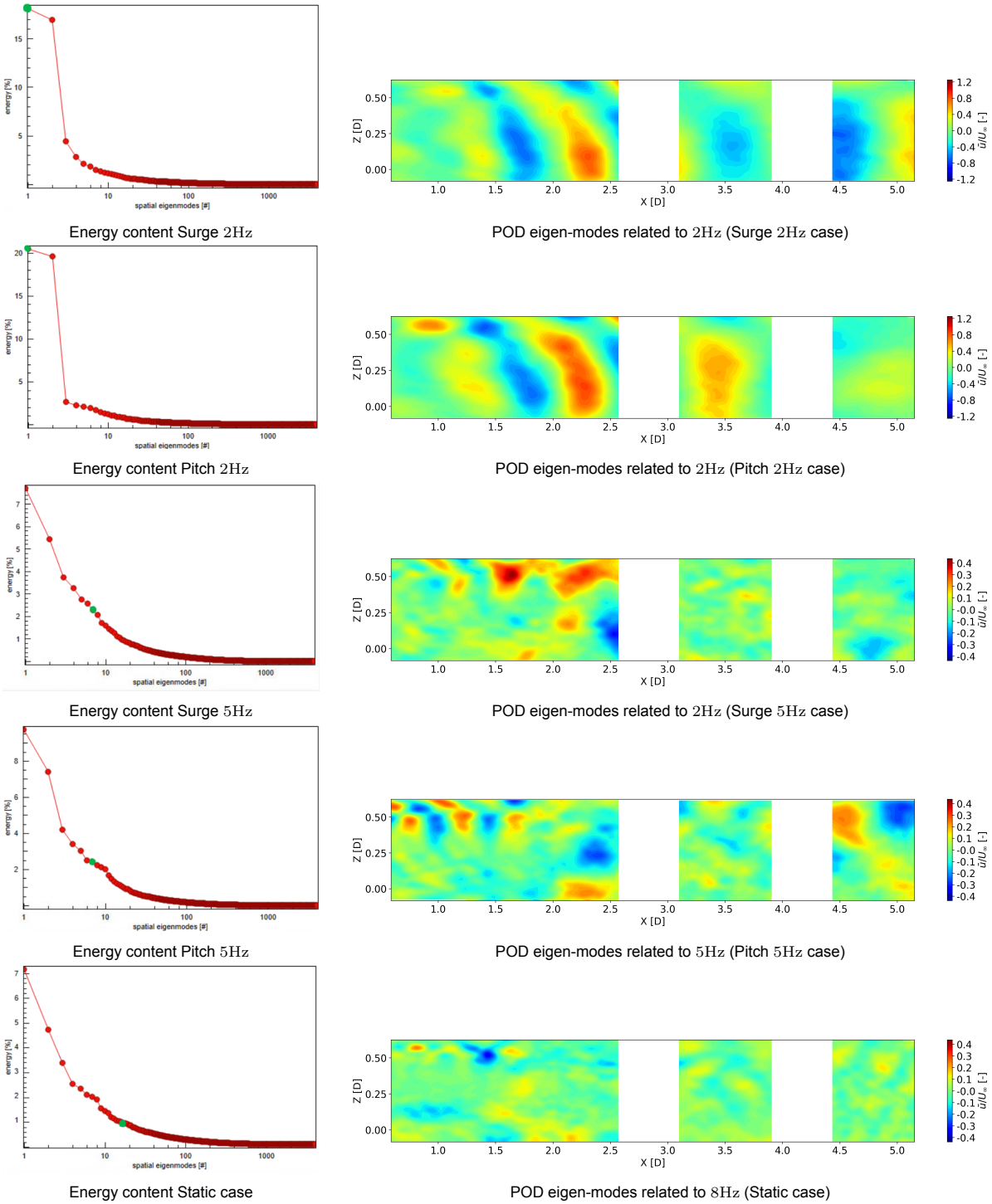

Energy content Surge $2\mathrm{Hz}$ | POD eigen-modes related to $2\mathrm{Hz}$ (Surge $2\mathrm{Hz}$ case)

Energy content Pitch $2\mathrm{Hz}$ | POD eigen-modes related to $2\mathrm{Hz}$ (Pitch $2\mathrm{Hz}$ case)

Energy content Surge $5\mathrm{Hz}$ | POD eigen-modes related to $2\mathrm{Hz}$ (Surge $5\mathrm{Hz}$ case)

Energy content Pitch $5\mathrm{Hz}$ | POD eigen-modes related to $5\mathrm{Hz}$ (Pitch $5\mathrm{Hz}$ case)

Energy content Static case | POD eigen-modes related to $8\mathrm{Hz}$ (Static case)

Figure 4.37: POD spatial modes associated with dominant frequencies (note color-bar range is different for $2\mathrm{Hz}$ motions).

4.6. Uncertainties

Lavision states that sub-pixel displacement measurement accuracy is maximized by sophisticated interpolations and routines [83]. However, not all errors can be prevented, and measurement uncertainties from all the experimental and processing parameters must be quantified.

To assess the reliability of the measured flow fields, two primary sources of uncertainty were considered: the uncertainty arising from the stereo camera calibration, and the uncertainty associated with velocity field reconstruction via VIC+ in Davis.

The first source arises from the 3D reconstruction of particle positions, based on the stereo camera calibration. The average residual calibration error was found to be 0.00605 pixel, approximately 0.005 mm. To translate this into a velocity uncertainty, the following relation was used:

$$\delta u = \frac{\delta x}{\Delta t} \tag{4.3}$$

Where δx is the spatial uncertainty obtained from DaVis, and Δt is the time between frames (0.0025s). This constitutes the baseline uncertainty from position measurements alone, and results to 0.002 m/s.

A second component of uncertainty arises from the velocity calculation and fitting during the VIC+ processing. In this phase, the instantaneous particles are tracked and used to reconstruct a continuous velocity field by forward and backward integration in time. Inconsistent number of particles, or local seeding density can influence in error production. Davis is able to quantify uncertainty for instantaneous velocity vectors, for both 2D and 3D techniques, employing a method based on correlation statistics.

While the above two sources of uncertainty are treated separately, their combined effect contributes to the total uncertainty in the measured velocity field. The propagation of uncertainty is additive following root-mean-square:

$$\delta u_{total} = \sqrt{(\frac{\delta x}{\Delta t})^2 + \delta u_{VIC}^2} \tag{4.4}$$

For visualization purposes, uncertainty maps were generated along the measured wake to highlight regions of higher measurement error. No distinction is made between surge and pitch, only between low frequency and high frequency motions compared to the static (Figure 4.38). Additionally, the uncertainty for the phase-locked flow fields is presented to evaluate the impact of reduced sample sizes on the reliability of the averaged results (Figure 4.39).

In practice, the total uncertainty is found to increase with downstream distance in the wake. This trend is attributed to more complex flow structures unrelated directly to the motions for the FOWT model. The most accurate velocity estimations are obtained close to the rotor, with error estimated around 0.01 m/s. At a distance of 5D uncertainties have increased by a factor of 10, independently on the case. The line correspondent to $2\mathrm{Hz}$ *Phase-Locked Motion* is clearly more unstable and unpredictable than $5\mathrm{Hz}$ or Static, presenting higher values of uncertainty specially between 2D and 4.5D.

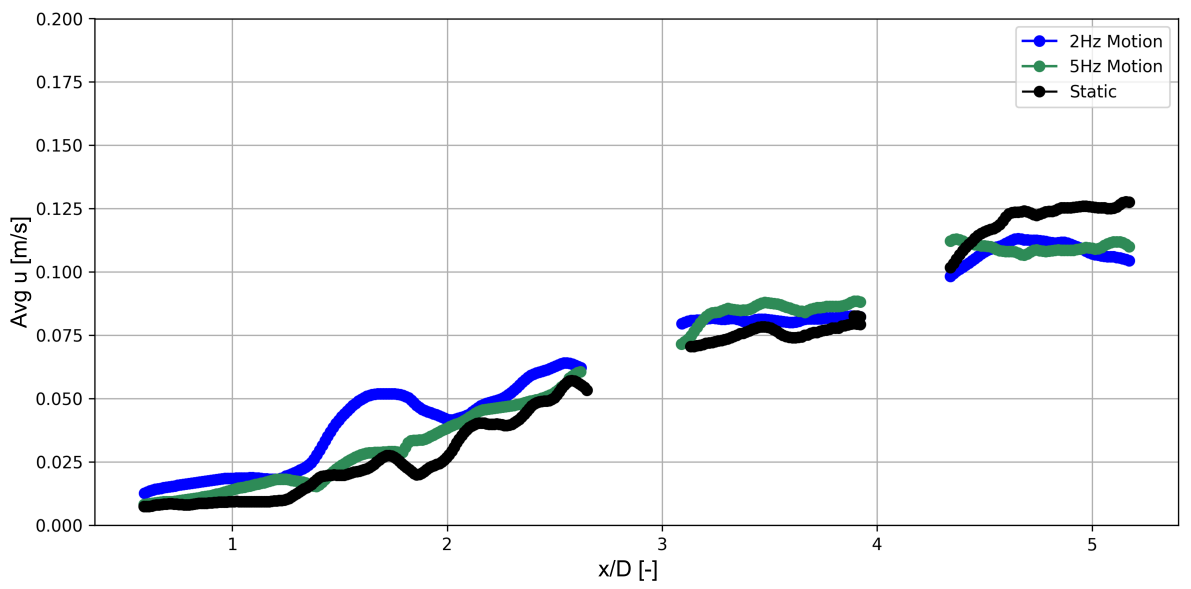

Figure 4.38: Uncertainties along the wake for different cases, based on unconditional averaging of the full dataset.

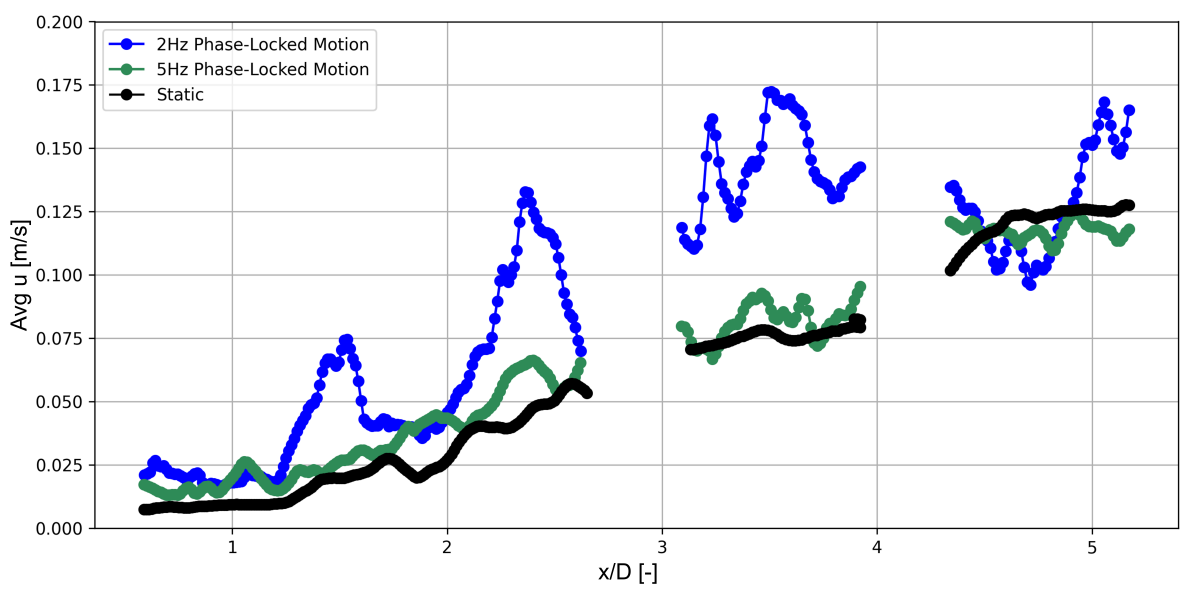

Figure 4.39: Uncertainties along the wake for different cases, based on phase-locked averaging for the studied frequencies.

5

Conclusion

An experiment campaign involving the aerodynamic testing of a scaled wind turbine model moving on a 6-DOF hexapod in the Open Jet Facility at Delft University of Technology was performed. Flow field measurements and wake characterization are conducted using 3D PTV with HFSB tracers, capturing four times the size of previous related work through multiple traversing system movements. The insights gained from this investigation aim to contribute valuable knowledge to the global research community on FOWTs and support the ongoing development and optimization of future floating offshore wind farms.

This study demonstrates that the motions of floating offshore wind turbines, particularly low-frequency oscillations, play a significant role in shaping the downstream wake characteristics. Based on the analysis and findings, the research questions will be answered here, providing the key conclusions drawn from this investigation:

RQ I. How do floating motions affect the wake characteristics of a FOWT?

While the imposed floating motions do not change the wake expansion ratio or the location where blade effects disappear (end of near-wake region), 20% and 4D respectively, they introduce velocity oscillations which are not seen in the static case.

The periodic nature of the motion is clearly reflected in the phase-locked averaged horizontal and vertical velocity fields, forming distinct regions of alternating influence. These effects are particularly pronounced in the near wake, with fluctuations peaking around 2.5D downstream and reaching up to approximately 20% of the freestream velocity. The induced horizontal and vertical flow structures enhance mixing within the wake, leading to an earlier increase in TI compared to the static case and promoting higher velocities in previously low-speed regions.

Ia. How do low- and high-frequency motions differently influence the wake behavior of a floating offshore wind turbine?

Low-frequency motions exhibit a broader and earlier influence on the wake, accelerating its development and enhancing turbulent mixing up to approximately 3D downstream. In contrast, while high-frequency effects are still detectable in phase-locked analyses, the overall wake behavior closely resembles that of the static case.

Turbulence intensity further highlights the limited mixing in high-frequency cases. For 2Hz motions, horizontal and vertical velocity fluctuations reach up to $\pm$0.75m/s and $\pm$1.1m/s respectively. In comparison, 5Hz motions show much lower fluctuations, approximately $\pm$0.3m/s horizontally and $\pm$0.4m/s vertically, indicating weaker wake perturbations and slower development.

Ib. How does the wake differ when the FOWT exhibits pitching versus surging sinusoidal motions?

While the affected regions and behavior are very similar from pitch to surge, the intensity of fluctuations seem to be higher for the surge case, leading to higher average velocities in the more downstream volumes. When focusing at the last measured location, the streamwise velocity of surge cases was 20% better than the respective pitch case. The rate of improvement is similar through the entire measured domain, suggesting that the same development could happen beyond 5D.

RQ II. How does wake recovery change with FOWT motions compared to a stationary turbine?

Motions are able to force free-stream flow to bend downwards behind the wake of the wind turbine unlike the static case. Motions show fluctuations in vertical velocity near the edge of the wake, alternating between upward and downward trends. These flow movements show an increase in momentum transfer from outside of the wake, mixing further the shear layer, re-energizing the center of the wake, and increasing the horizontal velocity.

This was further verified with TI plots where more turbulence was observed in the near wake of the motion cases, but less than Static in the last measured volumes (5D downstream of rotor). This suggests that the imposed motion in FOWTs could accelerate wake development by approximately two to three diameters, improving wake recovery considerably. Assuming a similar recovery rate beyond the measured domain, this early wake evolution could offer significant advantage over the static configuration.

IIa. Which motion modes and amplitudes result in the most significant changes in wake recovery?

Overall, lower-frequency motions offer a considerable improvement in wake recovery. Among the motion types, surge results in more favorable outcomes than pitch. Furthermore, larger motion amplitudes generally lead to improved performance compared to smaller amplitudes.

Surge 2Hz outperforms every other case. Velocity deficit line plots show the best results for all distances, and around 40% better recovery than Static in the last measured volume.

The Pitch 2Hz and Surge 5Hz cases follow, each demonstrating approximately a 20% improvement in wake recovery compared to the static case. Notably, the Pitch 2Hz case characterized with lower amplitude, shows comparable velocity curves to the higher amplitude case within the only tested volume, located around 3.5D downstream.

In contrast, the remaining cases show minimal improvement over the static case. Only Pitch 5Hz exhibits slightly better recovery, and only at the furthest measured distance.

IIb. Does imposing a realistic wave-induced motion pattern lead to enhanced wake mixing compared to simplified sinusoidal motions?

Within the two wave cases, the rough sea state does not show much improvement, showing the slowest wake streamwise velocity of all tested cases. The moderate sea state also does not perform greatly, matching velocity profile with Static, even being slightly slower near the wake boundary.

However, the moderate wave velocity deficit line matches almost to perfection the line of Surge 5Hz for the one volume measured, also great match seen in TI. This is of great importance, as a moderate sea state can now be related to a sinusoidal imposed motion tested for the entire domain. Thus, assuming that the behavior remains similar for the later volumes, better wake recovery, up to 20% better than Static, is realistic for FOWTs.

5.1. Recommendations

The following recommendations aim to guide future work by addressing experimental limitations, extending the current findings, and proposing complementary studies to enhance understanding and applicability.

- **Improved correlation between wave cases and sinusoidal imposed motions**
  In this study, one of the main conclusions is that a moderate sea state wake can be reproduced by a simple sinusoidal 5Hz Surge motion with $\Delta V^* = 0.1$. This was only verified in a single volume location, only place where waves were tested.

  It is recommended to assess this behavior at additional downstream locations. If the 5Hz surge motion reliably replicates a moderate sea state, it could greatly simplify experimental setups, as only a 1DOF system would be required.

  Alternatively, another approach would be to actively try and find a frequency and amplitude that show the same results as moderate or rough wave patterns.

- **Measurements at further downstream locations** While this study indicates that FOWT motion can enhance wake recovery, further measurements at greater downstream distances are needed. In wind farms, turbines typically operate in the far wake, at distances of approximately 10–15D downstream.

  It is therefore essential to validate the observed trends at those distances. Including a moderate wave case in such experiments would also help simulate more realistic operational conditions.

  The current setup is limited by the quality of the flow further downstream, as well as the physical length of the test section. However, the wind turbine model was placed $3.1\mathrm{m}$ away from the nozzle due to safety concerns. By addressing the safety constraints, the setup can instantly gain more than 2D in length.

- **Investigation of persistent negative vertical velocity**
  A consistent negative vertical velocity was observed across the entire domain, which remains unexplained. Understanding the root cause of this anomaly is important for future experiments and should be documented to assist other researchers working in the same facility.

- **Bigger 3D PTV measurement volumes**
  Larger measurement volumes could be achieved by repositioning the cameras about $0.5\mathrm{m}$ farther from the wake center (toward the OJF wall), and using $50\mathrm{mm}$ lenses on all cameras to expand the field of view in the streamwise and vertical directions. This could increase coverage by roughly $0.4\mathrm{m}$ in each direction.

  A larger volume simplifies the testing inside the wind tunnel. Measuring the same locations can be achieved with less traversing movements, reducing the number of tests. Additionally, the full rotor diameter could be covered, adding information in the characterization of the wake. Or alternatively, a bigger portion of the shear layer, between slow velocity wake and the high velocity freestream could be studied, focusing on the gradient curve between the two regions.

  However, these changes would require setup optimization and potentially a different HFSB seeder or seeding strategy, as vertical seeding range was already a limitation in the current experiment. Additionally, processing such a large volume may exceed Davis' current post-processing capacity.

- **Verification and completeness through numerical studies**
  Two numerical studies are currently being developed in other studies, trying to specifically reproduce the experimental test presented in this thesis.

  If they succeed, coupling experimental validation with numerical modeling would enhance the robustness of the findings and support a deeper understanding of the flow behavior. Furthermore they would offer a cost-effective way to explore scenarios beyond the experimental matrix.

- **Incorporating blade position tracking for blade-phase-locking**
  Although not directly relevant to wake recovery, monitoring blade position for blade-phase-locking could uncover subtle mechanisms in the near wake. This additional insight may prove valuable for a deeper understanding of wake dynamics.

References

[1] World Weather Attribution. *World Weather Attribution*. Accessed: 23 June 2025. 2024. URL: https://www.worldweatherattribution.org/.

[2] A. Stips et al. “On the causal structure between CO_2 and global temperature”. In: *Scientific Reports* 6 (2016), p. 21691. DOI: 10.1038/srep21691. URL: https://doi.org/10.1038/srep21691.

[3] United Nations Framework Convention on Climate Change. *Paris Agreement*. https://unfccc.int/process-and-meetings/the-paris-agreement/the-paris-agreement. Accessed: 2025-06-23. 2015.

[4] IPCC. *Climate Change 2023: Synthesis Report. Contribution of Working Groups I, II and III to the Sixth Assessment Report of the Intergovernmental Panel on Climate Change*. https://www.ipcc.ch/report/ar6/syr/. Accessed: 2025-06-23. 2023.

[5] Kristina Eurek et al. “An improved global wind resource estimate for integrated assessment models”. In: *Energy Economics* 64 (2017), pp. 552–567. DOI: 10.1016/j.eneco.2016.11.015.

[6] International Energy Agency. *World Energy Outlook 2022*. https://www.iea.org/reports/world-energy-outlook-2022. Accessed: 2025-06-23. 2022.

[7] S.P. Hendriks. “Analysis of the Wake of Tandem Floating Wind Turbines”. Flow Physics and Technology, Wind Energy - Aerospace Engineering. MA thesis. TU Delft, Faculty of Aerospace Engineering, 2024.

[8] James F. Manwell, Jon G. McGowan, and Anthony L. Rogers. *Wind Energy Explained: Theory, Design and Application*. 2nd. Chichester, UK: Wiley, 2009. ISBN: 978-0-470-01500-1.

[9] Global Wind Energy Council. *Global Offshore Wind Report 2022*. Published by the Global Wind Energy Council, Brussels, Belgium. June 2022. URL: https://gwec.net.

[10] Emma C. Edwards et al. “Evolution of floating offshore wind platforms: A review of at-sea devices”. In: *Renewable and Sustainable Energy Reviews* 183 (2023), p. 113416. ISSN: 1364-0321. DOI: https://doi.org/10.1016/j.rser.2023.113416. URL: https://www.sciencedirect.com/science/article/pii/S1364032123002733.

[11] Srikanth Bashetty and Selahattin Ozcelik. “Review on Dynamics of Offshore Floating Wind Turbine Platforms”. In: *Energies* 14.19 (2021). ISSN: 1996-1073. DOI: 10.3390/en14196026. URL: https://www.mdpi.com/1996-1073/14/19/6026.

[12] Emma C. Edwards et al. “Trends in floating offshore wind platforms: A review of early-stage devices”. In: *Renewable and Sustainable Energy Reviews* 193 (2024), p. 114271. ISSN: 1364-0321. DOI: https://doi.org/10.1016/j.rser.2023.114271. URL: https://www.sciencedirect.com/science/article/pii/S1364032123011292.

[13] T.J. Broertjes. “Lift-Induced Wake Re-Energization for a VAWT-Based Multi-Rotor System”. MA thesis. Delft University of Technology, 2024.

[14] L. Pustina et al. “Control of power generated by a floating offshore wind turbine perturbed by sea waves”. In: *Renewable and Sustainable Energy Reviews* 132 (2020), p. 109984. ISSN: 1364-0321. DOI: https://doi.org/10.1016/j.rser.2020.109984. URL: https://www.sciencedirect.com/science/article/pii/S1364032120302756.

[15] Yan Li et al. “Effects of various freak waves on dynamic responses of a Spar-buoy floating offshore wind turbine”. In: *Ocean Engineering* 311 (2024), p. 118837. ISSN: 0029-8018. DOI: https://doi.org/10.1016/j.oceaneng.2024.118837. URL: https://www.sciencedirect.com/science/article/pii/S0029801824021759.

[16] Nicolas Coudou, Sophia Buckingham, and Jeroen Beeck. “Experimental study on the wind-turbine wake meandering inside a scale model wind farm placed in an atmospheric-boundary-layer wind tunnel”. In: *Journal of Physics: Conference Series* 854 (May 2017), p. 012008. DOI: 10.1088/1742-6596/854/1/012008.

[17] Lei Xue et al. “Wake Interactions of Two Tandem Semisubmersible Floating Offshore Wind Turbines Based on FAST.Farm”. In: *Journal of Marine Science and Engineering* 10 (Dec. 2022), p. 1962. DOI: 10.3390/jmse10121962.

[18] Bjørn Skaare et al. “Integrated dynamic analysis of floating offshore wind turbines”. In: *European Wind Energy Conference and Exhibition* (Jan. 2007).

[19] F. Taruffi, F. Novais, and A. Viré. “An experimental study on the aerodynamic loads of a floating offshore wind turbine under imposed motions”. In: *Wind Energy Science* 9.2 (2024), pp. 343–358. DOI: 10.5194/wes-9-343-2024. URL: https://wes.copernicus.org/articles/9/343/2024/.

[20] Xinbao Wang et al. “A review of aerodynamic and wake characteristics of floating offshore wind turbines”. In: *Renewable and Sustainable Energy Reviews* 175 (2023), p. 113144. ISSN: 1364-0321. DOI: https://doi.org/10.1016/j.rser.2022.113144. URL: https://www.sciencedirect.com/science/article/pii/S1364032122010255.

[21] Ziwen Chen, Xiaodong Wang, and Shun Kang. “Effect of the Coupled Pitch–Yaw Motion on the Unsteady Aerodynamic Performance and Structural Response of a Floating Offshore Wind Turbine”. In: *Processes* 9 (Feb. 2021), p. 290. DOI: 10.3390/pr9020290.

[22] Richard Stevens, Dennice Gayme, and Charles Meneveau. “Effects of turbine spacing on the power output of extended wind-farms”. In: *Wind Energy* 19 (Feb. 2015). DOI: 10.1002/we.1835.

[23] Stefano Gambuzza and Bharathram Ganapathisubramani. “The influence of free stream turbulence on the development of a wind turbine wake”. In: *Journal of Fluid Mechanics* 963 (2023), A19. DOI: 10.1017/jfm.2023.302.

[24] Lei Duan et al. “Wake topology and energy recovery in floating horizontal-axis wind turbines with harmonic surge motion”. In: *Energy* 260 (2022), p. 124907. ISSN: 0360-5442. DOI: https://doi.org/10.1016/j.energy.2022.124907. URL: https://www.sciencedirect.com/science/article/pii/S0360544222018096.

[25] N. Kluth, Krzysztof Rudion, and Antje Orths. *Study of wake effects for offshore wind farm planning*. Oct. 2010.

[26] P. Veers et al. “Grand challenges in the design, manufacture, and operation of future wind turbine systems”. In: *Wind Energy Science* 8.7 (2023), pp. 1071–1131. DOI: 10.5194/wes-8-1071-2023. URL: https://wes.copernicus.org/articles/8/1071/2023/.

[27] Nord-Jan Vermeer, Jens Sørensen, and Antonio Crespo. “Wind turbine wake aerodynamics”. In: *Progress in Aerospace Sciences - PROG AEROSP SCI* 39 (Oct. 2003), pp. 467–510. DOI: 10.1016/S0376-0421(03)00078-2.

[28] Magnus K. Vinnes et al. “The far wake of porous disks and a model wind turbine: Similarities and differences assessed by hot-wire anemometry”. In: *Journal of Renewable and Sustainable Energy* 14.2 (Mar. 2022), p. 023304. DOI: 10.1063/5.0074218. URL: https://doi.org/10.1063/5.0074218.

[29] Alexander Piqué, Mark Miller, and Marcus Hultmark. “Laboratory investigation of the near and intermediate wake of a wind turbine at very high Reynolds numbers”. In: *Experiments in Fluids* 63 (June 2022). DOI: 10.1007/s00348-022-03455-0.

[30] Eduardo Alvarez and Andrew Ning. *Reviving the Vortex Particle Method: A Stable Formulation for Meshless Large Eddy Simulation*. June 2022. DOI: 10.48550/arXiv.2206.03658.

[31] L.E.M. Lignarolo et al. “Experimental analysis of the wake of a horizontal-axis wind-turbine model”. In: *Renewable Energy* 70 (2014). Special issue on aerodynamics of offshore wind energy systems and wakes, pp. 31–46. ISSN: 0960-1481. DOI: https://doi.org/10.1016/j.renene.2014.01.020. URL: https://www.sciencedirect.com/science/article/pii/S0960148114000494.

[32] S. Ivanell et al. “Stability Analysis of the Tip Vortices of a Wind Turbine”. In: *Wind Energy* 13 (Jan. 2008), pp. 705–715. DOI: 10.1002/we.391.

[33] Alessandro Fontanella et al. “UNAFLOW: a holistic wind tunnel experiment about the aerodynamic response of floating wind turbines under imposed surge motion”. In: *Wind Energy Science* 6 (Sept. 2021), pp. 1169–1190. DOI: 10.5194/wes-6-1169-2021.

[34] Stanislav Rockel et al. “Wake to wake interaction of floating wind turbine models in free pitch motion: An eddy viscosity and mixing length approach”. In: *Renewable Energy* 85 (Jan. 2016), pp. 666–676. DOI: 10.1016/j.renene.2015.07.012.

[35] D.C. van der Hoek. “Advances in Actuation Techniques for Wind Farm Flow Control”. PhD thesis. TU Delft, Team Jan-Willem van Wingerden - Mechanical, Maritime and Materials Engineering, 2023. DOI: 10.4233/uuid:56cadf8e-cc7f-4f7b-b6b0-696dd4ecb65d. URL: https://doi.org/10.4233/uuid:56cadf8e-cc7f-4f7b-b6b0-696dd4ecb65d.

[36] Thomas Messmer, Michael Hölling, and Joachim Peinke. “Enhanced recovery caused by nonlinear dynamics in the wake of a floating offshore wind turbine”. In: *Journal of Fluid Mechanics* 984 (Apr. 2024). DOI: 10.1017/jfm.2024.175.

[37] Fawaz Massouh and Ivan Dobrev. “Exploration of the vortex wake behind a wind turbine rotor”. In: *Journal of Physics: Conference Series* 75 (Aug. 2007), p. 012036. DOI: 10.1088/1742-6596/75/1/012036.

[38] F. González-Longatt, P. Wall, and V. Terzija. “Wake effect in wind farm performance: Steady-state and dynamic behavior”. In: *Renewable Energy* 39.1 (2012), pp. 329–338. ISSN: 0960-1481. DOI: https://doi.org/10.1016/j.renene.2011.08.053. URL: https://www.sciencedirect.com/science/article/pii/S0960148111005155.

[39] Jinlong He et al. “Coupled Aero–Hydrodynamic Analysis in Floating Offshore Wind Turbines: A Review of Numerical and Experimental Methodologies”. In: *Journal of Marine Science and Engineering* 12 (Dec. 2024), p. 2205. DOI: 10.3390/jmse12122205.

[40] Steven Rodriguez and Justin Jaworski. “Strongly-coupled aeroelastic free-vortex wake framework for floating offshore wind turbine rotors. Part 1: Numerical framework”. In: *Renewable Energy* 141 (Apr. 2019), pp. 1127–1145. DOI: 10.1016/j.renene.2019.04.019.

[41] Steven Rodriguez and Justin Jaworski. “Strongly-coupled aeroelastic free-vortex wake framework for floating offshore wind turbine rotors. Part 2: Application”. In: *Renewable Energy* 149 (Oct. 2019), pp. 1018–1032. DOI: 10.1016/j.renene.2019.10.094.

[42] Néstor Ramos-García et al. “Investigation of the floating IEA Wind 15 MW RWT using vortex methods Part I: Flow regimes and wake recovery”. In: *Wind Energy* 25 (Oct. 2021). DOI: 10.1002/we.2682.

[43] Zhaobin Li and Xiaolei Yang. “Resolvent-based motion-to-wake modelling of wind turbine wakes under dynamic rotor motion”. In: *Journal of Fluid Mechanics* 980 (Feb. 2024), p. 48. DOI: 10.1017/jfm.2023.1097.

[44] Benyamin Schliffke, Sandrine Aubrun, and Boris Conan. “Wind Tunnel Study of a “Floating” Wind Turbine’s Wake in an Atmospheric Boundary Layer with Imposed Characteristic Surge Motion”. In: *Journal of Physics: Conference Series* 1618 (Sept. 2020), p. 062015. DOI: 10.1088/1742-6596/1618/6/062015.

[45] Ilmas Bayati et al. “Wind Tunnel Wake Measurements of Floating Offshore Wind Turbines”. In: *Energy Procedia* 137 (Oct. 2017), pp. 214–222. DOI: 10.1016/j.egypro.2017.10.375.

[46] Ilmas Bayati et al. “Wind tunnel validation of AeroDyn within LIFES50+ project: imposed Surge and Pitch tests”. In: *Journal of Physics Conference Series* 753 (Oct. 2016). DOI: 10.1088/1742-6596/753/9/092001.

[47] Ilmas Bayati, BELLOLI M., and Alan Facchinetti. “Wind Tunnel Tests on Floating Offshore Wind Turbines: A Proposal for Hardware-in-the-Loop Approach to Validate Numerical Codes”. In: *Wind Engineering* 37 (Dec. 2013), pp. 1–8. DOI: 10.1260/0309-524X.37.6.557.

[48] M. Belloli et al. “A hybrid methodology for wind tunnel testing of floating offshore wind turbines”. In: *Ocean Engineering* 210 (Aug. 2020), p. 107592. DOI: 10.1016/j.oceaneng.2020.107592.

[49] Hui Hu, Morteza Khosravi, and P. Sarkar. “An Experimental Investigation on the Performance and the Wake Characteristics of a Wind Turbine Subjected to Surge Motion”. In: Jan. 2015. DOI: 10.2514/6.2015-1207.

[50] YuanTso Li, Wei yu, and Hamid Sarlak. “Wake Structures and Performance of Wind Turbine Rotor With Harmonic Surging Motions Under Laminar and Turbulent Inflows”. In: *Wind Energy* 27 (Oct. 2024), pp. 1499–1525. DOI: 10.1002/we.2949.

[51] Ping Zhang et al. “Three-dimensional analytical wake model for floating offshore wind turbines under pitch motion”. In: *Ocean Engineering* 311 (2024), p. 118935. ISSN: 0029-8018. DOI: https://doi.org/10.1016/j.oceaneng.2024.118935. URL: https://www.sciencedirect.com/science/article/pii/S002980182402273X.

[52] Stanislav Rockel et al. “Experimental Study on Influence of Pitch Motion on the Wake of a Floating Wind Turbine Model”. In: *Energies* 7 (Apr. 2014), pp. 1954–1985. DOI: 10.3390/en7041954.

[53] Philippe Chatelain et al. “Large Eddy Simulation of Wind Turbine Wakes”. In: *Flow, Turbulence and Combustion* 91.3 (2013), pp. 587–605. DOI: 10.1007/s10494-013-9474-8. URL: https://doi.org/10.1007/s10494-013-9474-8.

[54] Zhaobin Li, Yunliang Li, and Xiaolei Yang. “Large eddy simulation and linear stability analysis of active sway control for wind turbine array wake”. In: *Physics of Fluids* 36.7 (July 2024), p. 075116.

[55] Néstor Ramos-García et al. “Investigation of the floating IEA wind 15□MW RWT using vortex methods Part II: Wake impact on downstream turbines under turbulent inflow”. In: *Wind Energy* 25 (May 2022), n/a–n/a. DOI: 10.1002/we.2738.

[56] H.H. Bruun. *Hot-Wire Anemometry: Principles and signal analysis*. Oxford Science Publications, 1995.

[57] Lunds Tekniska Högskola, Department of Energy Sciences. *Laboratory 2b: Hot Wire Anemometry*. MMV211 Fluid Mechanics. Jan. 2010.

[58] M R Abdulwahab et al. “A Review in Particle Image Velocimetry Techniques (Developments and Applications)”. In: *Journal of Advanced Research in Fluid Mechanics and Thermal Sciences* (Jan. 2020).

[59] D. Engler Faleiros. “Soap bubbles for large-scale PIV: Generation, control and tracing accuracy”. PhD thesis. Aerodynamics - Aerospace Engineering Research Group, Aerodynamics (Aerospace Engineering), 2021. DOI: 10.4233/uuid:c579128f-9e96-4e9e-9997-6ce9486e1e25.

[60] Gerrit Elsinga et al. “Tomographic Particle Image Velocimetry”. In: *Experiments in Fluids* 41 (Dec. 2006), pp. 933–947. DOI: 10.1007/s00348-006-0212-z.

[61] Constantin Jux et al. “Robotic volumetric PIV of a full-scale cyclist”. In: *Experiments in Fluids* 59.4 (2018), p. 74. DOI: 10.1007/s00348-018-2524-1. URL: https://doi.org/10.1007/s00348-018-2524-1.

[62] Hyoungsoo Kim, Jerry Westerweel, and Gerrit Elsinga. “Comparison of Tomo-PIV and 3D-PTV for microfluidic flows”. In: *Measurement Science and Technology* 24 (Dec. 2012). DOI: 10.1088/0957-0233/24/2/024007.

[63] LaVision GmbH. *Fluid Mechanics Applications*. Accessed: 2025-04-04. 2024. URL: https://www.lavision.de/en/applications/fluid-mechanics/index.php.

[64] M. Raffel et al. *Particle Image Velocimetry: A Practical Guide*. Jan. 2007. ISBN: 978-3-540-72307-3. DOI: 10.1007/978-3-540-72308-0.

[65] Giuseppe Carlo Alp Caridi et al. “HFSB-seeding for large-scale tomographic PIV in wind tunnels”. In: *Experiments in Fluids* 57.12 (2016), p. 190. ISSN: 1432-1114. DOI: 10.1007/s00348-016-2277-7. URL: https://doi.org/10.1007/s00348-016-2277-7.

[66] TU Delft. *Open Jet Facility*. Accessed: 2025-06-23. 2024. URL: https://www.tudelft.nl/lr/organisatie/afdelingen/flow-physics-and-technology/facilities/low-speed-wind-tunnels/open-jet-facility.

[67] Christian Bak et al. *The DTU 10-MW Reference Wind Turbine*. 2013. URL: https://orbit.dtu.dk/en/publications/bc5f61cd-4c51-442f-89eb-02df89ab0aa4.

[68] Alessandro Fontanella, Giulia Pra, and Marco Belloli. “Integrated Design and Experimental Validation of a Fixed-Pitch Rotor for Wind Tunnel Testing”. In: *Energies* 16 (Feb. 2023), p. 2205. DOI: 10.3390/en16052205.

[69] Quanser Inc. *Hexapod: Six Degrees of Freedom Motion Platform for Advanced Research*. Technical document published by Quanser Inc. 2019. URL: https://www.quanser.com.

[70] B. Wieneke. “Volume self-calibration for 3D particle image velocimetry”. In: *Experiments in Fluids* 45.4 (Oct. 2008), pp. 549–556. DOI: 10.1007/s00348-008-0521-5.

[71] LaVision. *Shake-the-Box Volumetric Particle Tracking at Highest Seeding Density*. 2025.

[72] LaVision. *Multi-pass Shake-the-Box*. 2025.

[73] Jan F. G. Schneiders and Fulvio Scarano. “Dense velocity reconstruction from tomographic PTV with material derivatives”. In: *Experiments in Fluids* 57.9 (2016), p. 139. ISSN: 1432-1114. DOI: 10.1007/s00348-016-2225-6. URL: https://doi.org/10.1007/s00348-016-2225-6.

[74] José Cuissa and Oskar Steiner. *An innovative and automated method for vortex identification. I. Description of the SWIRL algorithm*. Oct. 2022. DOI: 10.48550/arXiv.2210.05223.

[75] Jan Schneiders, Richard Dwight, and Fulvio Scarano. “Time-supersampling of 3D-PIV measurements with vortex-in-cell simulation”. In: *Experiments in Fluids* 55 (Feb. 2014). DOI: 10.1007/s00348-014-1692-x.

[76] Y.J. Jeon et al. “4D flow field reconstruction from particle tracks by VIC+ with additional constraints and multigrid approximation”. en. In: *Proceedings 18th International Symposium on Flow Visualization*. Ed. by Thomas Rösgen. Zurich: ETH Zurich, 2018-10-05. DOI: 10.3929/ethz-b-000279199.

[77] Jan Schneiders, Fulvio Scarano, and Gerrit Elsinga. “Resolving vorticity and dissipation in a turbulent boundary layer by tomographic PTV and VIC+”. In: *Experiments in Fluids* 58 (Mar. 2017). DOI: 10.1007/s00348-017-2318-x.

[78] Davide Medici and Per-Henrik Alfredsson. “Measurements on a wind turbine wake: 3D effects and bluff body vortex shedding”. In: *Wind Energy* 9 (May 2006), pp. 219–236. DOI: 10.1002/we.156.

[79] Ingrid Neunaber. “Stochastic investigation of the evolution of small-scale turbulence in the wake of a wind turbine exposed to different inflow conditions in Oldenburg”. PhD thesis. Jan. 2019.

[80] LaVision. *FlowMaster: Advanced PIV / PTV Systems for Quantitative Flow Field Analysis*. 2025.

[81] L.E.M. Lignarolo. “On the Turbulent Mixing in Horizontal Axis Wind Turbine Wakes”. Doctoral thesis. Delft University of Technology, 2016.

[82] Iacopo Tirelli et al. “Full-domain POD modes from PIV asynchronous patches”. In: *Experiments in Fluids* 66 (May 2025). DOI: 10.1007/s00348-025-04029-6.

[83] LaVision. *PIV Uncertainty Quantification: Instantaneous local uncertainties added to PIV results in DaVis*. 2018.

A

Test Matrix

A more detailed test matrix is presented here. All measured cases are shown with their respective tracking number used during the experiment, colored red when the measurement was faulty and was not used or had to be re-measured.

The initially planned test matrix only contemplated 34 measurements, but due to extra time in the wind tunnel facility, more cases were added to improve wake characterization. Note the distinction in amplitude of the test cases from run 35 to run 38: these are not a repetition of the previously tested 3.5D volume, but a extension of the test by including different amplitudes corresponding to a different normalized velocity variation ($\Delta V^* = 0.05$).

Run #	Case	Frequency [Hz]	ΔV^*	Amplitude	U_∞	Rotor speed [rpm]	X Location [Diameter]	Measuring Time [s]
1	Flow	n.a.	n.a.	n.a.	4	0	1D	10
2	Static	n.a.	n.a.	n.a.	4	480	1D	10
3	Surge	2	0.1	31.8 mm	4	480	1D	10
4	Surge	5	0.1	12.7 mm	4	480	1D	10
5	Pitch	2	0.1	1.57 deg	4	480	1D	10
6	Pitch	5	0.1	0.63 deg	4	480	1D	10
7	Surge	2	0.1	31.8 mm	4	480	1.625D	10
8	Surge	2	0.1	31.8 mm	4	480	1.625D	10
9	Surge	5	0.1	12.7 mm	4	480	1.625D	10
10	Pitch	2	0.1	1.57 deg	4	480	1.625D	10
11	Pitch	5	0.1	0.63 deg	4	480	1.625D	10
12	Pitch	5	0.1	0.63 deg	4	480	1.625D	10
13	Static	n.a.	n.a.	n.a.	4	480	1.625D	10
14	Flow	n.a.	n.a.	n.a.	4	0	1.625D	10
15	Flow	n.a.	n.a.	n.a.	4	0	2.25D	10
16	Static	n.a.	n.a.	n.a.	4	480	2.25D	10
17	Surge	2	0.1	31.8 mm	4	480	2.25D	10
18	Surge	5	0.1	12.7 mm	4	480	2.25D	10
19	Pitch	2	0.1	1.57 deg	4	480	2.25D	10
20	Pitch	5	0.1	0.63 deg	4	480	2.25D	10
21	Surge	2	0.1	31.8 mm	4	480	3.5D	10
22	Surge	5	0.1	12.7 mm	4	480	3.5D	10
23	Pitch	2	0.1	1.57 deg	4	480	3.5D	10
24	Pitch	5	0.1	0.63 deg	4	480	3.5D	10
25	Pitch	2	0.1	1.57 deg	4	480	3.5D	10
26	Pitch	5	0.1	0.63 deg	4	480	3.5D	10
27	Static	n.a.	n.a.	n.a.	4	480	3.5D	10
28	Flow	n.a.	n.a.	n.a.	4	0	3.5D	10
29	Flow	n.a.	n.a.	n.a.	4	0	4.75D	10
30	Static	n.a.	n.a.	n.a.	4	480	4.75D	10
31	Surge	2	0.1	31.8 mm	4	480	4.75D	10
32	Surge	5	0.1	12.7 mm	4	480	4.75D	10
33	Pitch	2	0.1	1.57 deg	4	480	4.75D	10

Run #	Case	Frequency [Hz]	ΔV^*	Amplitude	U_∞	Rotor speed [rpm]	X Location [Diameter]	Measuring Time [s]
34	Pitch	5	0.1	0.63 deg	4	480	4.75D	10
35	Surge	2	*0.05*	*15.9 mm*	4	480	3.5D	10
36	Surge	5	*0.05*	*6.4 mm*	4	480	3.5D	10
37	Pitch	2	*0.05*	*0.79 deg*	4	480	3.5D	10
38	Pitch	5	*0.05*	*0.32 deg*	4	480	3.5D	10
39	Wave1	n.a.	n.a.	n.a.	*3.43*	*408*	3.5D	*20*
40	Wave2	n.a.	n.a.	n.a.	*3.8*	*474*	3.5D	*20*
41	Wave3	n.a.	n.a.	n.a.	*3.8*	*474*	3.5D	*20*
42	Static	n.a.	n.a.	n.a.	4	480	5.375D	10
43	Surge	2	0.1	31.8 mm	4	480	5.375D	10
44	Surge	5	0.1	12.7 mm	4	480	5.375D	10
45	Pitch	2	0.1	1.57 deg	4	480	5.375D	10
46	Pitch	5	0.1	0.63 deg	4	480	5.375D	10
47	Flow	n.a.	n.a.	n.a.	4	0	5.375D	10

B

Wake Recovery Predictions Outside of the Measured Domain

To further explore the potential extent of the faster wake recovery observed in surge cases, an extrapolation of the available data, and a comparison to a similar study reaching further downstream are presented here. The aim of this chapter is to provide supporting evidence that the wake may recover 2–3 rotor diameters faster in the surge case compared to the static case.

A study from literature investigates wake behavior under harmonic surge motion up to 10D downstream [24]. It reports a smaller velocity deficit in the wake for surge compared to the static case, consistent with the findings of the present work. Here is a summary of the parameters in both the present study and in [24]:

	f [Hz]	A [m]	f_r [-]	A_r [-]	D [m]	TSR [-]
Surge 2Hz	2	0.032	0.6	0.026	1.2	7.5
Surge 0.3Hz [24]	0.3	0.05	0.6	0.02	2.52	7
Surge 1.3Hz [24]	1.3	0.05	2.2	0.02	2.52	7

Table B.1: Parameters used for each study, where f is frequency, A is amplitude, f_r is reduced frequency, A_r is reduced frequency, D is rotor diameter, and TSR is Tip Speed Ratio

While the operating conditions (such as rotor diameter and amplitude) differ between the studies, the reduced frequency (f_r) for *Surge 0.3Hz* matches that of the present work ($f_r = 0.6$). This is an important similarity, as f_r strongly influences wake unsteadiness [19]. The alignment in f_r enhances the relevance of comparing the wake recovery behavior across these studies, even if exact flow or turbine conditions differ.

To further explore the potential extent of the faster wake recovery observed in surge cases, we applied a simple extrapolation to our experimental data. An exponential decay model was used to fit the average velocity deficit ΔU:

$$\frac{U_\infty - \bar{u}(x)}{U_\infty} = Ce^{-kx} \tag{B.1}$$

Where C and k are constants fitted using available measurements, and x is the downstream distance normalized by rotor diameter D. The velocity deficit data corresponds to a location close to the wake centerline, specifically at $z/D = 0.25$, to maintain consistency across datasets.

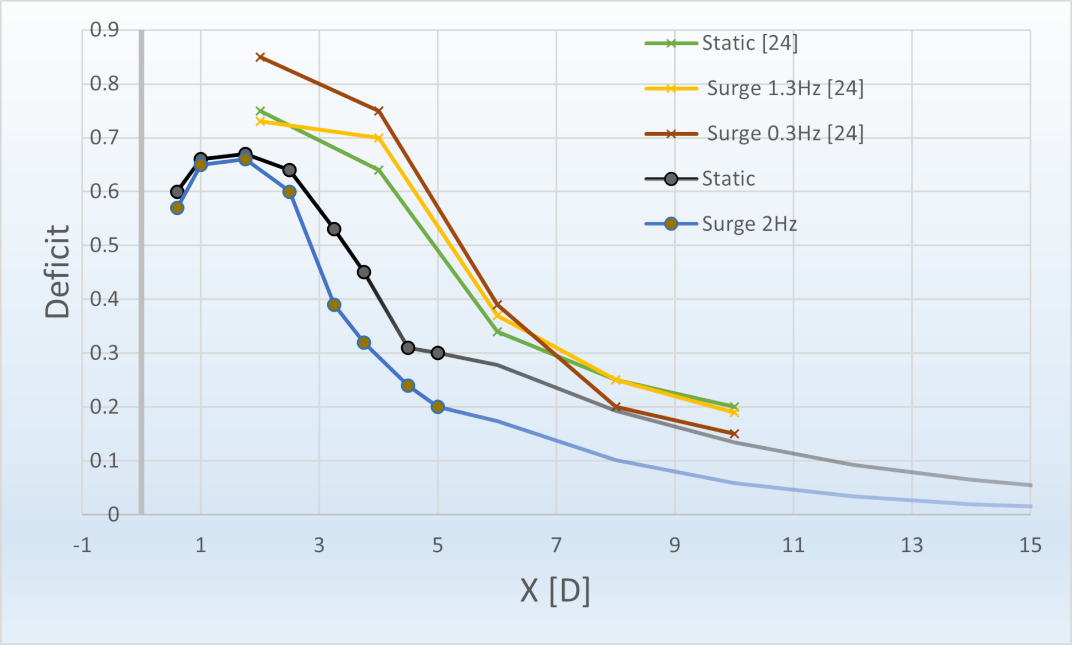

Figure B.1: Wake recovery depicted by streamwise velocity deficit normalized by freestream velocity $(U_\infty - \bar{u})/U_\infty$. Static and Surge 2Hz shown with the black and blue lines respectively, where the dots represent measured values, and the region downstream of 5D represents the extrapolation. Additionally, [24] results, where similar conditions to this study are used, are present from 2D to 10D range.

While the extrapolation is based on a simple model and has clear limitations, particularly the assumption of a continuous exponential decay beyond the measured region, it offers a useful approximation. If the identified trend continues, the surge case could show a recovery that is approximately 2–3D ahead of the static case. It also matches with the ”Surge 0.3Hz” case from literature, showing 2D improvement in their last measured location (10D). This hypothesis should, however, be interpreted with caution and validated with more extensive downstream data.

C

Additional Results for $\Delta V* = 0.05$ & Wave Cases

Complementary contour plots as part of $\Delta V* = 0.05$ and wave case studies are presented here for Velocity u, Velocity v, and Velocity w.

These cases were measured exclusively at a distance of 3.1 to 3.75 rotor diameters downstream, representing a compromise between the near and far wake regions. The smaller normalized velocity variation ($\Delta V^* = 0.05$) is compared to the static case and $\Delta V^* = 0.1$ cases. The two different wave cases are also included, representing moderate wave case on the left plot and rough wave case on the right plot.

As it was noted in the test matrix (subsection 3.2.3) the amplitudes of the motions are now 15.9mm & 6.4mm for surge low and high frequency respectively (previously 31.8mm & 12.7mm), and 0.79 deg & 0.32 deg for pitch low and high frequency respectively (previously 1.57deg & 0.63deg). The measuring time was $10s$ at a frequency of $400Hz$ for the non-wave cases, and $20s$ at $400Hz$ for the wave cases. The wave characteristics were given in Table 4.1.

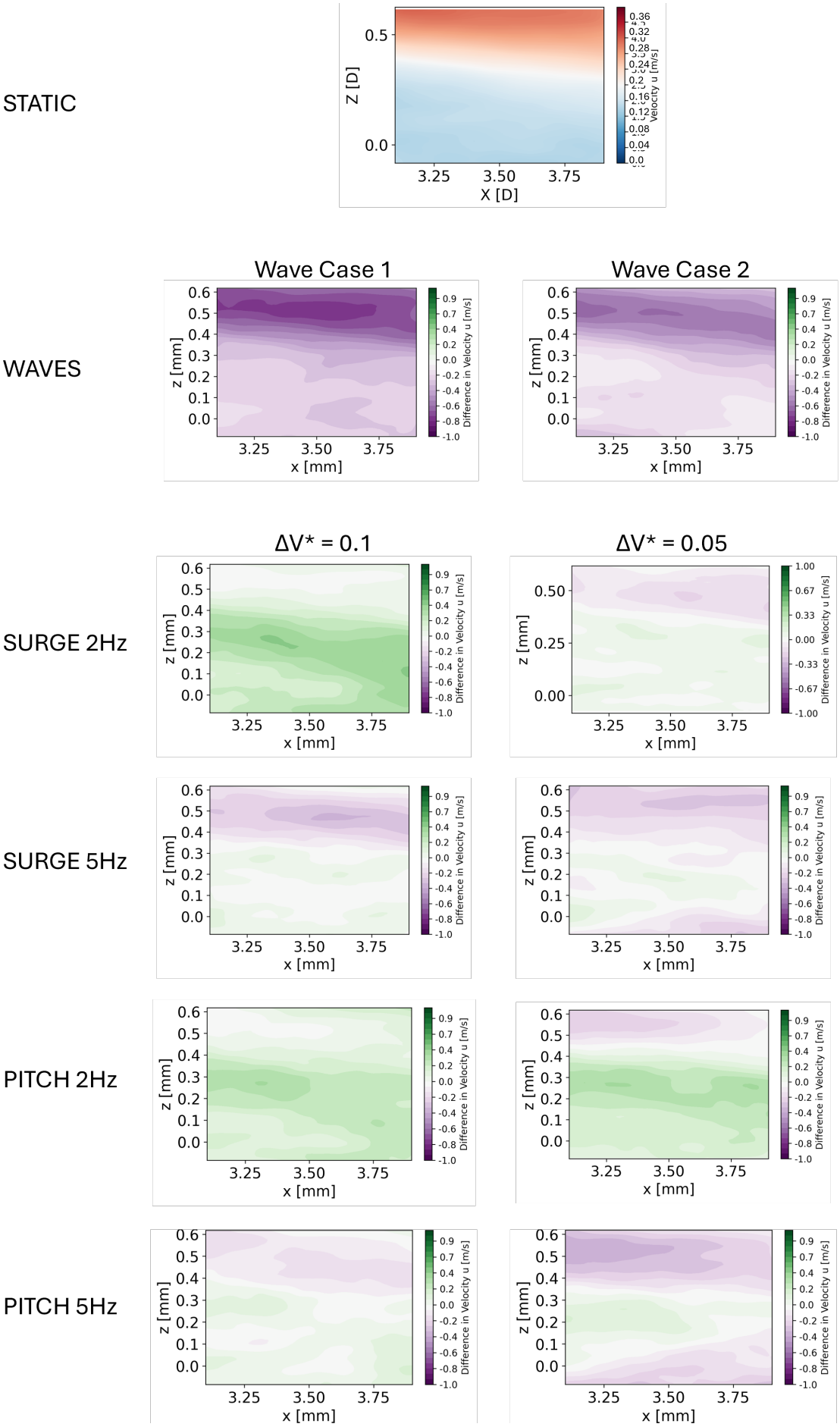

Figure C.1: Velocity u for $\Delta V^* = 0.1$, $\Delta V^* = 0.05$ & Wave cases.

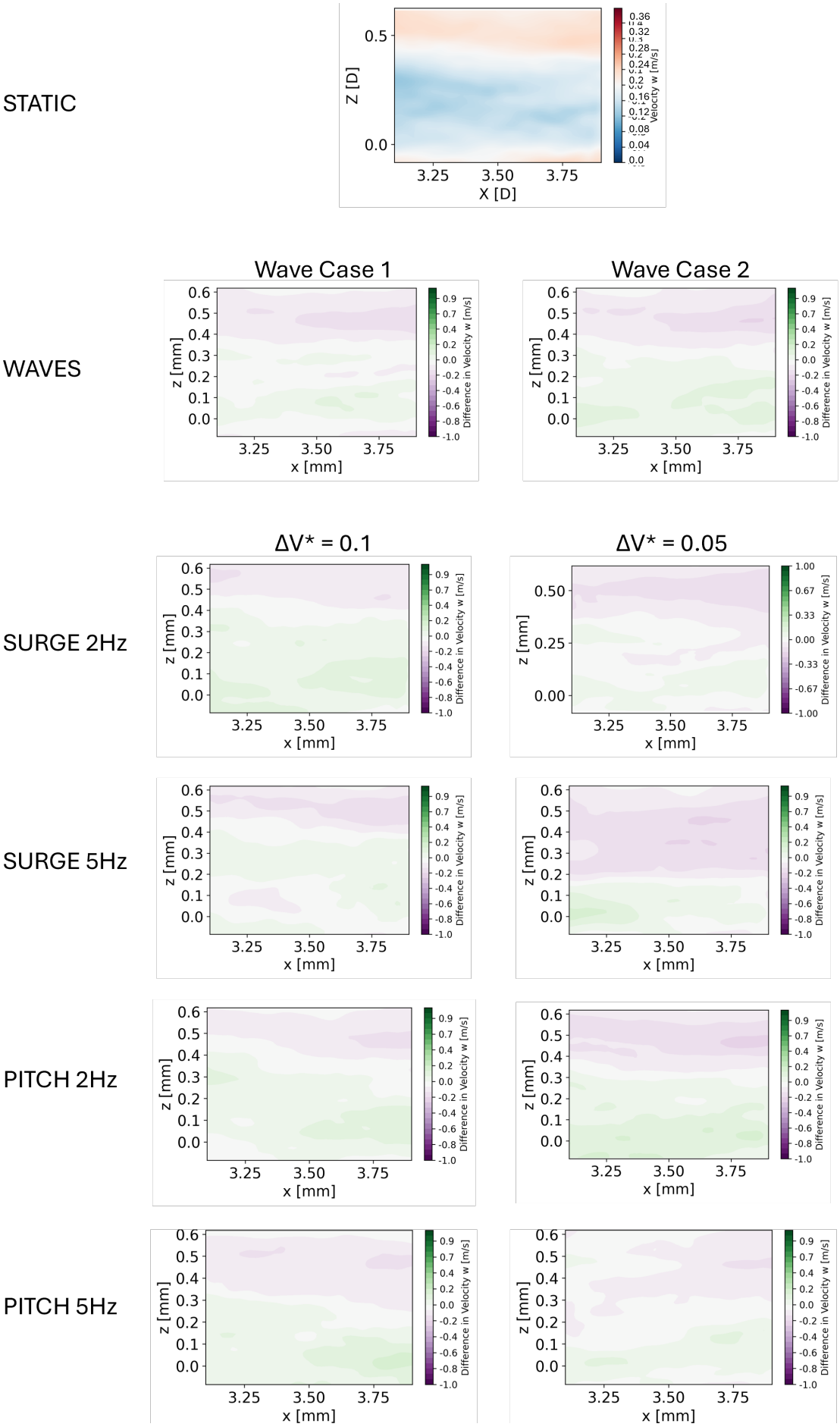

Figure C.2: Velocity w for $\Delta V^* = 0.1$, $\Delta V^* = 0.05$ & Wave cases.

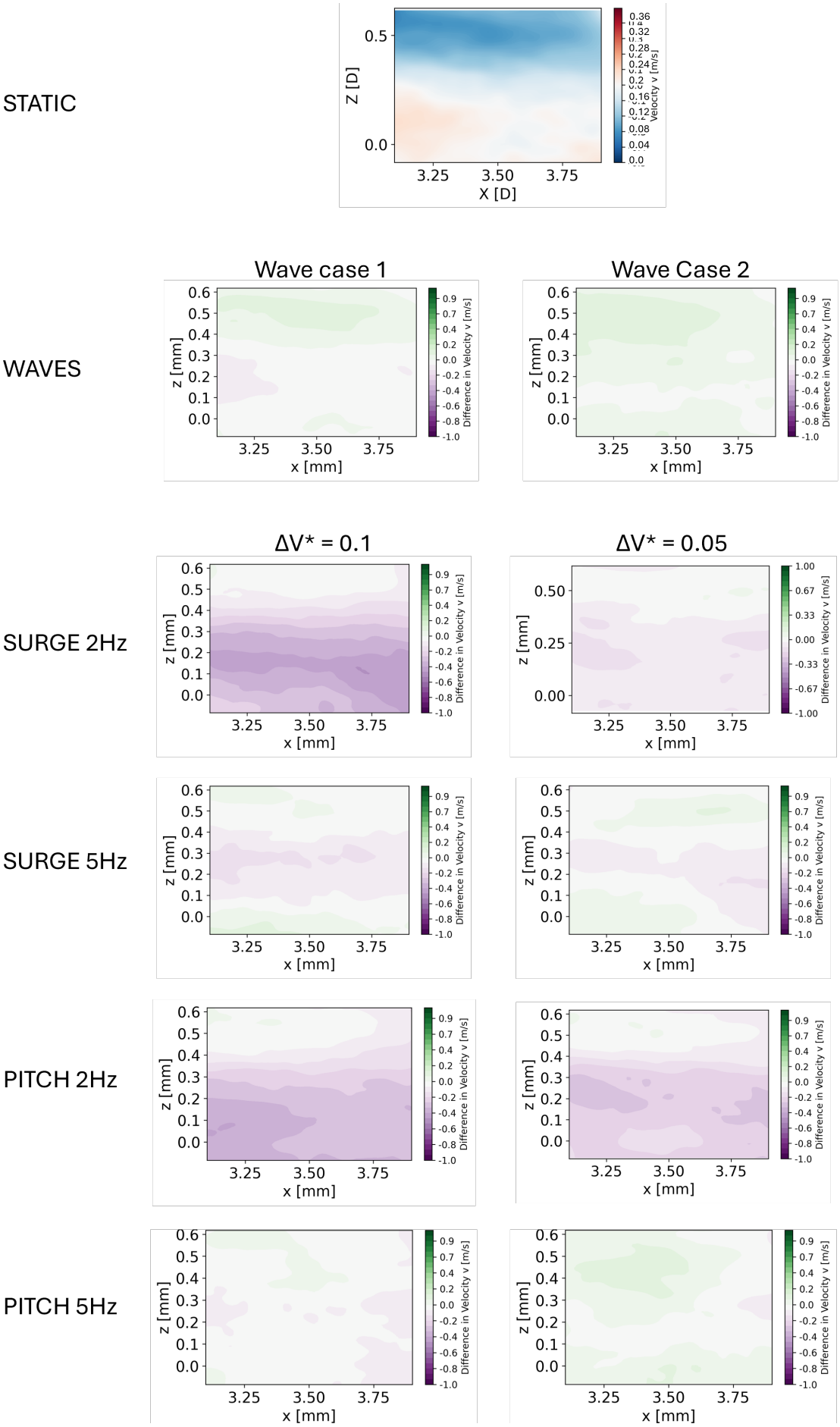

Figure C.3: Velocity w for $\Delta V^* = 0.1$, $\Delta V^* = 0.05$ & Wave cases.

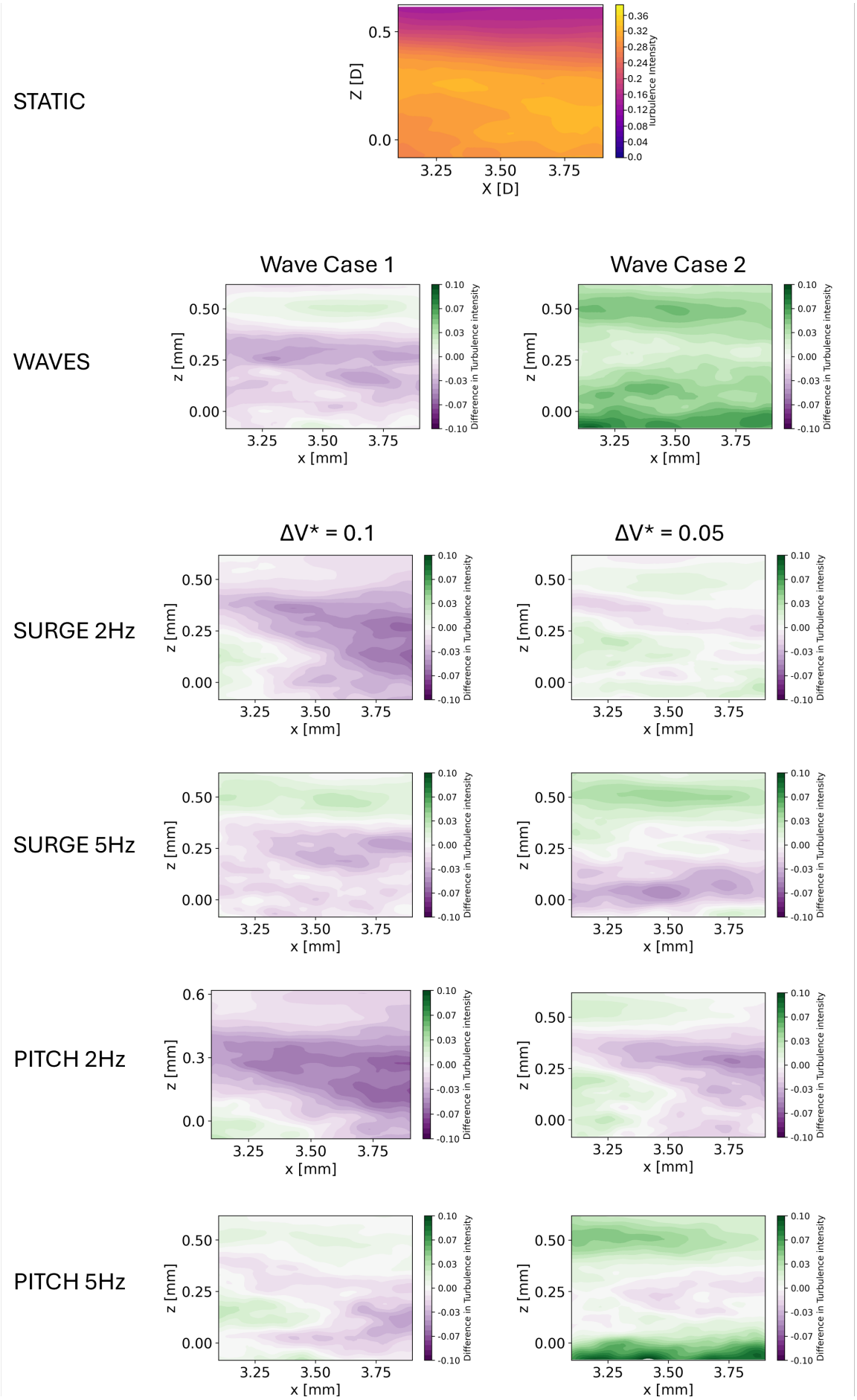

Figure C.4: Turbulence Intensity TI for $\Delta V^* = 0.1$, $\Delta V^* = 0.05$ & Wave cases.

D

Additional Results from Phase-Lock Analysis

The following pages present the averaged phase-locked velocity and TI fields corresponding to Positions 1, 2, 3, and 4 of the oscillatory motion.

The duration of each cycle varied with the motion frequency (e.g., a 2 Hz frequency corresponds to 200 measurements per cycle), which defined the segment length used for phase discretizations. Each cycle was evenly divided into four key positions:

- Pos 1: $x = 0$, $u < 0$ (moving against the wind),
- Pos 2: $x = -\max$, $u = 0$,
- Pos 3: $x = 0$, $u > 0$ (moving with the wind),
- Pos 4: $x = \max$, $u = 0$.

Although Position 1 figures were previously included in the main body of the report, they are reproduced here for reference and completeness, alongside the remaining positions. As reference for interpreting the figures, LF denotes low frequency ($2\mathrm{Hz}$) and HF denotes high frequency ($5\mathrm{Hz}$)

Pos 1: Velocity Components & Turbulence Intensity

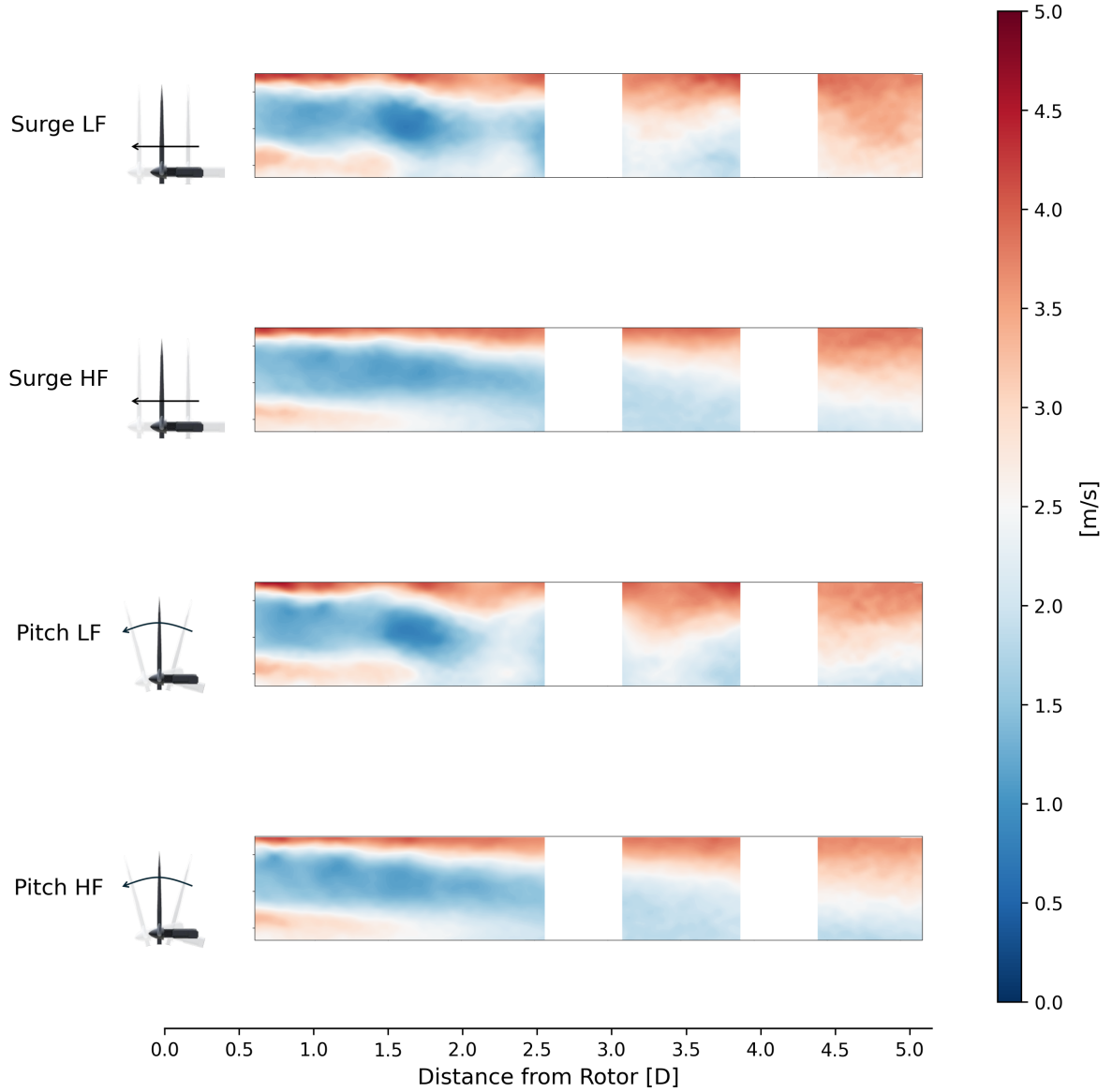

Figure D.1: Phase-locked average streamwise velocity component normalized by freestream velocity $\langle \bar{u} \rangle / U_\infty$ for static and motion cases at Position 1.

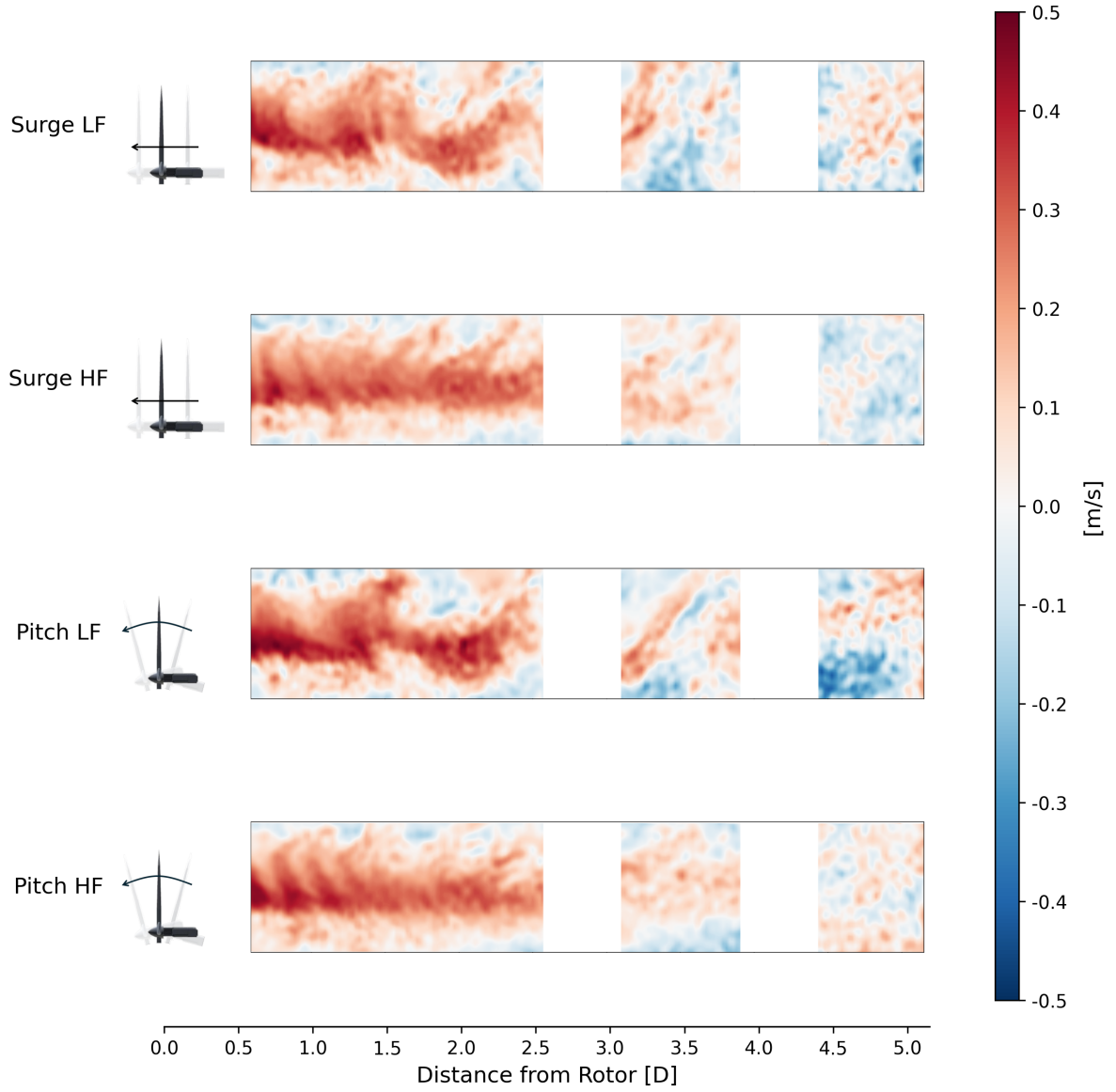

Figure D.2: Phase-locked average spanwise velocity component normalized by freestream velocity $\langle \bar{v} \rangle / U_\infty$ for static and motion cases at Position 1.

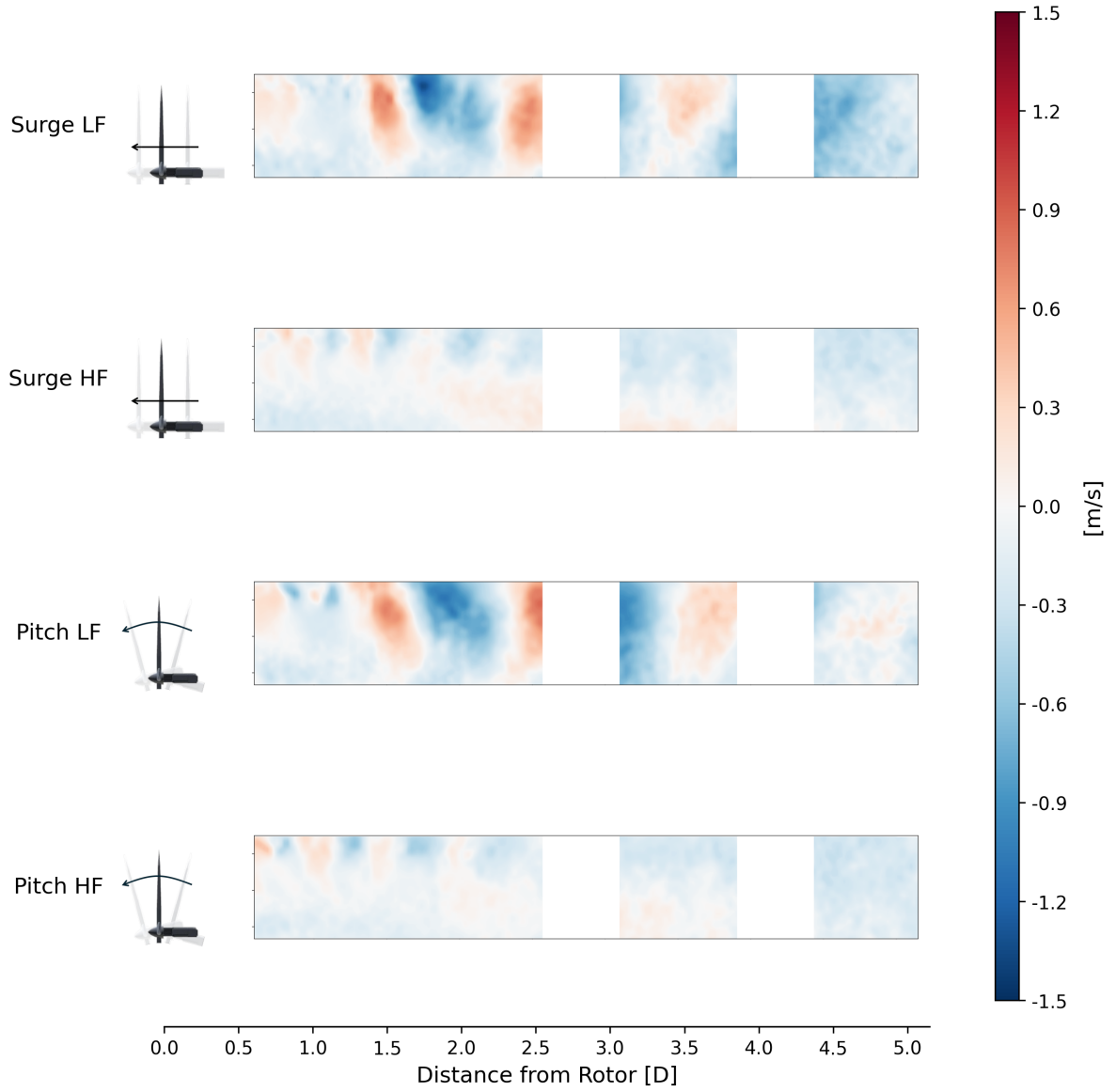

Figure D.3: Phase-locked average vertical velocity component normalized by freestream velocity $\langle \bar{w} \rangle / U_\infty$ for static and motion cases at Position 1.

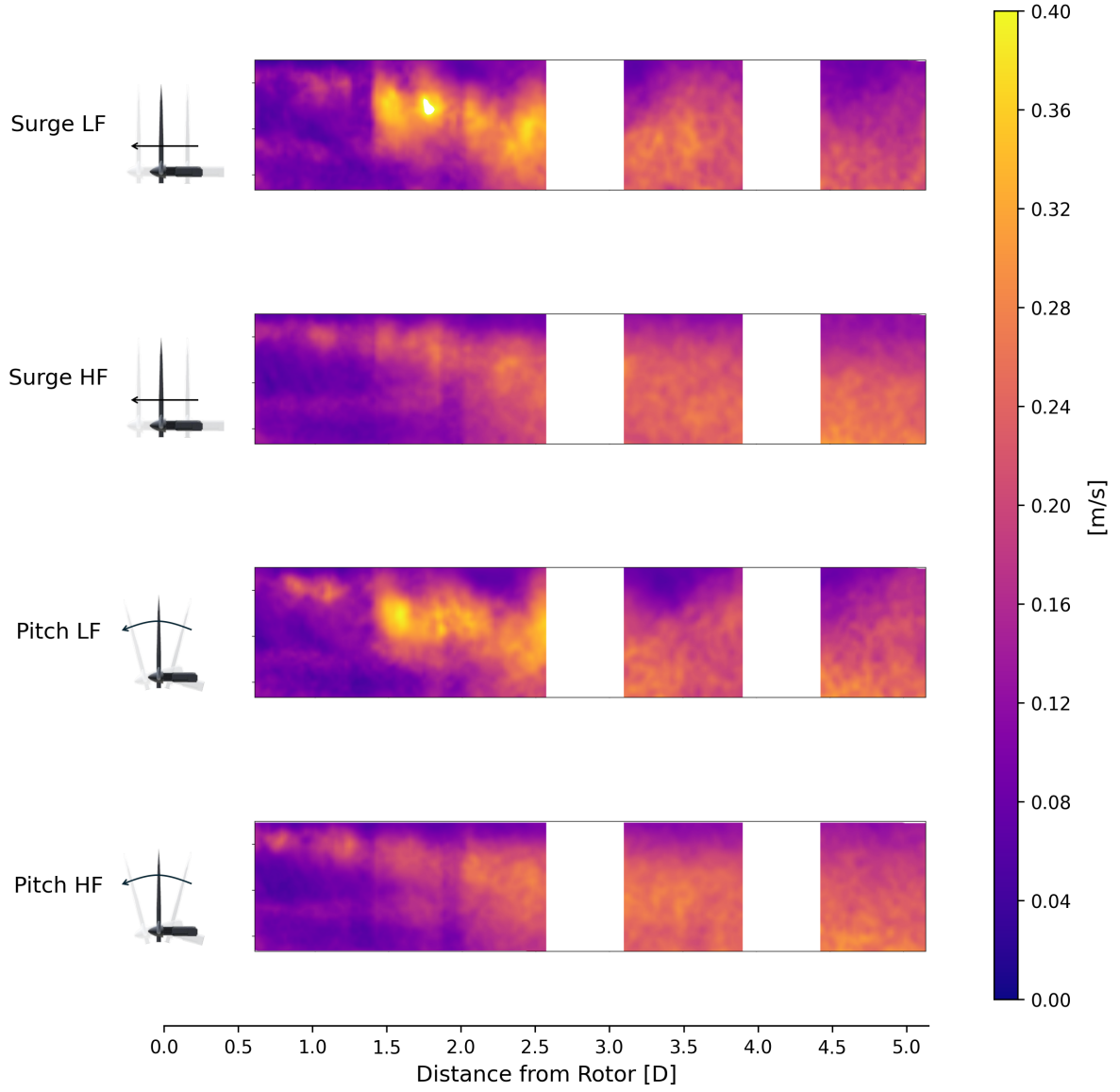

Figure D.4: Phase-locked turbulence intensity TI for static and motion cases at Position 1.

Pos 2: Velocity Components & Turbulence Intensity

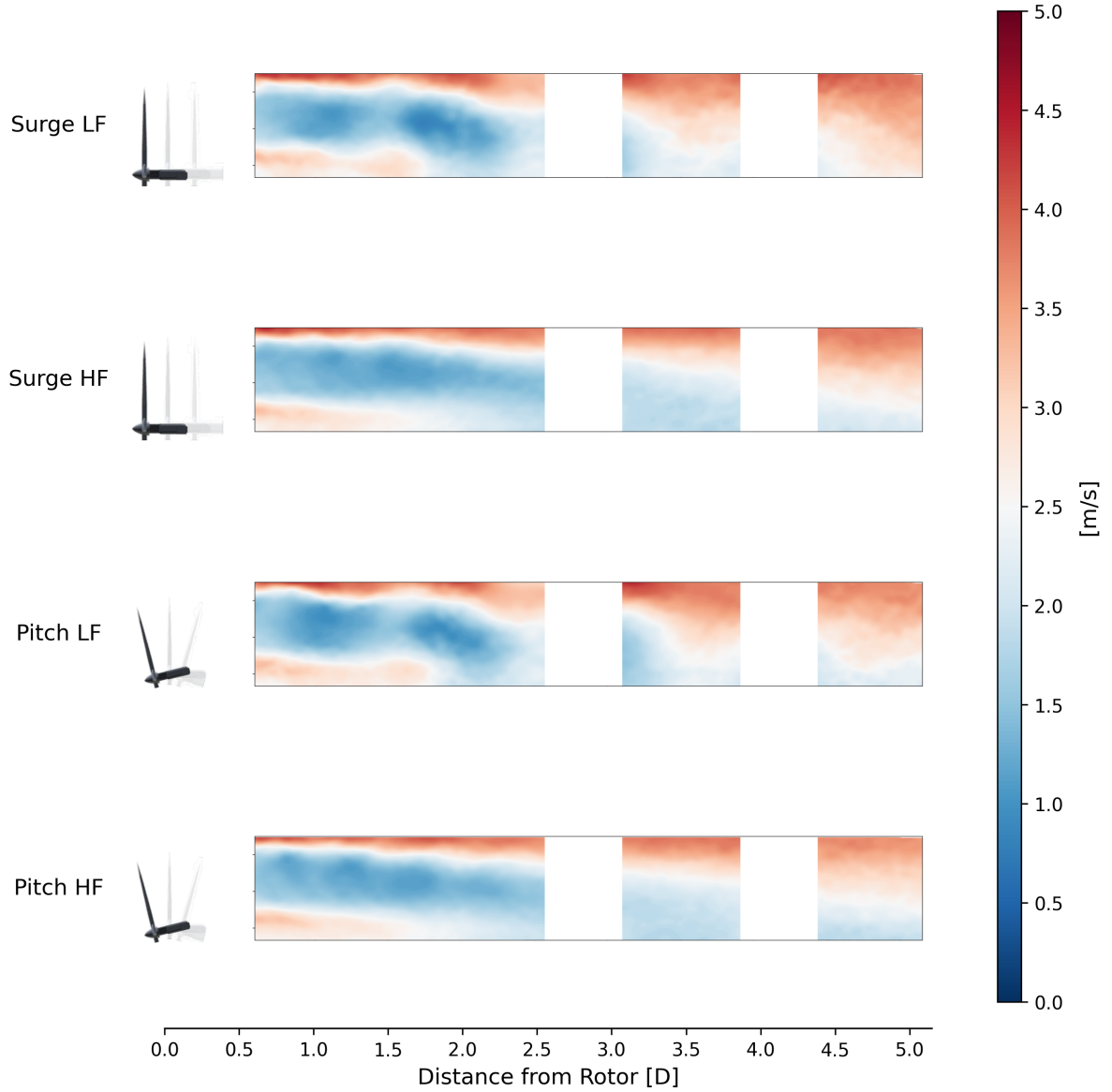

Figure D.5: Phase-locked average streamwise velocity component normalized by freestream velocity $\langle \bar{u} \rangle / U_\infty$ for static and motion cases at Position 2.

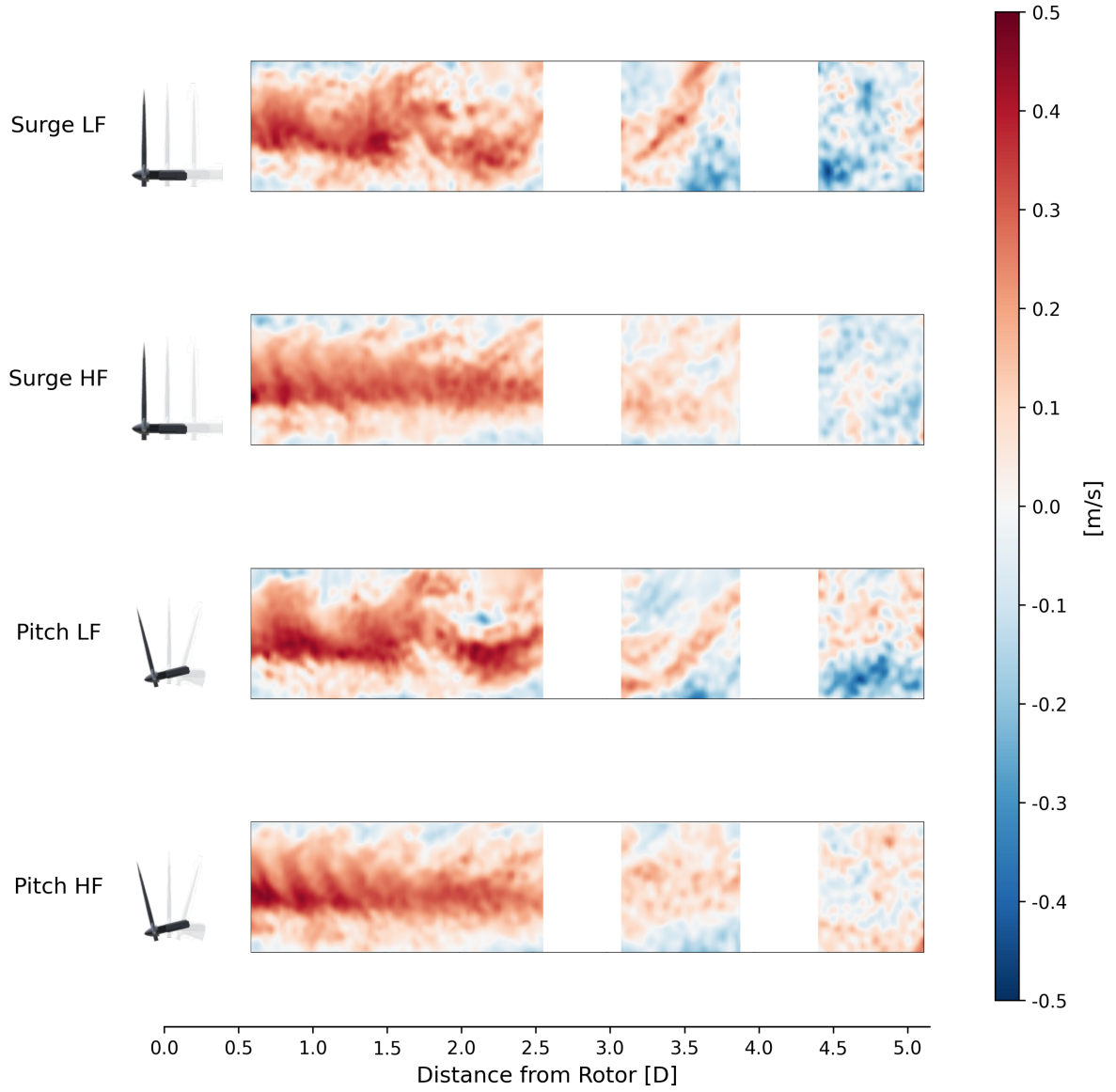

Figure D.6: Phase-locked average spanwise velocity component normalized by freestream velocity $\langle \bar{v} \rangle / U_\infty$ for static and motion cases at Position 2.

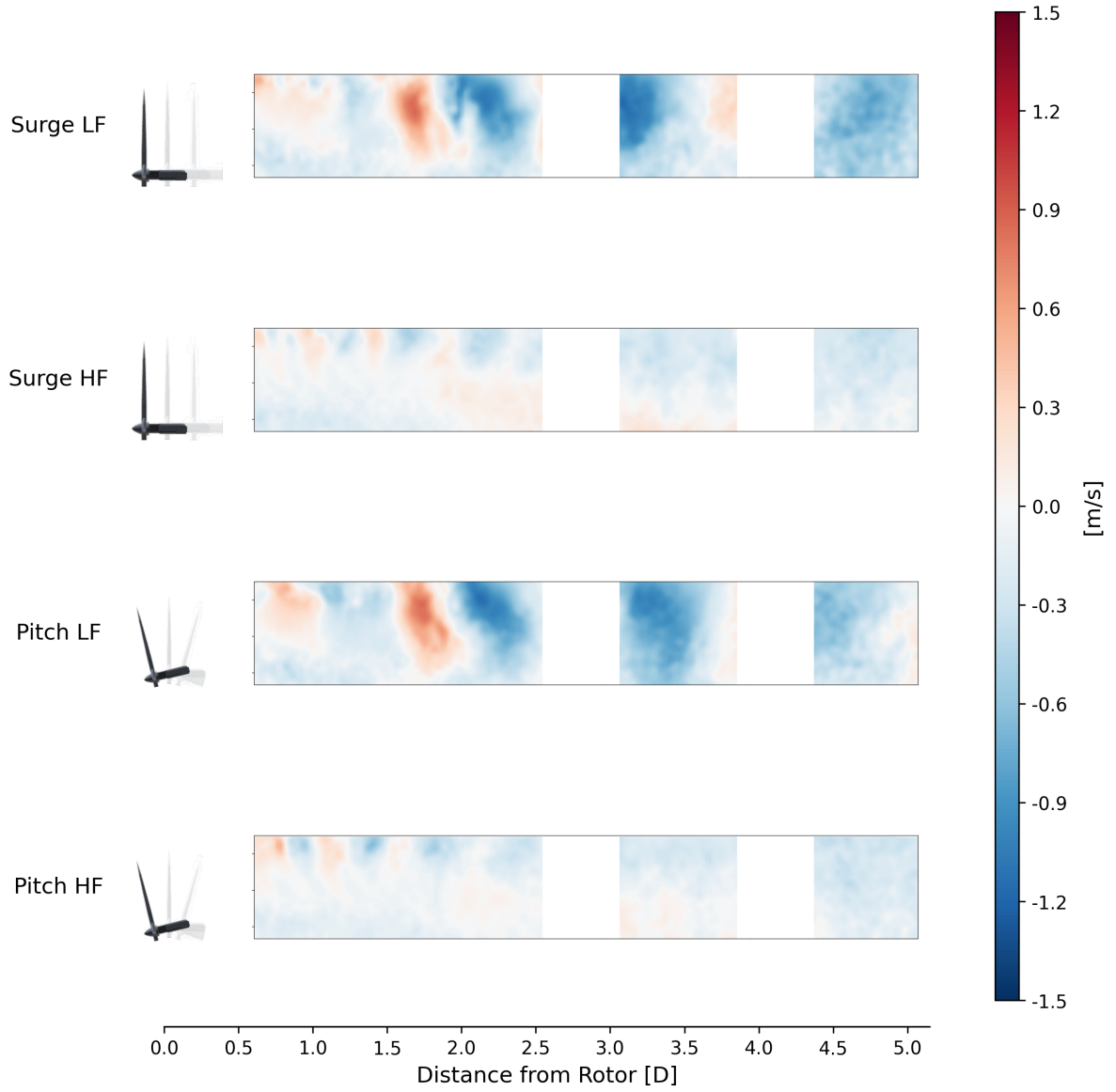

Figure D.7: Phase-locked average vertical velocity component normalized by freestream velocity $\langle \bar{w} \rangle / U_\infty$ for static and motion cases at Position 2.

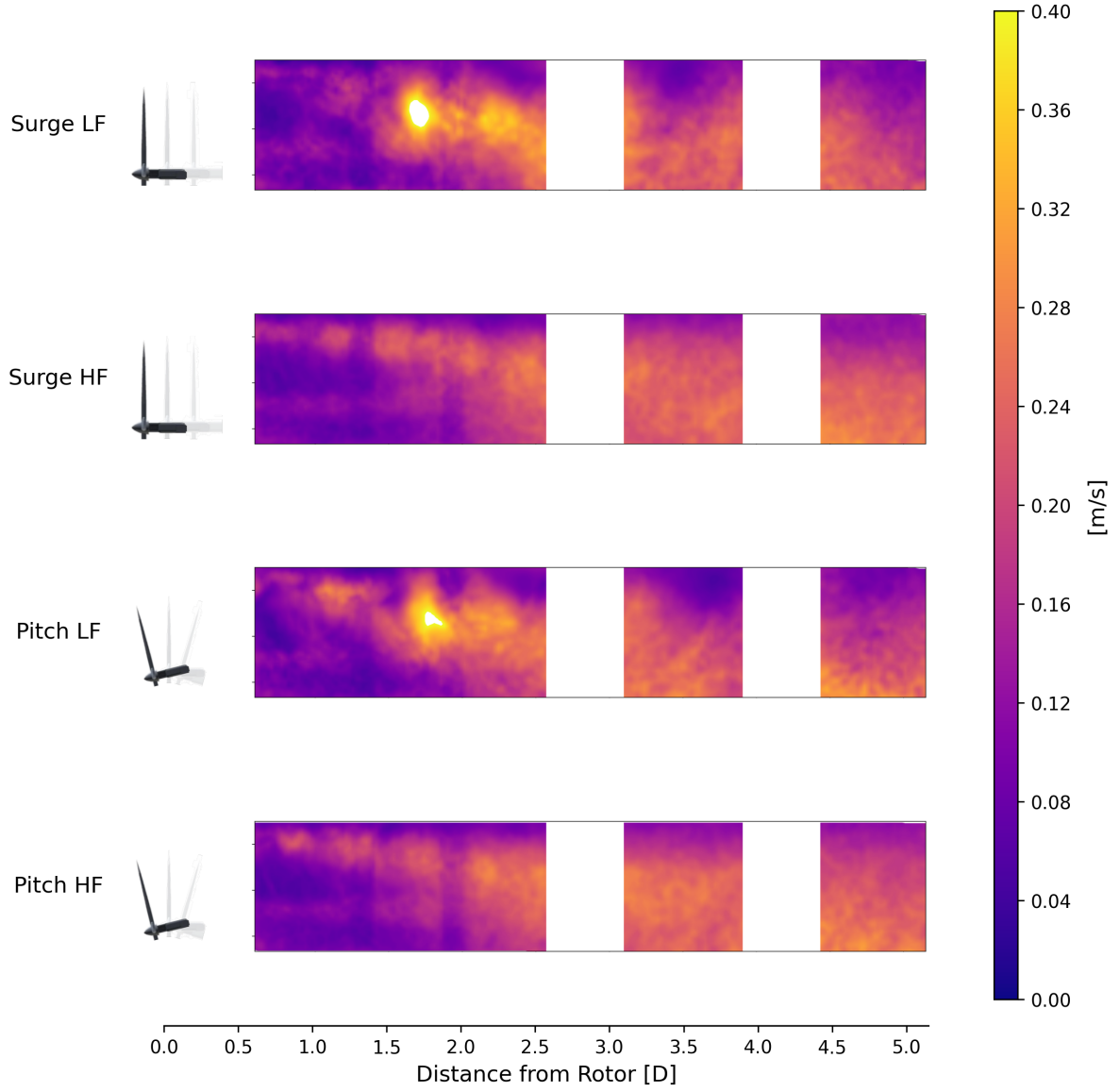

Figure D.8: Phase-locked average turbulence intensity TI for static and motion cases at Position 2.

Pos 3: Velocity Components & Turbulence Intensity

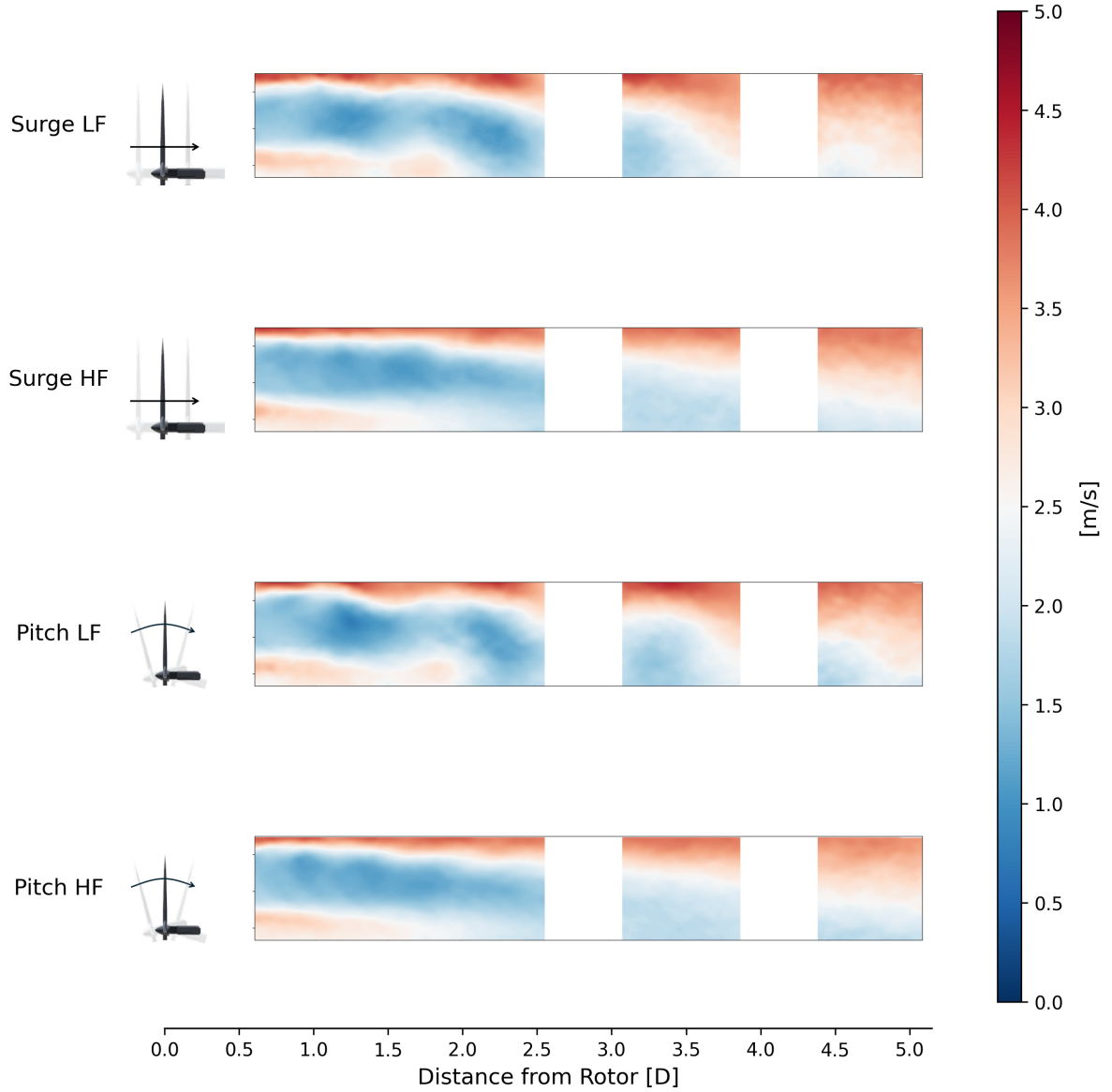

Figure D.9: Phase-locked average streamwise velocity component normalized by freestream velocity $\langle \bar{u} \rangle / U_\infty$ for static and motion cases at Position 3.

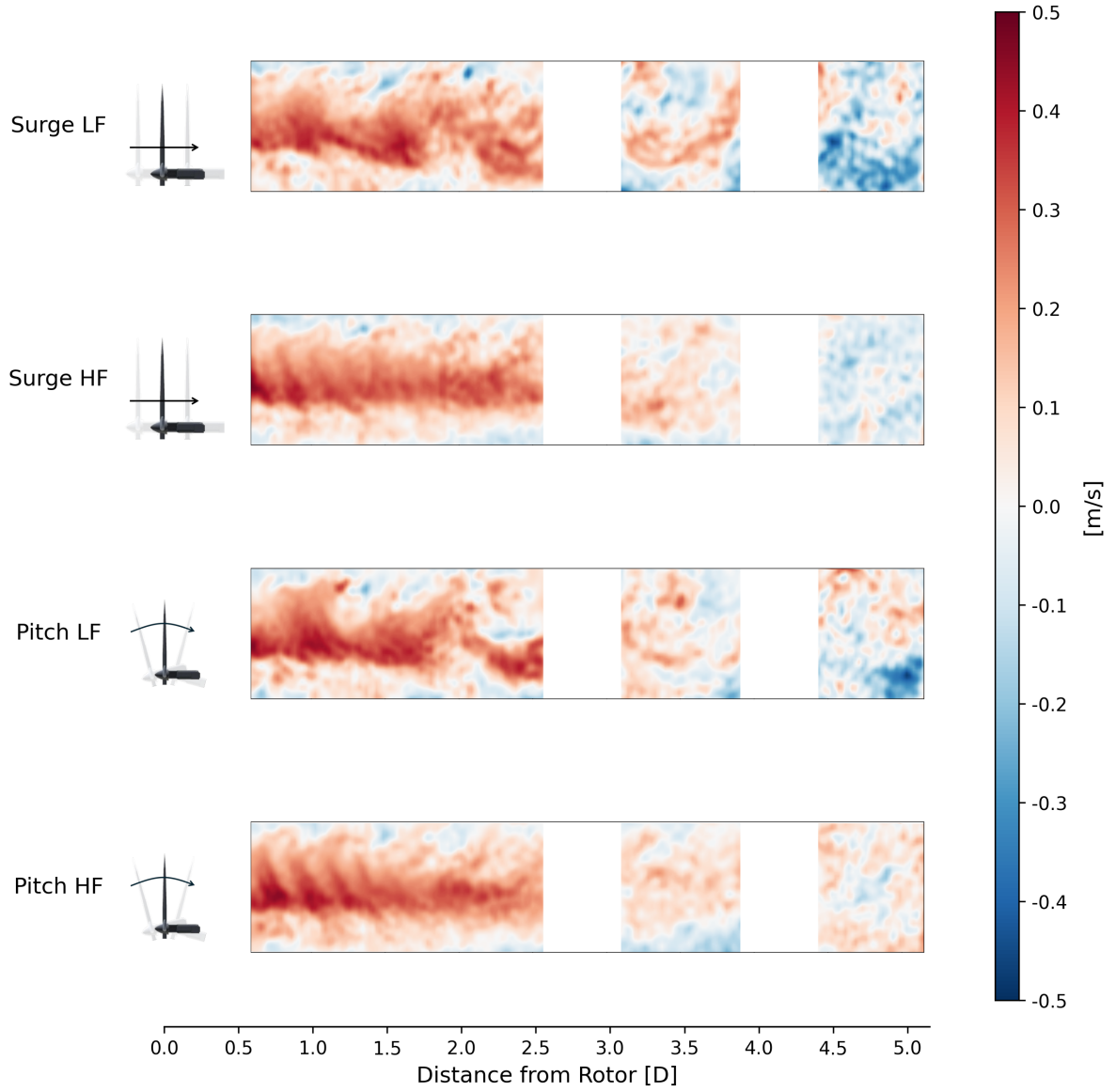

Figure D.10: Phase-locked average spanwise velocity component normalized by freestream velocity $\langle \bar{v} \rangle / U_\infty$ for static and motion cases at Position 3.

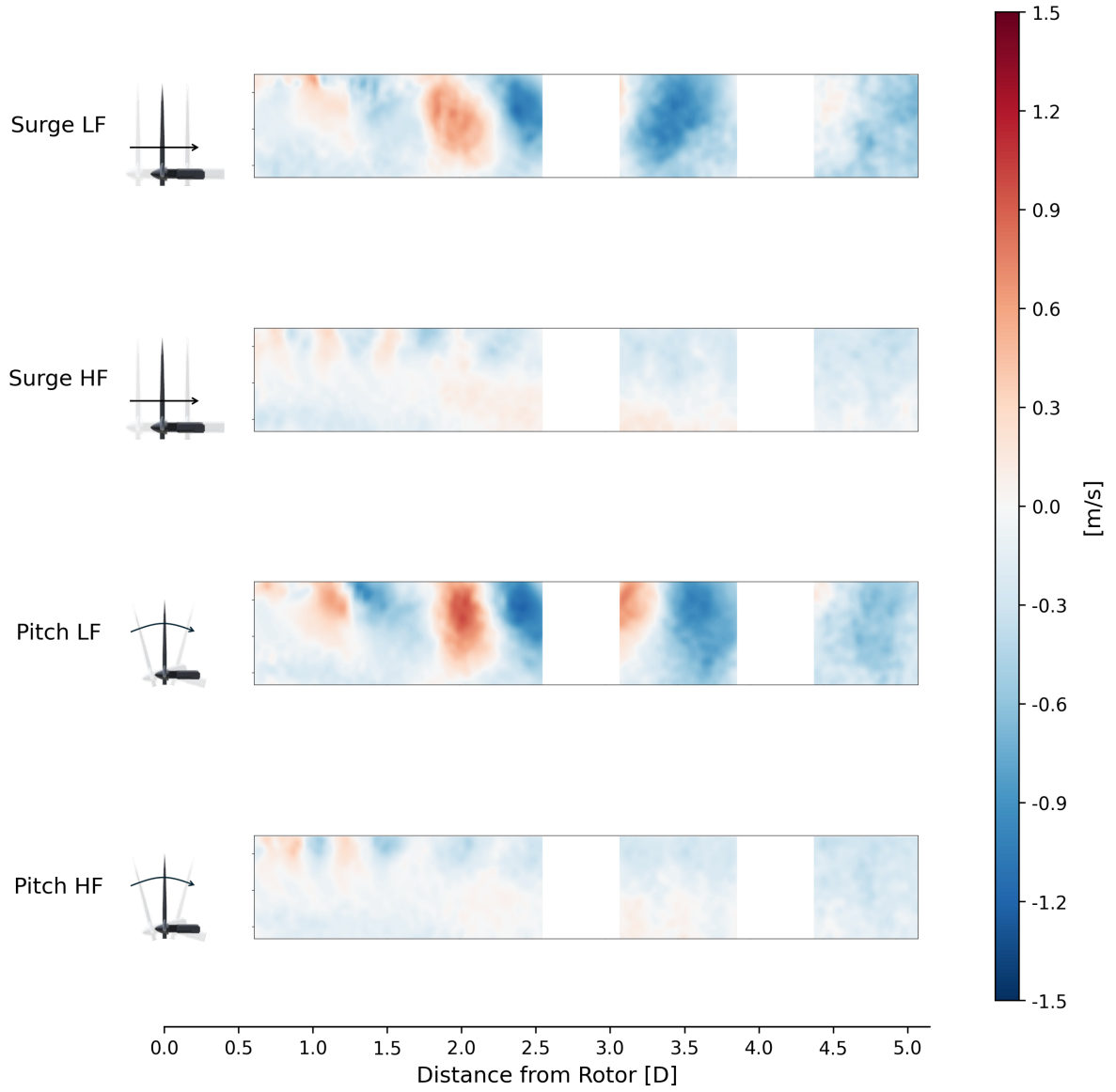

Figure D.11: Phase-locked average vertical velocity component normalized by freestream velocity $\langle \bar{w} \rangle / U_\infty$ for static and motion cases at Position 3.

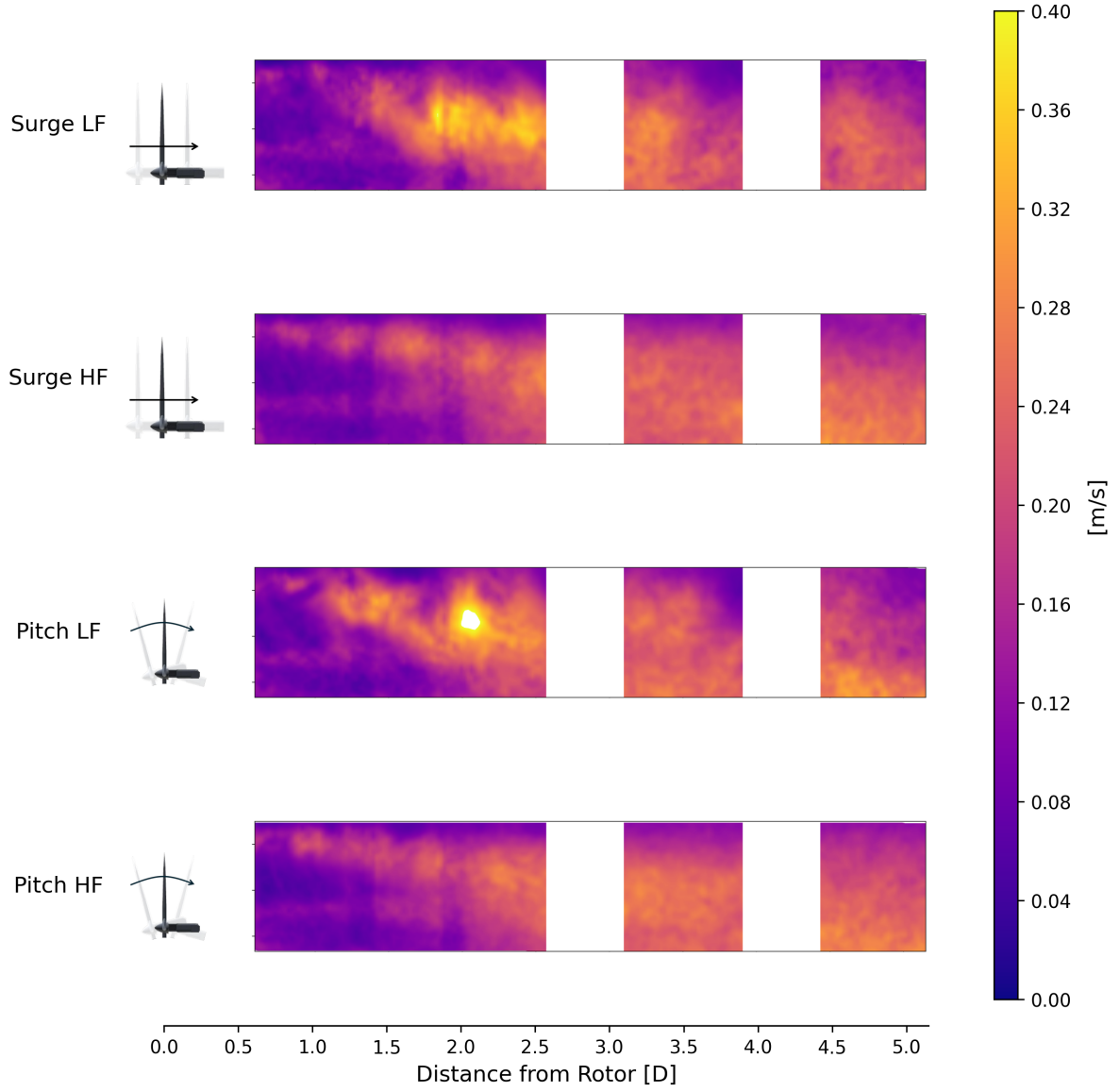

Figure D.12: Phase-locked average turbulence intensity TI for static and motion cases at Position 3.

Pos 4: Velocity Components & Turbulence Intensity

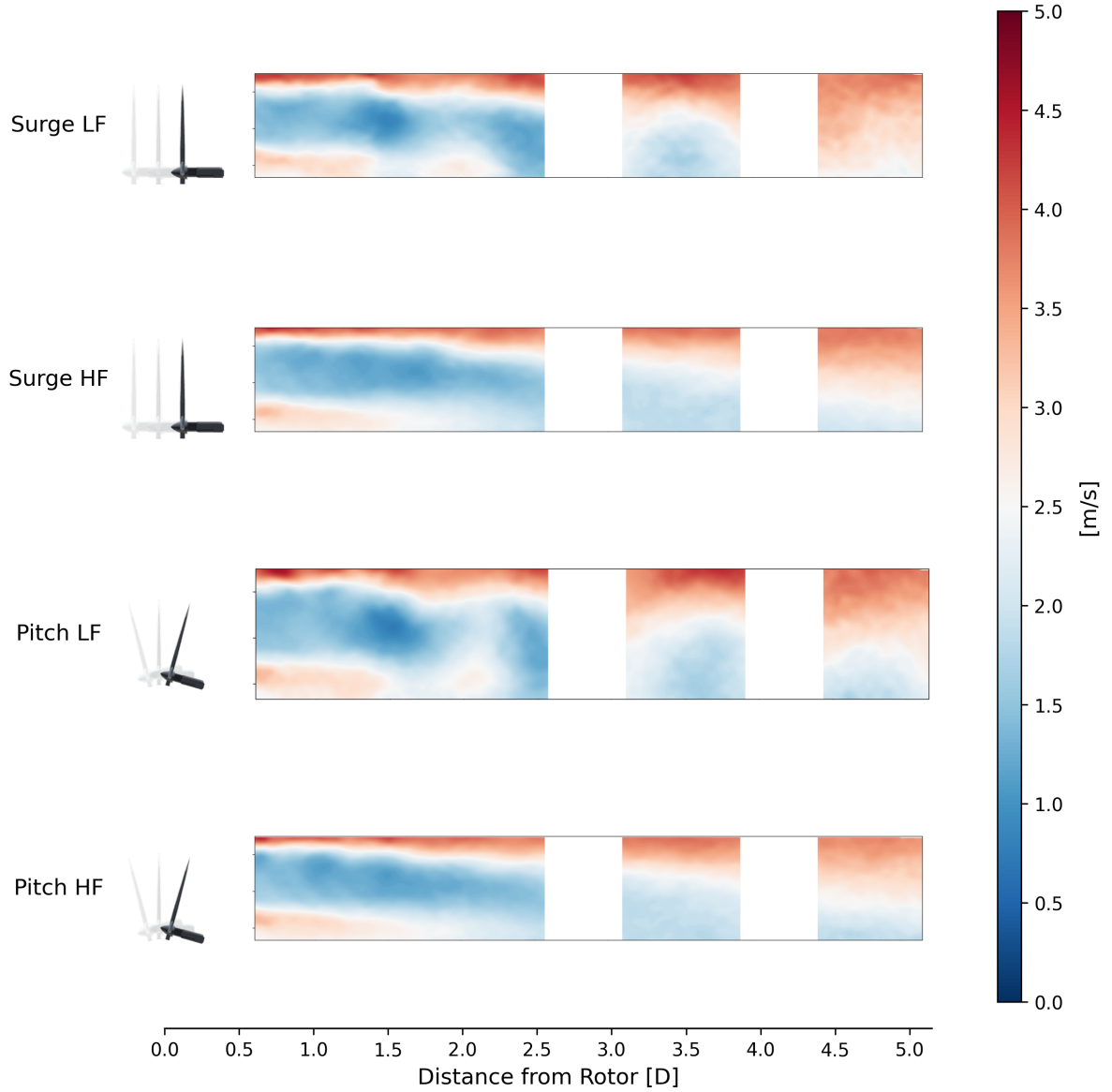

Figure D.13: Phase-locked average streamwise velocity component normalized by freestream velocity $\langle \bar{u} \rangle / U_\infty$ for static and motion cases at Position 4.

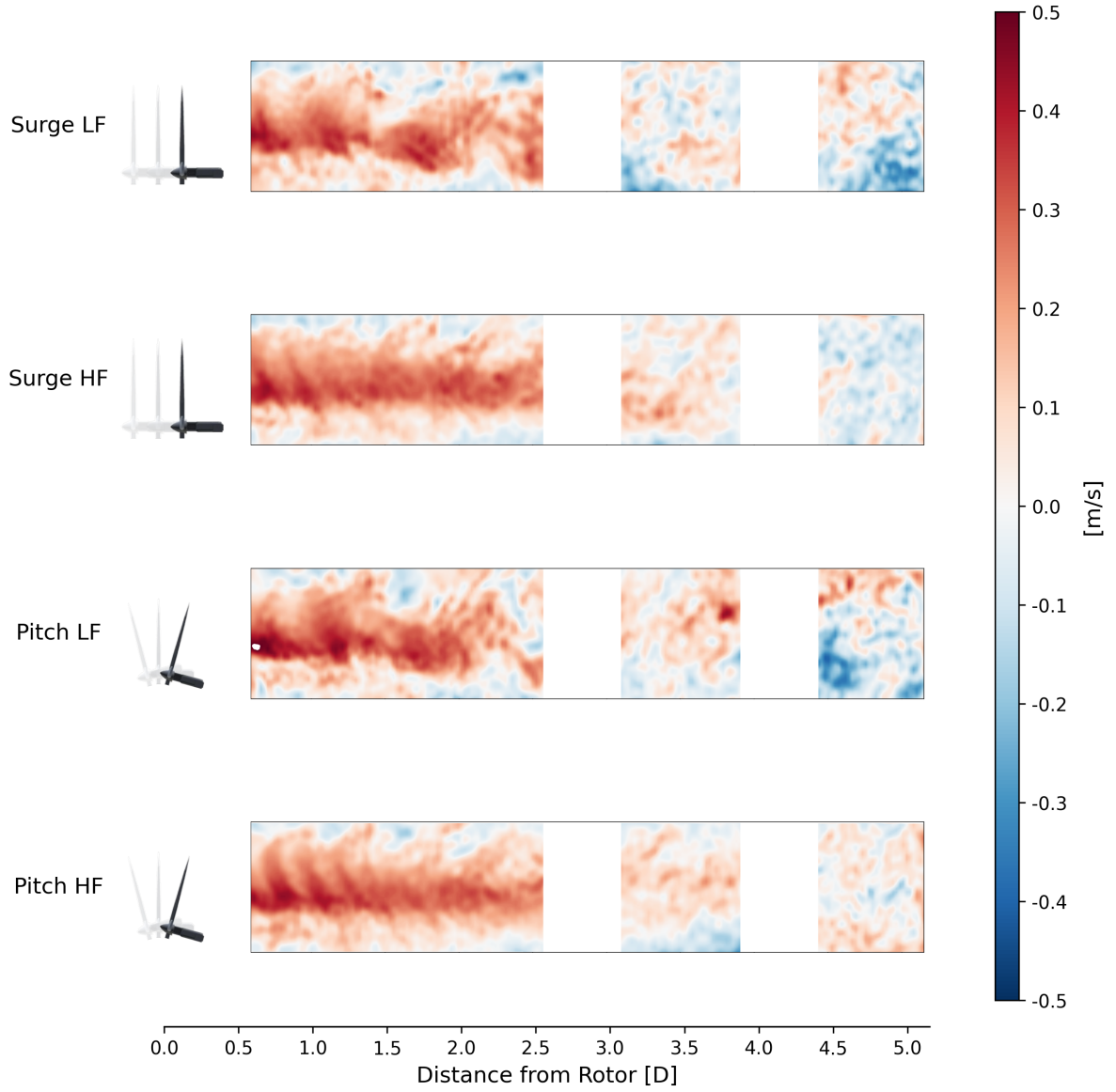

Figure D.14: Phase-locked average spanwise velocity component normalized by freestream velocity $\langle \bar{v} \rangle / U_\infty$ for static and motion cases at Position 4.

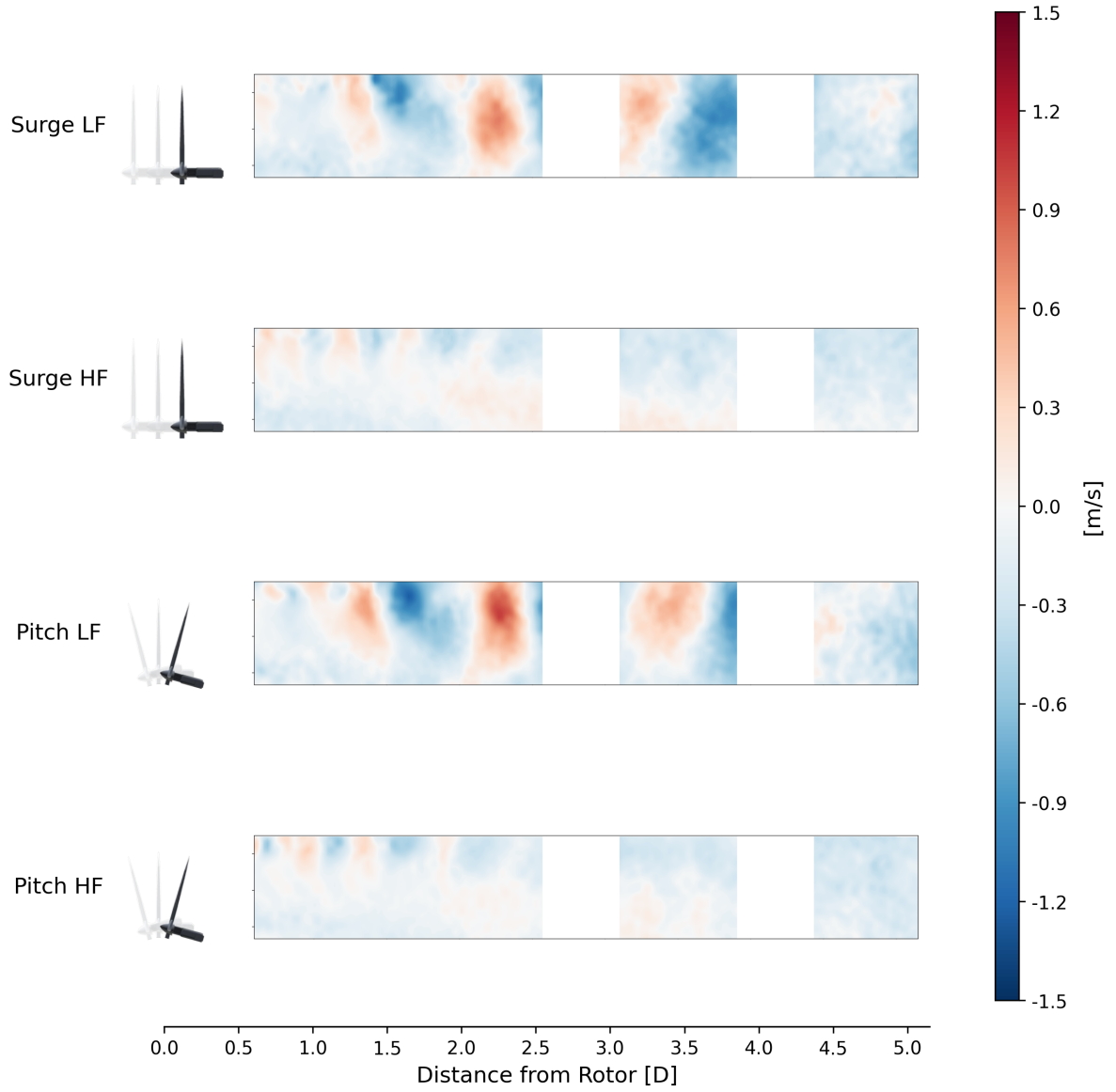

Figure D.15: Phase-locked average vertical velocity component normalized by freestream velocity $\langle \bar{w} \rangle / U_\infty$ for static and motion cases at Position 4.

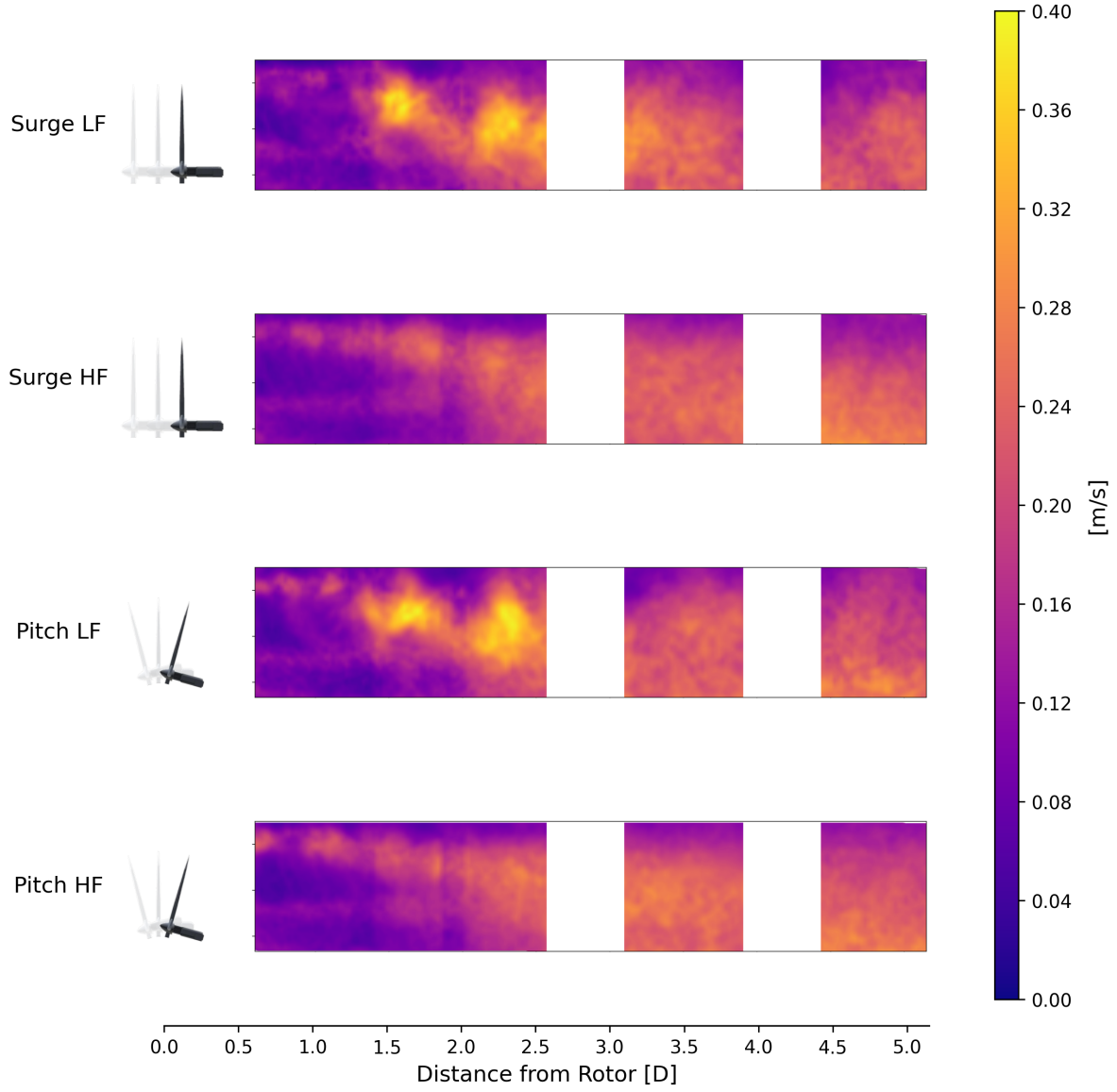

Figure D.16: Phase-locked average turbulence intensity TI for static and motion cases at Position 4.